

**DOCTORAL THESIS**

# Fast Assessment of Oil Shale Quality by Spectral Methods

Iram Tufail

TALLINN UNIVERSITY OF TECHNOLOGY  
DOCTORAL THESIS  
50/2022

# **Fast Assessment of Oil Shale Quality by Spectral Methods**

IRAM TUFAL



TALLINN UNIVERSITY OF TECHNOLOGY

School of Science

Department of Cybernetics: Division of Physics

The experimental part was done at the Plasma Physics laboratory of the University of Tartu

This dissertation was accepted for the defence of the degree 03/06/2022

**Supervisor:** Professor Jaan Kalda  
Department of Cybernetics  
School of Science  
Tallinn University of Technology  
Tallinn, Estonia

**Co-supervisor:** Associated Professor Emeritus Matti Laan  
Institute of Physics  
Faculty of Science and Technology  
University of Tartu  
Tartu, Estonia

**Opponents:** Juraj Jašík, PhD  
Department of Chemistry of Ions in Gaseous Phase  
J. Heyrovský Institute of Physical Chemistry  
Czech Academy of Science  
Czech Republic

Indrek Aarna, PhD  
Head of Development Department  
Viru Keemia Grupp  
Estonia

**Defence of the thesis:** 07/09/2022, Tallinn

**Declaration:**

Hereby I declare that this doctoral thesis, my original investigation and achievement, submitted for the doctoral degree at Tallinn University of Technology has not been submitted for doctoral or equivalent academic degree.

Iram Tufail

-----  
signature



European Union  
European Regional  
Development Fund



Investing  
in your future

Copyright: Iram Tufail, 2022

ISSN 2585-6898 (publication)

ISBN 978-9949-83-887-5 (publication)

ISSN 2585-6901 (PDF)

ISBN 978-9949-83-888-2 (PDF)

Printed by Koopia Niini & Rauam

TALLINNA TEHNIKAÜLIKOOL  
DOKTORITÖÖ  
50/2022

# **Põlevkivi kvaliteedi kiirmääramine spektraalsetel meetoditel**

IRAM TUFAIL





# Contents

List of Publications .....	7
Author's Contribution to the Publications .....	8
Abbreviations .....	9
Introduction .....	10
1 Oil shale: properties and applications.....	13
1.1 General Properties.....	13
1.2 Estonian Oil Shale Properties.....	14
1.3 Oil Shale Mining .....	17
1.4 Areas of Applications .....	18
1.5 Industrial Assessment of Oil Shale Quality .....	22
1.6 Environmental Aspects .....	23
1.7 Requirement for Characterization of oil shale.....	24
2 Spectral Methods and Data Processing .....	26
2.1 Laser-Induced Breakdown Spectroscopy (LIBS) .....	26
2.1.1 LIBS Phase .....	26
2.1.2 LIBS Technique .....	28
2.1.3 Quantitative Analysis by LIBS.....	31
2.1.4 Data Processing Algorithms .....	34
2.1.5 Application of LIBS in the Analysis of Different Raw Ores .....	35
2.2 Diffuse Reflectance Spectroscopy (DRS).....	38
2.2.1 DRS Principle .....	38
2.2.2 DRS Technique .....	39
2.2.3 Applications of Diffuse Reflectance NIR Spectroscopy in the analysis of different raw materials .....	42
3 Experimental Methods.....	44
3.1 Samples.....	44
3.1.1 Powder Samples .....	44
3.1.2 Crushed Specimens .....	45
3.1.3 Variation of moisture content .....	47
3.2 LIBS device .....	48
3.3 DRS device .....	49
3.4 Recording procedures and preprocessing of spectra .....	49
4 Results and Discussion .....	51
4.1 LIBS results.....	51
4.1.1 Fluctuations .....	52
4.1.2 Crushed oil-shale samples with low moisture content.....	55
4.1.3 Crushed oil-shale samples with different moisture contents.....	60
4.1.4 Application of multivariate regression model for data processing.....	62
4.2 DRS Results .....	66
4.3 Conclusions .....	67
References .....	71
Acknowledgements.....	82
Abstract.....	83
Lühikokkuvõte.....	85

Appendix 1 .....	87
Appendix 2 .....	99
Appendix 3 .....	119
Curriculum Vitae .....	130
Elulookirjeldus.....	131

## List of Publications

The list of publications, on the basis of which the thesis has been prepared:

- P I. Aints, M., Paris, P., Laan, M., Piip, K., Riisalu, H., & **Tufail, I.** (2018). Determination of heating value of Estonian oil shale by laser-induced breakdown spectroscopy. *Journal of Spectroscopy*, 2018.
- P II. Aints, M., Paris, P., **Tufail, I.**, Jogi, I., Aosaar, H., Riisalu, H., & Laan, M. (2018). Determination of the calorific value and moisture content of crushed oil shale by LIBS. *Oil Shale*, 35(4), 339-355.
- P III. **Tufail, I.**, Paris, P., Jõgi, I., Aints, M., Siiman, A., Riisalu, H., & Laan, M. (2020). Application of diffuse reflectance spectroscopy for quick laboratory assessment of Estonian oil shale quality. *Proceedings of the Estonian Academy of Sciences*, 69(2).

The copies of the publications P I–P III are included in Appendices.

## **Author's Contribution to the Publications**

The Contribution by the author to the publications was as follows:

- P I. The author participated in data processing, discussion of the results, and making the figures.
- P II. The author carried out the experiments, participated in data processing and in the discussion of the results, and making the figures.
- P III. Iram Tufail was the responsible author, she carried out experiments, participated in the data processing, interpretation of results and writing the paper.

## Abbreviations

CCUS	CO <sub>2</sub> capture, utilization and storage
CCD	Charge coupled device
CFB	Circulating fluidized bed
DRS	Diffusive reflectance spectroscopy
FTIR	Fourier transform infrared
LIBS	Laser-induced breakdown spectroscopy
NIR	Near infrared
PCA	Principal component analysis
PF	Pulverized firing
PGNAA	Prompt gamma neutron activation analysis
PKK	Estonian oil shale competence centre
PLSR	Partial least square regression
RSD	Relative standard deviation
SDEP	Standard deviation error of prediction
SNR	Signal-to-noise ratio
TGA	Thermo-gravimetric analysis
UV	Ultraviolet
XRF	X-ray fluorescence
ZPD	Zero path difference

## Introduction

Oil shale is among the most important strategic raw materials of Estonia [1] and during last 100 years a huge experience in oil shale mining, production of oil and electricity is obtained. The know-how in oil shale industry is based on studies of numerous Estonian researchers. Thanks to a strong domestic energy industry, even in 2017 Estonia has been the European Union's most energy-independent country [2]. However, oil shale industry has a large ecological footprint and big investments have been made to reduce the environment pollution. As an example of these efforts, during the last 30 years the CO<sub>2</sub> emission has been diminished by a factor of two.

EU regulations foresee the replacement of fossil energy sources by renewable ones. This placed oil shale based electricity generation under serious pressure as the market price of carbon dioxide emissions was tripled [2]. The growth of prices for CO<sub>2</sub> emission seems to fasten as the European Commission has proposed to diminish greenhouse gas emissions by 2030 at least by 55% from the level of 1990, so that Europe would become carbon neutral by 2050 [3].

These circumstances led to fast changes in the energy field, during the year of 2020, the Estonian electricity production from oil shale diminished by ca 43 % [4] This fall was partly compensated by renewable sources of energy but the total energy balance was still negative.

The role of wind mills and solar panels as electricity generators is gradually increasing, and it is likely that in a near future, these sources will be able to cover the Estonian need for electric energy during the periods of favourable weather conditions. However, daily and seasonal fluctuations of the energy production is a serious drawback of the green sources of energy. While short-time fluctuations can be compensated by pumped-storage hydroelectricity [5], in future, hydrogen technology can be predicted to become the leading option for storing renewable energy [6]. It should be emphasized that all these green energy developments will be requiring long-term research, engineering efforts, and big investments.

The fall of the production of green energy at the beginning of 2021 caused a big increase of the electricity price; to compensate this decrease of green energy production, oil shale power plants were switched on and they worked at their full output power.

The nowadays situation and the prediction of developments in production of electric energy is summarized by the president of the Estonian Academy of Science as follows [7].

*The society has to be provided with a large amount of stable electric energy. Our present way of electricity production by fossil fuels should be kept alive till new sources are able to replace the existing ones. It is not related only to habit, cheapness, comfort and even to social policy, but first of all, it is the topic of the energy security.*

In the frames of RITA program, the possibilities for continuation with oil shale in a smart, clean and socially responsible manner were studied [8]. The study examines options to continue with the existing production units in the oil shale industry implementing CO<sub>2</sub> capture, utilization and storage (CCUS) technologies. It was pointed that CO<sub>2</sub> capture is an environmental technology that does not improve the quality of the final product and, as with other environmental technologies, leads to additional costs. It was found that applying the most suitable CO<sub>2</sub> capture technologies, the CO<sub>2</sub> footprint of electricity production would fall by an order of magnitude, using the existing Auvere plant as the reference. However, CO<sub>2</sub> capture would not be financially feasible under the current market conditions. Citing Ref. [8]: "Additionally, it would be possible to reduce

the CO<sub>2</sub> footprint of electricity production by reusing the ash produced during combustion. Using co-combustion of wood chips and oil shale it is also possible to achieve a negative CO<sub>2</sub> emission, assuming that the CO<sub>2</sub> produced from burning wood chips is not counted as CO<sub>2</sub> emissions”.

The questionable feasibility of CO<sub>2</sub> capture is based on the present know-how, but the intensive study of more efficient methods of the implementation of economically viable and promising CCUS technologies takes place [9].

Using of oil shale as a solid fuel is on a crossroads and its future depends on investments. Differently from this situation, the shale oil as a liquid fuel is competitive in the world market even in the case of the most conservative scenarios and a new factory will be built [10]. A novel technology implemented in this factory will reduce the CO<sub>2</sub> emission by 3.3 times.

The fine chemicals obtained from oil shale are used in different fields of industry and the export of phenol products (including fine chemicals) increases quickly [2]. Researches have been developed new efficient methods like wet air oxidation [11], which application in industry will broaden the list of oil shale based chemicals. Above all, the future of Estonian oil is in the field of oil production and chemistry.

Oil and electricity production produces huge amount of gaseous, liquid and solid by-products. These are not worthless waste but rather potential inputs for production for a second go-round [2]. There are many ideas related to re-use of these materials but up to now only a limited number of them is realized.

Environmental impact, yield of chemical products, lifetime of boilers/retorts and a number of other factors depend on the properties of the raw material. Achieving a minimum level of the surrounding pollution and a high efficiency of an industrial process requires the knowledge of quantitative characteristics of the raw material. Because the properties in the flow of the mined oil shale vary remarkably, a fast real-time testing method is needed. Most of the existing control devices are single-purpose; as an example, the moisture content is measured by the absorption of the microwave radiation and this method cannot be used for the measurements of the gravel stiffness. In this thesis we chose the laser induced breakdown spectroscopy (LIBS) as the main technique for testing the oil shale properties. LIBS is a fast, non-invasive and safe method which is applied for control of numerous industrial processes [12]. Information obtained from LIBS spectra is multipurpose as using corresponding calibration curves it is possible to find different characteristics of the raw material.

The study achieves its goal when the measurements are carried out in conditions which are close to those on the running conveyer belt. In our experiments crushed oil shale lumps have been used as samples; their moisture content was changed artificially to mimic varying mining conditions.

Main LIBS experiments were made with oil shale lumps which had random orientation and size. Besides, the LIBS spectrum was collected from a very small solid angle. To clarify the effect of these factors limiting the accuracy of recording of LIBS spectra, two extra studies were made. First, LIBS measurements were made with air-dry powder pellets. Second, using the method of diffusive reflection spectroscopy (DRS), spectra were recorded in the near infrared region (NIR). In case of DRS, the light was collected from a solid angle of  $2\pi$  sr.

The main aim of the thesis is the LIBS testing of Estonian oil shale samples for the assessment of the values of calorificity, moisture content and concentrations of chemical species. The LIBS results were calibrated using data obtained by other methods.

While this thesis is based on the papers [PI–PIII], not all the content of these papers is reproduced: the main text of the thesis reproduces the most important parts of the papers while adding insight to the physical background of the studied phenomena; the appendixes with the full texts of the papers are assumed to be an integral part of the thesis. It must be emphasized that there are minor differences in the terminology and abbreviations used in main text of the thesis, as compared to the ones used in the papers.

The thesis is divided into four chapters. Each chapter is divided into sections and subsections.

Numbering of references and figures are grouped according to the chapters.

Chapter 1 starts with an overview of general oil shale properties, geology of Estonian oil shale (kukersite) beds, and the composition of different layers are described in more detail. Next few sections are devoted to the oil shale mining and applications, together with the related problems. In the final section, a detailed plan of the study is laid out.

Chapter 2 is dedicated to the optical methods used in the study. First, based on a literature review, the physical background of the methods, and the procedures of obtaining quantitative results are described. Besides, main results of different papers, related to the study of raw materials by LIBS and DRS, are presented.

Chapter 3 starts with the description of samples, including a detailed explanation of the method of variation of the moisture content. Further, the description of the used optical devices is presented. Additionally, the methods of recording and preprocessing the spectra, aimed to reduce the effect of fluctuations, are described.

Chapter 4 is devoted to the presentation and discussion of the results obtained by using LIBS. It starts with the analysis of the background of fluctuations in spectra. As the moisture can cause big changes in spectra, spectra of the samples with a low moisture content were analyzed separately. Subsection 4.1.3 describes the multivariate regression model, which allows better predictability of calorificity and moisture content values. DRS results in 4.2 allows to clarify problems related to LIBS technique. Final section 4.3 collects the main conclusions of the study and proposes further developments of the LIBS technique.

# 1 Oil shale: properties and applications

## 1.1 General Properties

“Oil shale is fine-grained sedimentary rock containing solid organic matter (kerogen). Content of mineral as well as organic parts could be different”.

Kerogen is formed from organic material that can have many different origins. It is often classified according to the origin of the organic material into three main categories: terrestrial, lacustrine and marine.

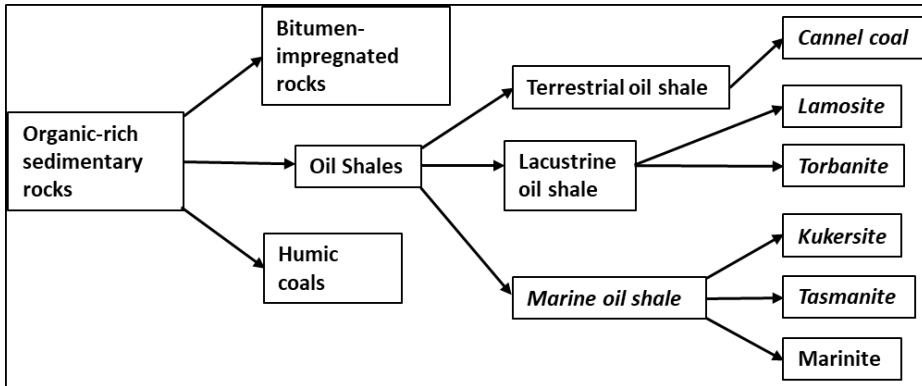


Figure 1.1. Classification of oil shale. Adopted from [13].

The oil shale from different deposits varies, depending on their geological deposition period, the contents and types of minerals and chemical composition of the organic matter [14].

The terminology of oil shale and shale oil contains many contradictions. Scientists and experts around the world have long debated the use of appropriate terms, but have not yet been able to define harmonized terminology. Under new terms to replace the currently “shale oil”, “shale” and “shale gases” will be suggested.

The name of the material reflects the main field of application: In German, Estonian and Russian names (in Estonian *põlevkivi*, in German *Brennschiefer* and in Russian *gorjuchii slanets*) are stressed its combustibility, but the name “oil shale” points a possibility to produce oil by an industrial chemical treatment. In this case the oil is obtained by heat treatment in the absence of oxygen (sometimes called retorting).

The name “oil shale” should not be confused with the “tight oil” which exists in porosity structure of a number of sediments and rocks. Tight oil in these sediments and rocks is natural raw oil. Even if the tight oil is achieved from sediments with heat or thermal treatment (e.g. direct steam heating in the case of oil sand), it is not shale oil [15].

The majority of oil shale contain organic matter derived from a variety of marine and lacustrine algae species, with some debris from land facilities, depending on the deposition environment and sediment sources. Organic matter in oil shale is a complex blend and comes from carbonaceous residues of algae, Plant cuticle, stones, cork fragments of herbaceous and woody plants, pollen, plant resins and plant marine waxes and other cellular residual cell waste [16, 17]. The basic mineral matter of oil shale could be of two types. The first type is carbonate, which contains a high proportion of carbon

deposits (for example calcite and dolomite). The second type is siliceous, which contain a high proportion of silicate deposits (for example clay, quartz, opal and feldspar) and it usually gives a black or dark brown color to the oil shale [18].

Oil shale is mostly spread throughout the world. Oil shale deposits can be found on all continents in over 600 deposits; the reserves are distributed more evenly compared to fuel and for many countries, oil shale represents almost the only type of fossil fuel. Oil shale kerogen is the fossil fuel like natural gas, coal and traditional petroleum [19].

The oil shale quality is evaluated by two main characteristics; oil shale calorific value and oil yield of oil shale.

Oil shale as source of oil is characterized by quantities of oil or combustible gas that would be yielded by retorting process. The oil yield is defined as the amount of oil obtained from a mass unit during the process of low-temperature carbonization of oil shale [20]. Oil shale differs from other humus fuels by its high ratio of hydrogen and oxygen content in organic matter. The atomic ratio of hydrogen to carbon (H/C) is about 1.2–1.7, which is nearby of crude oil: 1.8–2.0. This resemblance is the main reason why oil shale is measured an alternative source for liquid fuel production. Comparing oil shale with primary solid fuels, it looks more like brown coal, which has an H/C ratio of 0.8. For comparison, the anthracite coal ratio is about 0.3 to 0.4 [21].

Oil shale as a source of solid fuel is characterized by calorific value and mineral content. The calorific value  $Q$ ,  $\text{MJkg}^{-1}$ , shows the thermal energy achieved by burning a mass unit. The calorific value can be in the range of 5 to 20  $\text{MJkg}^{-1}$ , and mineral content can be in the range of 30–70%. Due to the relatively high mineral content of oil shale, the ash content can be up to 85%. The sulfur content of oil shale can be up to 12% and moisture content range from 4–45% [22].

## 1.2 Estonian Oil Shale Properties

The main type of the Estonian oil shale is known as Kukersite, which is a type of kerogen [23]. This organic matter is deposited in marine limestones and it is formed during the Middle Ordovician to Early Late Ordovician time span [1].

Estonia oil shale resources are estimated 5.94 billion tons [24], which are the ninth largest in the world [25]. The sites of Estonia's oil shale resources covers 5000  $\text{km}^2$  and are located in northern Estonia and extend east of Russia to St. Petersburg, In Estonia, a somewhat younger deposit, the Tapa deposit, overlies the Estonia Kukersite deposit, Figure 1.2 [24]. Oil shale is currently mined in three open pits (Narva, Põhja-Kiviõli, Ubjä) and two underground mines (Estonia, Ojamaa).

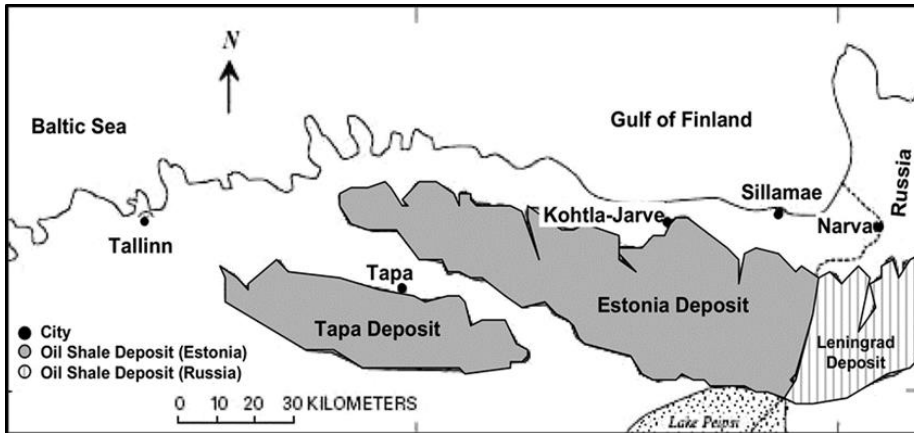


Figure 1.2. Map of Estonian oil shale resources, [25].

Bed index	Caloricity, MJkg <sup>-1</sup>	Oil yield, %
H	8.2	14.6
G/H		
G	15.8	28.1
F <sub>2</sub> /G		
F <sub>2</sub>	5.1	9.1
F <sub>1</sub>	9.4	14.6
E/F <sub>1</sub>		
E	12.1	21.5
D/E	3.1	
D	10.6	18.9
C/D		
C	10.9	19.4
B/C	3.4	
B	18.5	32.9
A'/B	2.4	
A'	5.7	10.1
A	15.0	26.7

Figure 1.3. Main characteristics of kukersite oil shale beds in the Põhja-Kiviõli open-pit mine. The origin of the scale is at the bottom of the deposit. Adopted from [1].

The kukersite oil shale beds vary depending on the deposit location and form up to 20–30 m thick succession. However, individual kukersite beds of chocolate-brownish colour are commonly 10–40 cm thick and may reach as much as 2.4 m. The kukersite oil shale has as many as 50 beds. The oil shale bed has a complex heterogeneous structure and

consists of oil shale's layers of different quality that alternate with limestone layers [1, 26]. Beds currently mined are designated by capital letters A–H, Figure 1.3. Only layers A, D and H contain pure kukersite. Other layers contain, on a larger or smaller scale, limestone compositions with an average kukersite content of 8%. The energy content of different layers depends on the plenty of the mineral part, its higher amount leads to a lower energy content.

Limestone layers D/E, E/F<sub>1</sub> and B/C are organic limestone, while A, A' and A'/B is clay-like limestone. The mineral (as well as chemical) composition of all the ingredients alone is relatively stable, regardless of the location and the deposition layer.

Table 1.1 shows the characteristics of the different oil shale layers. As layers G and H are separated from lower ones by a meter-thick limestone layer they are not used for production, mainly for economic reasons. The thin layers deeper than layer A also are not used. In the case of underground mining layer F forms the mine ceiling, but in the case of open pits, it is used.

*Table 1.1. Characteristics of oil shale layers [26].*

<b>Layer</b>	<b>Character of layer</b>
H	Not used for production
G/H	Tight limestone
G	Not used for production
F <sub>2</sub> /G	A clay-rich limestone with clayey oil shale interlayers
F <sub>2</sub>	Contains plenty of intermediate oil shale interlayers of variable thickness. In the oil shale base layer there are two or three layers of different calorific value
E/F <sub>1</sub>	A thin organic rich interlayer without fixed borders
E	The most important payable layer besides layer B. Limestone content is lower than in other layers
D/E	A thin organic rich limestone layer
D	Contains plenty of thin limestone layers, only with difficulty separable from upper and lower limestone interlayers
C/D	Mostly pure limestone
C	Limestone-rich layer
B/C	Layer of variable thickness containing organic matter in substantial amount
B	The most important payable layer containing small layers of crystal limestone
A/B	Interlayer A/B—the clayey limestone
A	The layer A, distributed into upper and lower zones. The upper one is a limestone-rich oil shale layer
A'/A	A clayey organic-rich limestone layer
A'	A clayey oil shale layer without limestone inclusions

In addition to organic matter, Estonian oil shale is mainly composed of limestone and clay, as shown in Table 1.1. Clay does not exist in the oil shale bed as a separate layer but is distributed into oil shale and limestone layers as the addition of fine-grained, consisting of sand and clay.

Estonian oil shale (as a dry matter) can be classified into three categories: sandy clay, organic material and carbonates. The chemical composition of three main parts of oil shale is presented in the Table 1.2, [26]. Organic part of Estonian kukersite is described by an empirical formula  $C_{421}H_{638}O_{44}S_4NCl$  [23].

Table 1.2. Chemical Composition of the Estonian oil shale.

Sandy clay part		Organic part		Carbonate part	
Compound	Average Content %	Compound	Average Content %	Compound	Average Content %
Al <sub>2</sub> O <sub>3</sub>	16.1	H	9.70	CO <sub>2</sub>	45.1
H <sub>2</sub> O	2.6	C	77.45	FeO	0.2
SiO <sub>2</sub>	59	N	0.33	MgO	6.6
FeS <sub>2</sub>	9.3	O	10.01	CaO	48.1
CaO	0.7	Cl	0.75		
MgO	0.4	S	1.76		
Fe <sub>2</sub> O <sub>3</sub>	2.8				
Na <sub>2</sub> O	0.8				
K <sub>2</sub> O	6.3				
TiO <sub>2</sub>	0.7				
SO <sub>3</sub>	0.5				
Total	100	Total	100	Total	100

The total content of these compounds of oil shale is 100%, which means that there are no other organic compounds or significant minerals.

The layer B has the highest calorific value 18.5 MJkg<sup>-1</sup> and layer A'/B has lower calorific value 2.4 MJkg<sup>-1</sup>. At the same time, calorific value of standard grades of coal changes from 33.412 MJkg<sup>-1</sup> to 16.077 MJkg<sup>-1</sup> [27].

The layer B has the highest oil yield 32% and the layer F<sub>2</sub> has the lowest oil yield 9.2%.

Above-presented numerical values describe dry oil shale, but the moisture content of commercial oil shale can range from 8 to 14% [20].

### 1.3 Oil Shale Mining

At present in Estonia oil shale is extracted by opencast mining and underground mining.

In both cases, oil shale is excavated and transported to a treatment plant where it is crushed, sometimes upgraded and then heated to produce shale oil or placed in ovens to generate heat or electricity. Different types of mining technology are used in the deposit.

- *Opencast Mining*

The open pit mines "Aidu" and "Narva" use stripping with dragline, bucket 10–15 m<sup>3</sup>. Overburden and the bed both are separated by blasting and then stripping is done with smaller excavators on surface with a thin overburden using front loaders and hydraulic excavators. Overburden carried out by loaders and trucks. The overburden thickness limit is evaluated for 27 to 30 meters [28].

Mass extraction of all beds (F-A layers) takes place in the open cast mining in Aidu where a separation unit operates. The open cast mines in Aidu and Narva use selective extraction in three layers of seams. The upper (F/E) and the lower (B/C) layers are extracted as run of mine, the middle seam (interlayers D/C and F/E) is pushed or dehydrated in the extraction area. If the bed breaks mechanically, with washers, the oil shale extracted completely and selectively. Layers A and D are taken in run of mine, which were lost in a partial selective extraction [29]. The D/C layer is extracted with a hydraulic hammer and pieces of limestone are loaded and transported to the screening and crushing plant where the aggregate is produced by successively placed impact crushers and is sifted into required fractions. The method for producing aggregates is to use the Wirtgen 2500 SM surface coal miner [30]. The crushed limestone must have a cubic particle shape. The problem is that the aggregate produced by the surface miner is characterized by many fine and thin particles and therefore the instability index of the aggregate is high [31]. The aggregates produced are washed to minimize the fine content.

One way to get limestone concretions from oil shale layers in uncrushed form without separation and to adjust the cutting thickness of surface miner in correspondence to thickness of concretions [32].

Eesti Põlevkivi's Narva mine also began with selective export [29]. The miner can cut limestone and oil seams separately and more precisely from the ramps (2...7 cm) with deviations of about 1 cm [33].

- *Underground Mining*

Underground mining technology uses blocks of room, formed up to 10 meters long work surface [34]. The roof of the room supported with pillars that are not extracted oil shale (25% averaging of reserves) and fastened to the upper rock layers.

Longwall mining has also been used, where the bed was mined with a carbon cutter shearer loader. During the mining performance with the shearer, the A–C layers were extracted, so it was actually selective extraction. This method of extraction was more productive, but much more capital intensive [20].

In enrichment plant a rough separation of organic and mineral lumps of oil shale is carried out in sink/float tanks. The tank is filled with water and, depending on the materials to be separated, additives to alter the fluid's density are added. The mixed stream of oil shale and limestone is directed into the tank where high-density limestone will sink, but low-density kerogen will float. The separated lumps will be conveyed for further processing [35].

## **1.4 Areas of Applications**

Comparing with the other countries, the use of oil shale in Estonian economy is high. Oil shale has no export potential as an energetic mineral due to its low calorific value and high mineral contents, and oil shale is only cost-effective when used as a raw material for industries located close to shale mines. Oil shale is mainly used for fuel production and electricity generation, while the production of oil is gradually increased and the role of oil shale in electricity is diminishing [2]. Products achieved from the processing of oil shale (shale oil, electricity, building material and chemicals) have good export potential. Depending of area of use specific technology with corresponding equipment have been developed. Figure 1.4 presents the different fields of oil shale applications [2].

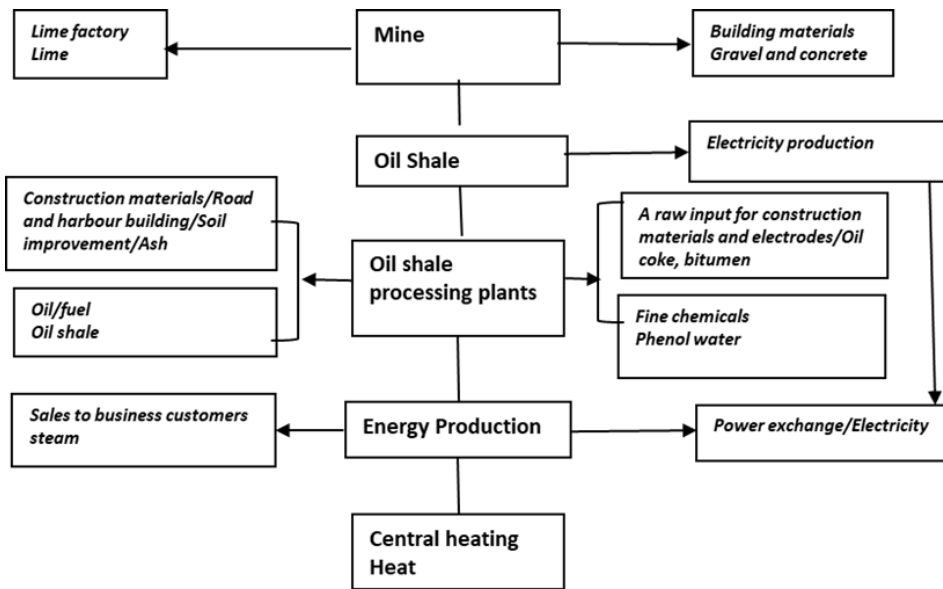


Figure 1.4. Oil shale value chain. Adopted from [2].

### • Lime and Gravel

Limestone extracted from oil shale in the mines, is used for production of high-quality gravel [36]. Gravels constitute the majority of coarse aggregate used in concrete with crushed stone making up most of the remainder. It is also used in road construction [37]. Some lime is sent to the lime factory for further process (Lime Kiln, Crushing, screening, grinding and hydration) under specific parameters (pressure, moisture content and temperature) [38, 39].

### • Shale Oil Production

Compared with coal, the oil shale kerogen contains more hydrogen and can therefore be subjected to thermal conversion into oil and gas [40]. At the moment the production of oil is the most important outcome in the oil shale industry.

Shale oil is produced by pyrolysis process. Pyrolysis is the thermal decomposition of materials at elevated temperatures in an oxygen-free atmosphere. The oil shale is heated at high temperatures until kerogen decomposes into vapors of petroleum-like condensable shale oil, a non-condensable combustible oil shale gas, solid residues (semi-coke, ash, pitch residues) and phenolic water [41]. The yield of oil shale and exact composition not only depend on the composition but also on the type of reactor where the oil was produced, as well as on process parameters such as pyrolysis time, heating rate and pyrolysis temperature in the reactor.

In Estonia, the next types of retorting technology are used:

- *Gas heat carrier (vertical retort) technology*, it is an internal combustion technology in which the gas is used for heat transfer. This technology uses grains of 25–125 mm size and the temperature of the pyrolysis 900 °C (Kiviter technology, used in the Viru Oil plant and Kiviõli oil plant), the process results in oil steam and gas [42].
- *Solid heat carrier (horizontal rotating cylindrical retort) technology*, in which circulating solids are used as a heat carrier. This technology uses grains up to 25 mm size and

the temperature of pyrolysis is kept at 520 °C. (Galoter technology, operating in the Narva oil plant) [43]. Currently there are different modifications of Galoter technology in use, the latest is realized in the plant Enefit-280 [44]. This process results in oil steam and gas, which calorific value is higher than that of gas heat carrier technology [45].

- *The parallel use of these two technologies*, allows a greater flexibility in the use of raw material, the oil shale fraction sized 0–125 mm is used, simultaneously, the finer fraction of raw material shifted from the Kiviter process can be used in the solid heat carrier process [46].

The overall efficiency of the use of oil shale is 43% and 52% for Kiviter and Galoter technologies, respectively [47]. Using the oil in cogeneration plants, the efficiency of production of heat and electricity could reach 79%.

The advantage of the oil resulting from the Estonian oil shale pyrolysis is that it is lower in sulfur content than petroleum based oil and has a low viscosity for its density [2]. The sulfur content of the shale oil from the Estonian producers is on average 0.8%, which meets the criteria for low sulfur fuels. In the future it is also planned to reduce sulfur in all oils to 0.5% by volume and in the distant future to less than 0.1% [2].

In addition to electricity, heat and fuel, there are also various chemicals produced from shale oil. Some of the chemicals, for example phenols are important in industry as a raw materials and additives [48, 49]. The overview of current research trends in the production and separation of phenolic rich bio-oils, as well as their applications are in [50]. The results of the full chemical analysis of Estonian oil shale – characteristics of shale oil, analysis and distribution of sulfur, pyrolysis mass balance analysis are presented in [51]. In VKG (Viru Keemia Grupp) valuable chemicals extracted from the phenol water, which is the by-product of oil production. Fine chemicals have high purification level, i.e. over 99% [2]. Oil shale chemicals are widely used in the manufacture of moulds and as epoxy adhesives in rubber, plywood and the petroleum industry. Phenols generated are used in Lexus and Toyota car companies to make high-strength tires. The fine chemicals derived from shale oil are used in the perfumery, cosmetics and electronics industries. Products with a high purity can be found in medicines and hair dyes. LCD monitors liquid are also made from them. More information about the fine chemicals are in [2, 52].

The combined use of oil shale and shredded tyres in a pyrolysis process works when shredded tyres make up up to 10% of the fuel mixture. The quality of the oil produced from a combination of shredded tyres and oil shale remains the same and the environmental impact does not increase. Eesti Energia plans to start making oil from tyres at the end of their life cycle in the coming years [2].

### • Electricity Production

Due to development of green energy and European environmental regulations, the importance of oil shale based power plants is diminishing drastically. Nevertheless, these power plants maintain their role as a stabilizing factors in electricity production.

In Estonia two different combustion technologies of oil shale for power generation are implemented: *pulverized firing (PF)* and *circulating fluidized bed (CFB)* technologies. Latest studies related to PF and CFB technologies are presented in [53, 54]. Some of the test results in CFB technology and the reliability of the boiler are presented in [55–60].

#### –*Pulverized Firing (PF)*

Currently, PF is the most common high temperature combustion technology for solid fuels. The main issues considered in design of oil shale firing boilers are presented in [61].

In case of PF technology the combustion area increases greatly, thus increasing the thermal efficiency, it results in a faster combustion rate.

During the burning pulverized oil shale, the maximum flame temperature in the furnace chamber reaches 1400–1500 °C.

Besides, if the lower grade oil shale is pulverized then it can also be used as an efficient fuel.

Compared with solid fuel firing PF technology have the next advantages [62]:

- The start of the PF technology is faster than that of the solid firing system. Even from a cold state its operation starts very quickly and efficiently. This feature of the boiler system is essential for ensuring the stability of the electrical network.
- Another key feature of PF technology is that it has no moving parts inside the combustion chamber which gives it a long trouble-free life.
- Ash handling is simpler in this system, as there is no solid ash.

#### –*Circulating Fluidized Bed (CFB)*

In case of CFB the gas and solids mix turbulently and compared with PF a better heat transfer is achieved. Up to 95% of pollutants can be absorbed before they are released into the atmosphere. As the fuel burns at temperature interval 760 °C – 927 °C, the formation of nitrogen oxide is negligible [63]. In CFB conditions sulfur dioxide emission is significantly reduced due to mixing the fuel particles with limestone or dolomite. As a result, 95% of sulfur pollutants are absorbed.

Alternatively, the sulfur-absorbing chemical and fuel will be recycled for increasing the efficiency production of high quality steam as well as for the lowering the emission of pollutants. Therefore, it will be possible to use circulating fluidized bed technology for fuel combustion in much more environmentally friendly method as compared to other conventional processes [63].

Due to design of CFB boiler no significant polluting or corrosion of heat exchangers have happened in CFB boilers at Narva power plants [57].

Using combined combustion of oil shale and biomass in the CFB helps to replace the use of fossil fuel by renewable one. Modern Auvere Power Plant can operate with 50% on biomass, up to 100% on oil shale, 10% on shale gas and 20% on peat. The effect of biomass and oil shale co combustion on emission, CFB boiler thermal efficiency, distribution of particle matter, CO<sub>2</sub> reduction and ash chemical composition was investigated in [64–70].

If biomass fuel compared with fossil fuels then the most important differences are variability of fuel characteristics, low energy density, higher moisture contents and low nitrogen and Sulfur contents of biomass fuels. The moisture content has a large influence on the combustion process and on the efficiency. In the future wide range of biomass fuel utilize in large-scale power generation [71].

#### • **Oil Shale Ash**

The inorganic part of Estonian kukersite oil shale consists of carbonates and terrigenous materials. Commercial oil shale contains 65 to 80% of mineral matter. Combustion of oil shale produces ash with diverse mineral composition [72]. The main ingredient, calcium carbonate makes up 57 to 75% of the total mineral matter content. Besides, the mineral part of the inorganic matter contains fine-grained quartz (SiO<sub>2</sub>) (8 to 16%), orthoclase ( $KAlSi_3O_8$ ) (4 to 8%), mica (silicate minerals) (6%), marcasite (FeS<sub>2</sub>) (4%), and hydromica [73].

Ash properties (chemical and others) depend on burning conditions (PF vs CFB) but also in separation point (bottom ash, fly ash) [74]. The problems relating to the chemical-mineralogical composition of oil shale ash and the conditions at hydro (wet), dry, or semidry ash removal are analyzed in [75].

Oil shale ash produced during oil and electricity production has a number of applications [72, 76]. The shale ash can be used to produce various cements as well as different construction materials such as blocks and various mixtures and for many other purposes [77]. Currently, the most effective way is to use oil shale ash as a raw material for cement production [78]. Portland cement raw material made from oil shale ash that came from fly ash, which collected from electrostatic exhaust gas cleaners at power plants. Applications of oil shale ash as cement in the building material industry are in [79–81].

Recently oil shale has become a beneficial debtor in road construction activity and restrictions on crushing, limestone mining and sorting. Crushing is the main method of benefit, which is the softest part of oil shale, i.e. organic material, and screening it out [20].

Oil shale ash helps to increase the harvest of the fields, as it has high calcium carbonate content, which helps the soil to enrich it with trace element and to neutralize pH levels faster which neutralize acidic soils and to improve crops and grassland soils [72]. Besides, the results of studies confirmed that the fertilizer produced from oil shale ash helped in absorbing nutrients to plants from soil, inhibited the growth of mosses and reduced plant diseases [82].

Recent research of Ragn-Sells Company shows that calcium carbonate, which is one of the main oil shale components could be used in a wide variety of products, such as adhesives, sealants, food and pharmaceuticals, paints, coatings, paper, cements and construction materials [83].

## 1.5 Industrial Assessment of Oil Shale Quality

Among the main parameters of the quality of oil shale are the calorific value and the moisture content. The quality of oil shale entering the plants is variable but from the viewpoint of the efficiency and lifetime of oil retorts and boilers a relatively constant quality of raw materials is required [84]. Furthermore, the emission of greenhouse gases as well as other harmful by-products of oil shale processing depend also on the choice of treatment of the raw material. In previous days the quality management of oil shale production was mostly a financial problem [85], but nowadays the problems related to the ecological footprint are at the foreground.

Calorific value shows how much energy in the form of heat the fuel can generate during combustion. Net calorific value differs from gross calorific value in that it does not include the condensation heat of water, as this is usually dissipated as unused steam:

$$\text{Net calorific value} = \text{gross calorific value} - \text{condensation heat}$$

Thus, the gross calorific value is always higher than the net calorific value.

The procedure of determination of calorific value of oil shale is fixed in Estonian national standard EVS-ISO 1928:2009 *Determination of gross calorific value by the bomb calorimetric method and calculation of net calorific value* [86]. According to this standard, the gross calorific value is found by combustion of a fixed amount of oil shale in the calorific bomb at atmospheric pressure and etalon temperature 25 °C. The calorific bomb

is calibrated by certified benzoic acid combustion. Using empirical relationships, the knowledge of the moisture content allows to calculate the net calorific value.

The moisture content of a sample is the loss in weight (%) after oven drying at a fixed temperature until constant weight is obtained. Procedures foreseen for finding of the moisture content are described in Estonian national standard EVS 668:2018 *Oil shale: Determination of moisture* [87].

## 1.6 Environmental Aspects

The production of oil shale has a potentially serious impact on the environment [88]. Oil shale industry has several environmental impacts such as land use and solid waste management, water and air pollution, which caused by the extraction and processing of oil shale [89].

- *Land contamination and solid waste arising*

The most striking impact of the oil shale industry is the disruption to land use and waste disposal [90]. The value of existing land use as an ecosystem should be assessed before the development of oil shale and the overall environmental impact assessment should also consider the loss of land use after restoration. Mining waste, petroleum (including semi-carbon) and combustion ash require additional land use, therefore should avoid high-density population areas [90].

The waste material can contain of several pollutants including heavy metal, sulfate and polycyclic aromatic hydrocarbons (PAHs), some of which are carcinogenic and toxic [91, 92].

Solid waste treatment is an important environmental issue related to energy production. A peculiarity of oil shale is the high content of minerals about 40–50% of the original mass remains after combustion. The ash formed at the Narva power plant in Estonia and at the Ahtme power plant is deposited in ash fields next to the power plants. Hydro-transport is used to transport large quantities of ash, i.e. the ash is pumped to the storage site mixed with water. The ash is transported in closed systems, where the transport water does not come into contact with the environment. Surplus water generated by the precipitate is neutralized and treated as required and then transported to the environment in accordance with the terms and conditions set out in the environmental permits [90].

Citing Ref. [93], “To keep the environment decent and save natural resources, the producing of waste must be avoided as much as possible and the existing waste must be collected and managed in an environmentally friendly way. Estonian goal in the area of waste is to recycle, as much as possible, the materials left over from consumption”. Further (ibid.), “Waste must be recycled and reused as new materials. The environmental risk coming from waste should also be decreased.”

- *Water Management*

The analysis of the water situation is complicated by the fact that the main oil shale area is located on mechanical power and the chemical industry in Estonia. Water represents the main pollutant carrier in the oil shale industry. An environmental issue is to prevent the leakage of harmful materials from consumed shale to the water supply [21]. The treatment of oil shale is accompanied by the formation of treatment of water and dirt water containing tar, phenols, and many other products, much distinguishable and toxic to the environment [94]. Phenolic compounds are present in water bodies due to the discharge of contaminated wastewater from industrial, agricultural and domestic

activities into water systems. These compounds are known to be toxic and cause both severe and long-term effects in both humans and animals [95]. It has been concluded in [96] that phenol causes many harmful effects on fish and concerns about public health. Industrial wastewater must be treated before entering the water resources.

- *Air Pollution*

The highest air pollution is caused by oil shale power plants, which provide atmospheric emissions of gaseous products such as sulfur dioxide, nitrogen oxides, airborne particulate matter and hydrochloride. It contains on different types of particles (carbonated, inorganic) and different sizes [61, 97]. The concentration of air pollutants in the flue gases mainly depends on the combustion regime and the combustion technology, while the emissions of solid particles are determined by the efficiency of the ash collection devices [61].

The open deposition of semi-carbohydrates causes the distribution of pollutants in addition to aqueous trajectories also finished in air (dust) [94]. There are probably links from being in an oil shale area with a greater risk of cancer and asthma than other areas.

The sulfur dioxide remaining in flue gas is still excessive, thus forming the great air pollution problem. Although plants has been equipped with electrostatic precipitators and bag filters, the fly ash concentration in flue gas is still high. The dust particle amounts to about 1% of the oil shale burnt [98].

- *Greenhouse Gas Emission*

Processing of the oil shale is associated with fossil fuel combustion and carbon dioxide emissions. Additional production of this greenhouse gas is due to the high decomposition temperature of the carbonates contained in the oil shale. The oil shale retorting also produces another greenhouse gas, methane. Growing public concern about the negative effects of global warming could lead to a reversal in the development of oil shale [90].

## **1.7 Requirement for Characterization of oil shale**

In summary of the above-presented overview it is possible to bring forward the main factors which should be kept in mind in development of methods of oil shale characterization in industry.

- As a rule, the thickness of individual kukersite beds is only few tens of centimeters and the content of organic matter in different beds vary remarkably.
- Nowadays methods of selective mining as well as oil shale processing in enrichment plants allow remarkably homogenize the quality of oil shale used for further processing but quantitative data (like calorificity, moisture content, etc) become available with a long delay. The calorific bomb method has several steps (sampling, transport, average of the original sample in a detailed sample, grinding, moisture content measurement and finally determination of the calorific value of a bomb) and it takes several hours.
- For efficient work oil retorts and boilers of power plants require a relatively constant quality of raw materials and fuel. In addition, inorganic components in oil shale have a direct impact on the retort/boiler operating conditions. The presence of low melting oxides in the ashes is responsible for the formation of undesired ash deposits, which affect the heat exchange and the overall boiler efficiency.

- At the moment the main outcome of oil shale is the production of liquid and solid energy carriers. Both products have a large impact on the environment and use large amounts of water. A problem of major importance is how to reuse the gaseous, liquid and solid residues and/or make them less hazardous for the environment in accordance with EU regulations.
- Oil shale as a hydrocarbon resource is used for production of fine chemicals and it has a big potential in this field. Developments in this direction need quantitative information about the chemical compounds/elements of the raw material.

On the basis of this information we set a more detailed plan of the study.

First, because of the variable quality of oil shale, on-line information about the integral oil shale characteristics like the gross calorificity and the moisture content is required. True on-line measurements exclude any preliminary preparing of the raw material. As oil shale is a mixture of lumps of organic and inorganic matter with variable properties, the information obtained has a statistical nature and for data processing appropriate mathematical algorithms should be applied.

Secondly, as the efficiency and life-time of retorts and boilers depend on constituents of raw materials, the information about concentrations of inorganic matter helps to choose optimal working regimes of these devices. Besides, the information about the constituents allows to minimize the environmental impact.

Thirdly, methods developed for oil shale studies should be easily applied in another field, for example for analysis of waste material.

Finally, devices applied for measurements should be safe and user friendly.

## 2 Spectral Methods and Data Processing

There are several analytical techniques for raw material analysis. Over the years, standard test methods based on different chemical processes have been established. However, these methods typically use a few grams of raw material's sample from tons of material traveling on a conveyor belt and may not be able to provide representative results due to the inhomogeneity inherent raw material. In addition, it takes several hours to complete an analysis. This obviously hinders real-time requirements.

Currently available on-line analysis methods are X-ray fluorescence (XRF), prompt gamma neutron activation analysis (PGNAA), microwave analysis, near-infrared diffusive reflectance spectroscopy (DRS), and laser-induced breakdown spectroscopy (LIBS). All these methods are non-destructive. Among these, XRF is the analysis of the characteristic emission of secondary X-rays after material bombarding with high energy X-rays. PGNAA analysis records the energy spectrum of  $\gamma$  rays arising by irradiation the sample with a neutrons beam. These methods suffer from low accuracy, radiation risk and the corresponding devices are bulky and have a high cost. The application of microwave technology is limited to the finding of the moisture content. The DRS advantage is the simultaneous analysis of vibrational spectra of many important species. LIBS is a safe method and it needs only optical access to samples without any sample preparation. Besides, LIBS allows all-element detection with high sensitivity [99].

This chapter describes the basic of LIBS and DRS methods. Additionally, an overview is given about the main results of publications where LIBS and DRS are applied for raw material studies.

### 2.1 Laser-Induced Breakdown Spectroscopy (LIBS)

In case of LIBS, the laser radiation causes the heating of a thin layer of the target surface, followed by melting and evaporation of the target material. The evaporated material expands, and because of the high temperature, a plasma is formed in the material plume. This plasma contains electrons, ions, as well as ions and neutral species in excited states. The spectrum of light originating from the excited species in the plasma constitutes is measured by a spectrometer [100]. LIBS is an attractive and effective technique that can be used to detect and characterize material [101].

#### 2.1.1 LIBS Phase

The evolution of the laser-target interaction process passes a number of phases.

Characteristics of these phases depend on many factors like the duration, wavelength and intensity of the laser beam, properties of the target material and properties of the surrounding atmosphere [102].

By varying the laser pulse duration from femtosecond range through pico- and nanoseconds up to the microsecond range, different regimes of laser ablation can be studied. In the case of femtosecond lasers ( $1\text{fs} = 10^{-15}\text{s}$ ), the pulse duration is too short for inducing thermal effects and the ablation is related to non-thermal procedures such as light absorption, plasma formation, non-linear ionization and ablation. In case of picosecond lasers ( $1\text{ps} = 10^{-12}\text{s}$ ) the thermal effects are dominating; the laser energy liquefies and evaporates the sample, and the rise in temperature excites/ionizes atoms. Formed plasma plume remains optically thin i.e. the laser radiation is not absorbed in plasma and it reaches the target surface.

Up to now, most of LIBS studies are carried out with nanosecond ( $1\text{ns} = 10^{-9}\text{s}$ ) lasers. Initial phases of ns LIBS do not differ from that of fs and ps lasers. In its initial stage the plasma temperature reaches several tens of thousands of Kelvin. In between  $10^{-9}\text{s}$  and  $10^{-8}\text{s}$ , the plasma becomes dense to the laser radiation and this is why in later moments the laser radiation is mostly absorbed by the plasma medium [103].

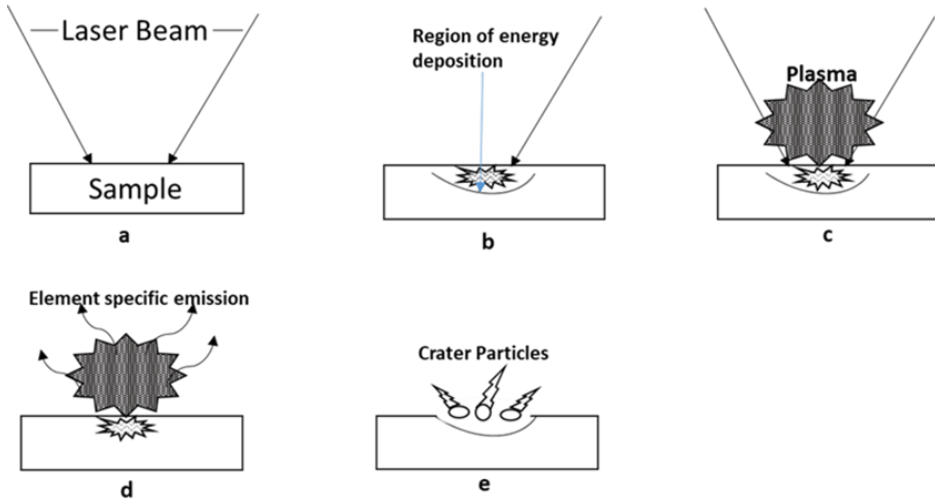


Figure 2.1 Main stages of the LIBS process are depicted in diagrams a-e.

The main stages of a nanosecond LIBS process are depicted in Figure 2.1. At the initial stage (a), a pulse of the laser beam is focused onto the surface of the sample to be examined. At the second phase (b), a thin layer of the target surface is warmed up by the laser radiation and the material starts to evaporate. During the next stage (c) within this material vapor and the surrounding gas atmosphere, a high-temperature plasma plume is generated where the atomization, ionization and excitation of the material constituents takes place. Stages a-c take place while the laser pulse is on. After the end of the laser pulse, at the stage d, the plasma decays and the element-specific radiation starts to dominate in the plasma spectrum. Finally, at the stage e, the crater is formed in the solid sample [12].

From the viewpoint of spectroscopy, the stage d is the most important one because at this stage, the emission of elements is resolved spectrally and it is detected by the spectrometer. The spectrum of the plasma emission has continuous and linear parts. The continuous spectrum is caused by free-free transitions of electrons (bremsstrahlung) as well as by free-bounded transitions of electrons with different bounded energy states of atoms and ions (recombination). Both the plasma spectrum and the plasma density are changing with time. Immediately after the laser pulse, the plasma emits predominantly a continuous spectrum and only small peaks of the spectral lines of atoms and ions are detectable. With the growth of the delay time  $t_d$  from the laser pulse, plasma cools down and the ratio of the peak intensity of spectral lines to the continuous spectrum increases significantly. Alongside with this trend, the width of spectral lines (which had been increased due to the Doppler and Stark effects) becomes smaller, which leads to a better resolution of spectral lines. At the same time the peak intensities of spectral lines are decreasing gradually, which causes the decrease of the signal-to-noise ratio. Thus, from the viewpoint of spectral analysis, there is an optimal value of the delay time  $t_d$ .

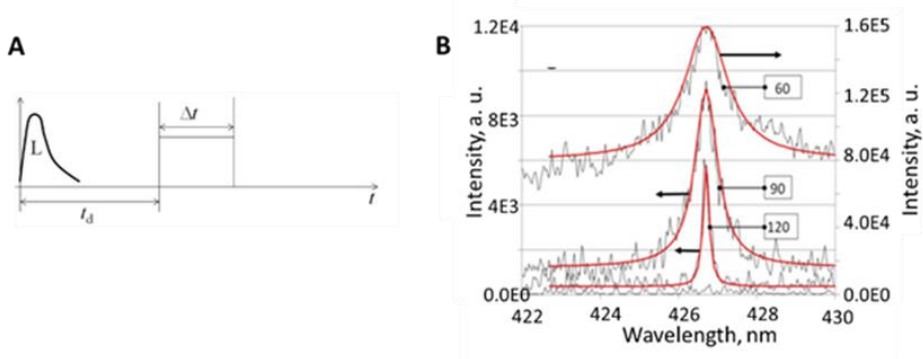


Figure 2.2. A – the method of recording LIBS spectra. B – a spectral line of the carbon ion at different delay times; target – pure graphite; parameter –  $t_d$  in nanoseconds,  $\Delta t = 20$  ns [104].

Figure 2.2A shows schematically the method of recording of LIBS spectra. In this figure, the delay time  $t_d$  is time interval between the laser pulse L and the moment when the spectrum recording starts. During the following time window (time gate) of length  $\Delta t$ , the spectrometer records the spectrum. Figure 2.2B demonstrates how the spectrum recorded within the timegate of length  $\Delta t$  depends on the delay time  $t_d$ . If the delay time  $t_d = 60$  ns, the plasma is still very hot, hence the intensity of the continuous spectrum is dominating. Additionally, because of the high concentration of charge carriers and the high temperature, the  $C^+$  line is very wide. With the growth of  $t_d$ , the contribution of the continuous spectrum becomes smaller, and the line becomes narrower. In the case of the present example, the delay time  $t_d = 120$  ns seems to be the optimal as a further increase of  $t_d$  leads to lower values of the signal-to-noise ratio (SNR).

### 2.1.2 LIBS Technique

The characteristics of LIBS depend on many factors like the sample material, laser energy, laser wavelength and spectral instruments etc.

#### • Laser Energy

LIBS spectra arise when the energetic characteristics of the laser radiation at the target surface exceed certain values. The most important energetic characteristics of the laser beam are the irradiance (intensity)  $I$  and the fluence  $\Phi$ . The irradiance of a laser pulse is the instantaneous power per unit of the target area and its unit in practice is  $W\ cm^{-2}$ , while that of the fluence of a laser pulse is the energy per unit area ( $J\ cm^{-2}$ ) [105]. In case of short laser pulses, the value of fluence is measured experimentally and the value of irradiance is then estimated.

The threshold value of the laser fluence is defined as the minimum fluence needed to detect emission signal from the ablated element. The ablation processes (sublimation, melting, explosion, erosion, etc.) have different fluence thresholds [106]. In case of solid targets and ns lasers, plasma is formed when the fluence reaches the value of several  $J\ cm^{-2}$ .

A comparative investigation of the laser induced plasma threshold of several metals is presented in [107]. The typical threshold level of the irradiance for gases is around  $10^{11}$   $W\ cm^{-2}$  and for liquids, solids, and aerosols are around  $10^{10}$   $W\ cm^{-2}$  [108].

In [109] spectra at five different values of laser energy were measured. Figure 2.3 shows that spectral lines belonging to different energies are almost the same, but their relative intensities changed considerably. Closer examination of time-integrated spectra revealed that the total emission integrated over the entire wavelength range has a linear correlation with the laser fluence.

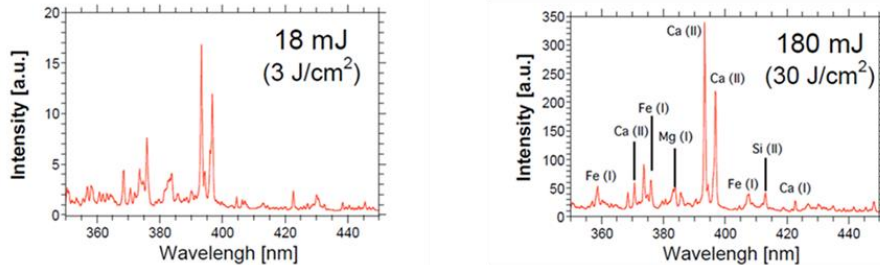


Figure 2.3. LIBS spectra for two values of fluence; laser – Nd:YAG laser (wavelength – 1064 nm ); target – basalt slab [109].

#### • Laser Wavelength

The effect of wavelength on LIBS appears in two ways [110]: the laser-target interaction and laser-plasma interaction.

When the laser-target interaction occurs at shorter wavelength, the photoemission arises and the non-thermal effects are more significant. In general, the shorter the laser wavelength, the higher is the ablation rate and the smaller is the difference between the composition of target elements and the composition of plasma plume elements. This means that there is no elemental fractionation which is the first requirement for a quantitative description of the sample’s composition.

Properties of laser-plasma interaction also depend on wavelength. In the case of a nanosecond laser, two mechanisms of this interaction are important.

The first is the inverse Bremsstrahlung by which free electrons gain energy from the laser beam during photon collisions with atoms and ions. This process increases the plasma lifetime but at the same time also increases the intensity of the continuous spectrum. The inverse Bremsstrahlung mechanism is more efficient at longer laser wavelengths [111]. However, plasma shielding reduces the ablation rate at the target and increases the elemental fractionation in term of redistribution of elements concentrations between solid and plasma phases.

The second process of laser-plasma interaction is the photoionization of excited species and excitation of ground atoms. Photoionization becomes efficient in case of UV lasers.

The most common laser type used in LIBS is pulsed Nd:YAG laser. It can emit light at the wavelength of 1064 nm in the infrared, 532 nm in the visible, 355 nm and 266 nm in the ultraviolet range and its pulse width is between 6 and 15 ns.

Besides Nd:YAG laser, in LIBS studies CO<sub>2</sub> and excimer lasers are used. CO<sub>2</sub> laser emits infrared light at the wavelength of 10600 nm. Excimer lasers radiate mostly in UV region (ArF laser – 193nm, KrF laser – 248 nm XeCl laser – 308 nm).

- **Setup**

Many different LIBS setups are used. An example of a setup applied in LIBS analysis is presented in Figure 2.4.

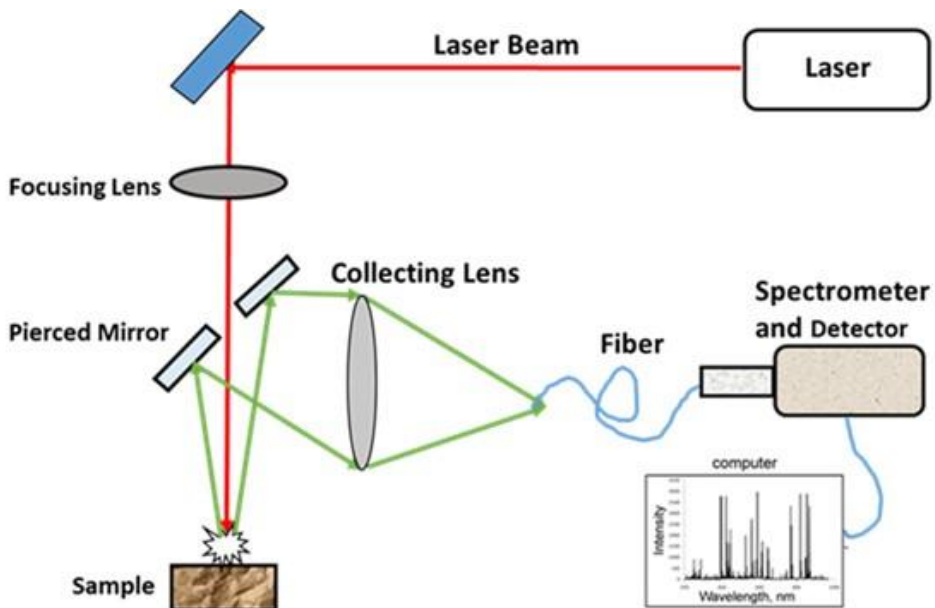


Figure 2.4. Example of LIBS setup.

A high-energy beam of a pulsed laser is focused with a focusing lens to the target surface. To avoid the damage of the mirror, on its way to the target the beam passes an opening in the mirror. To reduce the probability of the gas breakdown in front of the target, the distance between the lens and the target is kept less than the focal length of the lens [112]. Light emitted by the plasma plume reflects from the pierced mirror and then it is collected by the collecting lens to the end of the fiber optics. The fiber optics delivers the light signals to the entrance slit of a spectrometer.

Finally, a computer processes the obtained spectrum.

- **Spectrometers and Detectors**

Spectrometers are devices that disperse the emitted radiation to get a spectrum in terms of intensity as a function of the wavelength. Different types of spectrometers are used for recording of LIBS spectra. In the case of the analysis of samples with a multi-elemental composition with spectral lines in a wide wavelength range, it is suitable to use echelle spectrometers which have a large spectral bandpass and a high spectral resolution at the same time [113]. The two dispersive elements of the echelle spectrometer are arranged to disperse the light in two perpendicular directions. A high spectral resolution is achieved by recording the spectrum at high diffraction orders of an echelle grating. To separate the diffraction orders, a second perpendicularly mounted cross-dispersive element e.g. prism is used. Such setup results to the spectrum consisting a number of parallel rows where each row corresponds to a certain wavelength interval.

This 2-dimensional spectrum is recorded by a charge coupled device (CCD) which is a matrix of photosensors. Incident photons with sufficient energy are absorbed in

photosensors and liberate electrons which can be stored and detected. CCD matrix is coupled with an image intensifier. Besides the signals amplification, the image intensifier allows to set the time-gate during which the spectrum is recorded [110, 113].

### 2.1.3 Quantitative Analysis by LIBS

Aim of the quantitative analysis is to find concentrations of different material components.

The simplest way is to use calibration curves, which gives the dependence of a spectral line intensity of an element on its concentration. For this purpose, a set of samples with known concentrations is needed. In the ideal case, we need just one spectral line characterizing component which concentration we want to know. Besides, if the dependence of the intensity on the concentration is a linear one, it is easy to find unknown concentrations. However, there are many factors which cause substantial deviations from this ideal case [108]. The main factors are:

(i) Fundamental and instrumental noise. Some level of noise can never be eliminated, because:

It results from the particulate nature of matter and light; this is the fundamental noise. However, excess noise comes from imperfections in equipment, instrumentation, conditions, etc., and theoretically can be minimized or eliminated [114].

An appearance of this noise are fluctuations of the peak value of a spectral line intensity. A way to minimize this effect is to characterize a spectral line by its integral intensity, which equals to the integral of the intensity over the half width of the line.

(ii) LIBS also suffers from poor shot-to-shot reproducibility, which can be affected by many aspects: laser pulse instability, plasma and sample interaction, properties of the sample (the sample itself may be inhomogeneous), and environmental factors.

To reduce the effect of these factors, instead of a single spectrum for a single laser shot, a series of shots is fired and a series of single-shot spectra is recorded. Then, the average, standard deviation and relative standard deviation (RSD) for the intensity values corresponding to each recorded spectral line are calculated. An example of an RSD plot is shown in Figure 2.5. We see that the increase of the number of the laser shots reduces the shot-to-shot variation effects on emission and the RSD value will be stable when there are more than 80 shots.

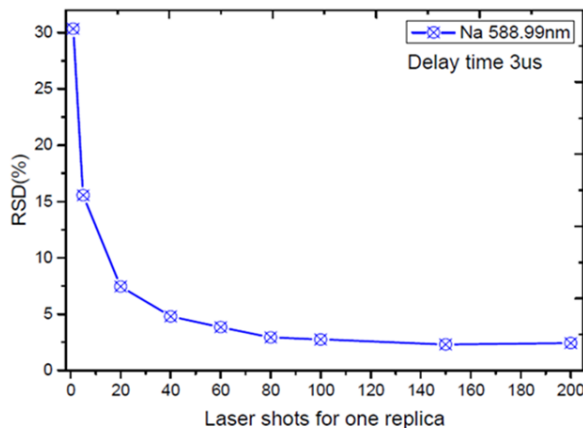


Figure 2.5. RSD of the Na (588.99 nm) line versus the number of laser shots [115].

In Figure 2.6 is an example of the calibration curve, when only factors (i) and (ii) are the dominating ones. We see that the result of the least square regression for the integral (net) intensity of a single spectral line (univariate regression) gives a linear calibration curve with a high correlation coefficient.

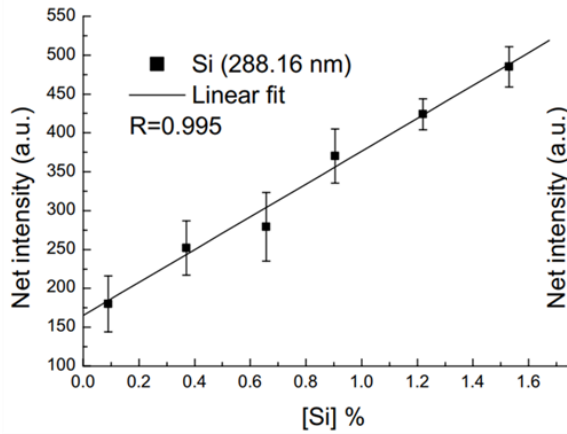


Figure 2.6. Calibration curve for quantitative analysis of Si in aluminum alloys, the curve is an average of 6 laser shots [116].

In cases when the intensity of spectral lines is comparable to that of the noise or spectral lines are partly overlapped, a studied element should be characterized by a number of spectral lines i.e. a multivariate least square regression is applied for building of a calibration curve.

(iii) The light emitted by the central hotter part of the plasma plume is partly absorbed by the colder outer part of plasma. This self-absorption phenomenon breaks the concentration-caused growth of the intensity and the absorption could even cause the appearance of a dip in the center of the lines as Figure 2.7 shows for Mg II line. As a result, calibration curves have a trend of saturation, Figure 2.8. As the non-linearity is different for different lines, the multivariate analysis can give wrong results.

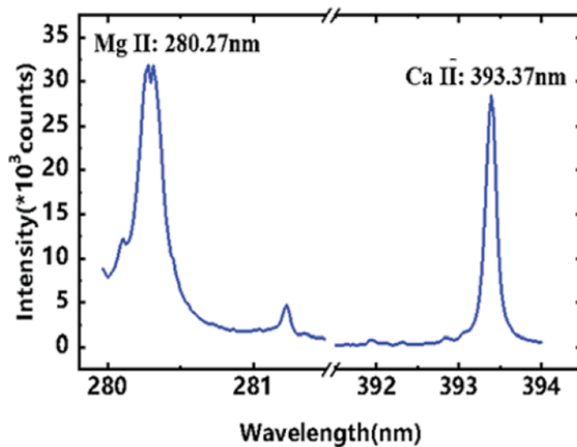


Figure 2.7. Because of reabsorption appears a dip at the center of Mg II line [117].

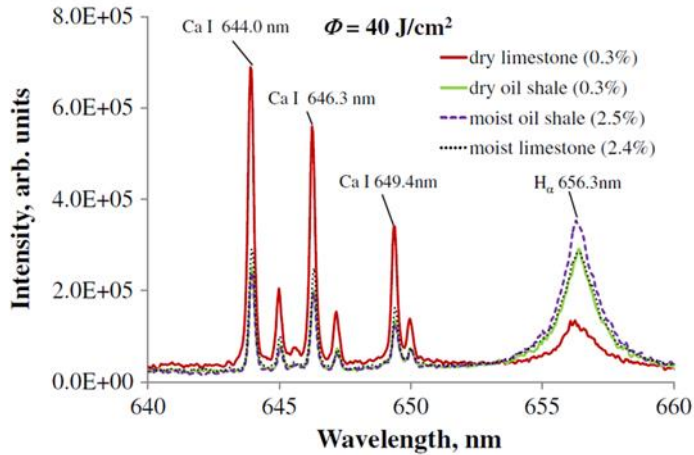


Figure 2.8. Because of self-absorption, intensities of the Fe I lines grow with the concentration slower than linearly [118].

(iv) Usually, the intensities of the spectral lines of an element depend also on the concentrations of other species in the sample. This matrix effect means that the intensity of a spectral line of an element is now a function of the concentrations of several species.

Figure 2.9 demonstrates the dependence of limestone and oil shale spectra on moisture content.

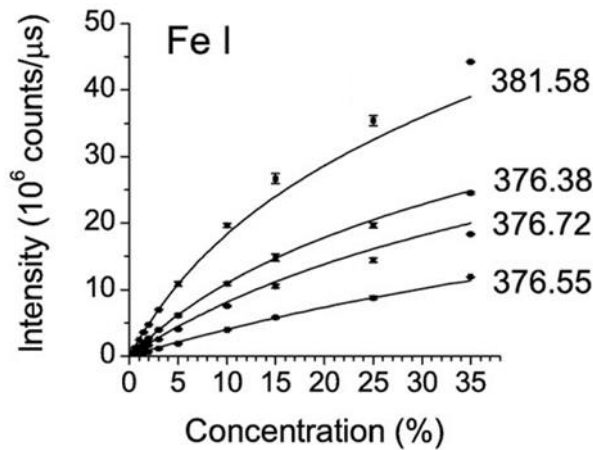


Figure 2.9. Dependence of limestone and oil shale spectra on moisture content [119].

As expected, the intensity of H<sub>α</sub> line increases with the growth of moisture content. At the same time, the moisture growth also reduces drastically the intensity of Ca I lines of the limestone and only on the basis of these data it is impossible to make conclusions about the content of the organic matter in the material.

For quantitative analysis, it is necessary to prepare standards that are similar to the matrix of the unknown (test) sample and obtain calibration curves for different elements [120].

A common way to improve the correlation between the spectral lines intensities and elemental concentrations is the normalization procedure [121]. In case of external normalization, the spectrum is compared with a reference signal like LIBS-induced acoustical signal. In case of internal normalization, the intensity of a spectral line which is used for determining the concentration is compared with that of a line whose intensity is independent of that concentration. When there are no chemical element with a constant concentration the spectral lines of which could provide such a reference, the spectral line intensities can be normalised to the total intensity  $I_T = \int_{\lambda_{min}}^{\lambda_{max}} I(\lambda) d\lambda$ , where  $\lambda_{min}$  and  $\lambda_{max}$  are the shortest and longest wavelengths of the spectral range of the spectrometer.

#### 2.1.4 Data Processing Algorithms

There are several fast and powerful algorithms which can be used for further processing of LIBS data. In essence, these are modifications of multivariate analysis based on least square regression. Here only some of these algorithms are described.

The model of multiple linear regression assumes that a dependent variable  $Q$  (calorific value, concentration of an element, etc) is given by a linear combination of independent variables  $I_i$  (intensity of a spectral line of an element)

$$Q = \sum_i k_i I_i$$

and a least squares method is used to calculate the coefficients  $k_i$ .

In LIBS the number of samples with different  $Q$  is limited and the selection of spectral lines is important for multiple linear regression modeling [122]. A limitation of the ordinary least square approach is the assumption that all the variables can be considered as observables. Besides, problems arise when the independent variables in the regression model are highly correlated to each other. This multicollinearity makes it difficult to interpret the obtained results.

The idea of principal component analysis (PCA) is to reduce the number of variables of a data set while preserving as much information as possible. PCA operates with new (standardized) variables

$$z = \frac{x - \bar{x}}{s_x},$$

where  $\bar{x}$  is the mean value of variable  $x$  and  $s_x$  is its standard deviation. PCA uses orthogonal transformation to convert a set of observations of possibly correlated variables into a set of values of linearly uncorrelated variables. The first principal component (PC) has the greatest possible variance, and each successive element, in turn, has the highest possible variance as long as it is orthogonal to the previous components [123]. The resulting vectors form an uncorrelated orthogonal basis set. PCs are then used as input variables for regression.

Partial least square regression (PLSR) has some resemblance to PC regression. PLS is used to find the fundamental relationships between two arrays ( $X$  and  $Y$ ) i.e. it is a latent variable approach. Most of the variants of PLS assume a linear regression between  $X$  and  $Y$ . Being a statistical method, PLS ignores the physical background of LIBS measurement and is mostly dependent on statistical correlation or curve fitting, which may lead to over-fitting the noise and eventually ruining the measurement accuracy for samples outside the matrix of the calibration sample set. Additional limitation related to PLS is that it could not satisfactorily reflect the non-linear relationship between variables [124].

Dominant-factor-based PLS mode combines the physical processes with the PLS regression which improves the accuracy of data analysis. In [125] a conventional univariate model with the background was applied to model the major concentration information (called the dominant factor) and PLS was further applied to compensate for residual errors in the dominant factor.

A fundamentally different way to find the unknown concentrations is the so-called calibration-free LIBS [126] the application of which needs the knowledge of the basic plasma characteristics (plasma temperature, electron concentration). This method assumes that there is a local thermal equilibrium in the plasma. In industrial conditions and for complex samples, such as the oil shale, the application of this method is not justified.

### **2.1.5 Application of LIBS in the Analysis of Different Raw Ores**

Properties of LIBS allow the application of this technique for fast and online process control in industry. The application of LIBS for the characterization of mining products has been presented in different papers. Recent overview [99] sums up the research contributions utilizing LIBS for coal analysis, including fundamentals and key factors, operation modes, data processing, and analytical results. In industry three LIBS set-up modes are used. In case of the inline mode the device is placed over the coal conveyor belt or besides the coal powder flow, where the analyzed coal form is the same as that in the coal stream, without pellet preparation (i.e., no sampling system is required to feed the analyzer). In the case of the at-line analysis, the LIBS system is compared with the automated sampling system which takes the coal sample from the belt, grinds, mixes, presses it into a pellet, analyzes, and finally sends it back to the coal stream. The offline LIBS set up is the same as by a laboratory analysis, but it is located near the coal utilization line where the sample handling is manually operated.

To realize a real-time online analysis, the most convenient way is to use an inline analyzer shooting the laser directly onto the lumps or powder of the raw material on a conveyor belt. However, this configuration usually suffers from severe measurement errors and has a high uncertainty.

Examples of the design and results of the inline mode are described in [127, 128, 129]. In [127] the measuring system has been designed to operate on the top of conveyor belts that carry the raw coal in coal fired power plants, where both the average distance and the spatial configuration of the raw coal on the conveyor belt continuously change during signal acquisition. To replicate this situation at a laboratory level, the coal samples (in the form of a raw material) are sequentially positioned under the measuring head by means of a translational/rotation unit. Measurements have been carried out on different coal samples (in the form of a raw material) with known chemical composition. Calibration curves of both major elements (such as carbon and hydrogen) and minor constituent (such as aluminum, calcium, iron and silicon) have been derived from the analysis of the recorded LIBS spectra. In this study, the experimental results show that both carbon and hydrogen concentration as well as the content of some inorganic components (Al, Ca, Fe, Si) can be evaluated with a good accuracy.

In [128] the LIBS analyzer determined the quality of coal on a moving belt conveyor in field conditions with the accuracy acceptable for the coal industry. The LIBS system was installed in line with a PGNA system and laboratory data served as a referee in the final assessment for analytical accuracy. The results show that there is a good correlation between the data of the two inline units, while the LIBS technique has a significant

advantage in that the PGNA system is very bulky and the neutron source represents potential health hazards that require strict regulatory demands. The performance of the unit was calculated and the results were found to be statistically valid. The successful results were achieved for accurate (at least  $\pm 0.5\%$  mean absolute error) online coal ash content monitoring; the average standard error was only 0.32%.

The study [129] shows the ability of LIBS to provide inline analyses for raw ores (phosphate and coal) in field conditions. Samples of phosphates production pebble were obtained from the pebble product belt. Samples of coal with known concentrations of impurities and ash content were utilized. An industrial LIBS machine was developed and successfully tested for on-belt evaluation of phosphate, measuring Mg, Fe, Al, bone phosphate lime, insoluble phase and metal impurity ratio, as well as for evaluation of coal, measuring its ash content. The comparison of the LIBS inline data with the values from the reference analysis shows a good correlation satisfying the required detection limits and accuracy.

Results of [130] present an example of at-line analysis; in this study, designed instrumental variation on LIBS allows simultaneous determination of all detectable elements by utilizing multiple spectrographs and CCD detectors. The device determined the elemental composition of bulk materials with a high accuracy. The system was suitable for the analysis of heterogeneous materials such as coal and mineral ores. In coal analysis, detectable elements included the key inorganic components of coal, such as Al, Si, Mg, Ca, Fe, Na, K, C and H. Coal and mineral samples received from the mines, crushed and mixed prior to the analysis. For moist material, only light crushing was required, however for hard material, the samples were crushed to a fine powder with the granule size less than 100  $\mu\text{m}$  to obtain results. For each sample positioned on a fast translation stage, up to 300 surface laser shots were recorded. The instrument was able automatically construct the calibration curve by univariate regression over the elemental concentration range. Detection limits vary depending on the specific element but are typically on the order of 0.01% by weight for heterogeneous materials such as the moist materials. Measurement repeatability and accuracy are typically within  $\pm 10\%$  which is similar to the results from standard analysis procedures for heterogeneous materials.

Results of the off-line measurements described in [131] where both LIBS and thermo-gravimetric analysis (TGA) (it continuously measures mass while the temperature of a sample is changed over time) were applied for predicting the slagging propensity of coal and coal blends. Coal samples from various mines were milled to particle sizes  $\leq 75 \mu\text{m}$ . For the LIBS analysis, coal or blend was compacted into a pellet. For TGA, the coal and blends were ashed in an oven for 7 hours under 750  $^{\circ}\text{C}$  and corresponding laboratory ash were analyzed by mentioned techniques and results were compared to standard laboratory methods. The indices of slagging, which predict the tendency of coal ash deposition on the boiler walls were determined. The LIBS technique provided fast and precise elemental detection of C, H, Si, Al, Fe, Ti, Ca, Mg, Na, K, Mn, Sr, and Ba elements without ashing, TGA analysis was applied to calculate the slagging indices.

Results of [132] belongs also to off-line setup. In this study, LIBS has been applied for the quantitative analysis of the ash content of coal. A series of coal powder samples were compressed into pellets and prepared for LIBS measurements. Results of the data processing show a good agreement between the ash content provided by TGA and the LIBS measurements. The relative error of prediction, RSD, and limit of detection were 6.94 wt%, 8.50%, and 1.73 wt%, respectively.

Results of the study [133] show the effects of moisture content variations on the spectra and properties of the laser-induced plasma. LIBS method was used for off-line coal analysis. To obtain samples with different moisture contents, the coal sample was mixed with a certain moisture content and then was pressed into three pellets with the same moisture content. One was used for LIBS analysis, and the two pellets used for moisture analysis were mashed into small pieces and then divided into three or four parts for moisture measurement. The deviations of the data met the national standard which verified that the sample preparation method could ensure homogeneous distribution of water. The moisture content of the samples varied from 1.19% to 22.25%. It was found that most of the spectral line intensities decreased as the moisture content increased, even including those of H and O. Additionally, the values of RSD of those lines increased also with increasing moisture content. Decreased intensities of the lines were explained by an extra energy needed for dissociation and ionization of the water vapor. This means that if the moisture content increases, the less coal mass is removed in the plasma, resulting in lower line intensities.

In Ref. [134], LIBS was applied for analyzing coal properties, including calorific value, ash content and volatile matter content. 53 coal samples were collected from different mines for the analysis. The off-line analysis was made with air dried samples. Calorific values were determined using an oxygen-bomb calorimeter; whereas moisture, volatile matter, and ash contents were measured using a TMA method. A total of 40 samples were selected as calibration samples and the remaining 13 samples were selected for the prediction. In data processing, the dominant factor modeled the direct correlation between coal properties and spectral line intensities, whereas residual errors were corrected by a secondary PLS method with a full spectral information. Compared with the conventional PLS model, an overall improvement was obtained for the dominant factor based PLS model. This finding can be attributed to the direct modeling of the physical mechanisms between the spectral information and the coal properties.

Unlike in the case of coal studies, only a few papers deals with oil shale characterization by LIBS.

Study [135] presents results about shale geochemical and mineralogical analysis by LIBS, in which a laser is used to rapidly pyrolyze shales in argon medium and the changes in sample elemental composition during pyrolysis are monitored through optical emission spectroscopy. This is similar to the laser-induced pyrolysis which has been used to characterize shales. In case of laser induced pyrolysis the volatized products are collected and further analyzed using gas chromatography and mass spectroscopy. Laser induced pyrolysis has been used to provide total organic carbon information, but not other geochemical parameters nor mineralogy, making LIBS a more complete assessment of organic and inorganic geochemistry. Measurements were made on 145 shale samples from multiple formations across several continents. Multivariate analysis has been applied to the LIBS spectra to predict both organic geochemistry and mineralogy. Data shows a good correlation and linear dependence between the total organic carbon content and predictions by LIBS.

In Ref. [136], the LIBS methods were applied to measurements of kerogen hydrogen-to-carbon elemental ratios in mud rocks and shales. Measurements were performed on whole rock samples that had been pulverized and pelletized to correspond to the homogenized rock samples used to obtain kerogen isolates. A sequence of laser shots was applied to samples and intensities of H and C lines as a function of time was found. The predicted H/C ratios of kerogen from the LIBS measurements of whole rock

samples correlated well ( $R^2 = 0.99$ ) with the values determined for kerogen isolates measured by atomic elemental analysis, although prediction of mass elemental ratios is also possible by this method.

In Ref. [137], LIBS was used for finding the elemental composition of samples from the Marcellus Shale. Ten powdered samples pressed to form pellets and used for LIBS analysis. Major elements (Al, Ca, Si, Mg, Ti, and C) in shale rocks were analyzed qualitatively and quantitatively. LIBS also offered the possibility of quantifying the carbon content. Relative errors of the LIBS measurements were in the range of 1.7 to 12.6%.

## 2.2 Diffuse Reflectance Spectroscopy (DRS)

LIBS spectra in visible and UV regions reflect electronic transitions between atoms and ions of elements of ablated sample material. Differently from LIBS, DRS spectra in the near infrared region (NIR, 700–2500 nm) are related to transitions between vibrational energy states, thus giving information about molecular bonds. Traditionally, in the NIR region the radiation is characterized by its wavenumber – reciprocal of the wavelength  $\lambda^{-1}$ . Thus, the wavelengths 700–2500 nm correspond to the wavenumbers 14300–4000  $\text{cm}^{-1}$ .

According to quantum mechanics, discrete energy levels of vibrational states are defined by the formula  $E_n = (n + 1/2)h\nu$ , where  $n$  is the vibrational quantum number and  $\nu$  is the fundamental vibrational frequency which is determined by the properties of the molecule. In oil shale, the most important molecules contain C-H, N-H, S-H or O-H bonds for which overtone bands ( $\Delta n = \pm 2, \pm 3 \dots$ ) belong to the 700-2500 nm range. Because of high anharmonicity of these bands the NIR radiation is absorbed by the matter and the information about the properties is obtained [138, 139].

### 2.2.1 DRS Principle

In the case of DRS, broadband light falling onto the surface of a sample is partly absorbed, another part of it undergoes specular reflection (mirror-like reflection) at the surface, and the remaining part is scattered and after multiple reflections may return back to the surface [140], Figure 2.10.

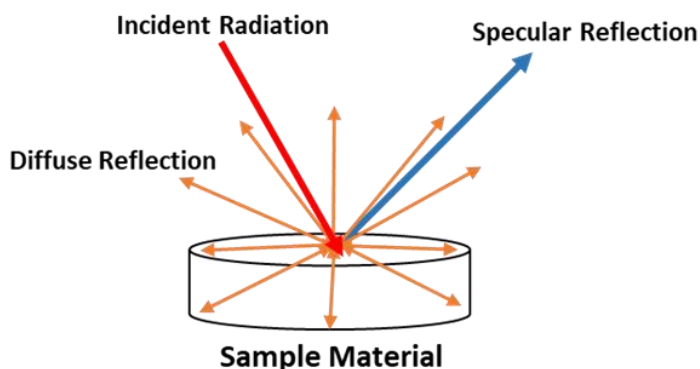


Figure 2.10. Distribution of the incident light.

When the sample surface is not polished, the diffuse reflection is the dominating type of reflection. As some of the light is absorbed by the sample, only a part of incident light is reflected, stronger absorption leads to a smaller reflection. On the other hand, when

the sample exhibits weak absorption then the total intensity of the scattered light differs only slightly from that of the incident light. This means that the absorption and reflectance spectra are complement to each other, and the former can be deduced from the latter. The reflection spectrum is obtained by comparing the intensity of the light reflected by the sample with the intensity of the light reflected by a reference etalon, and is commonly expressed as the percent reflectance (%R), defined as

$$\%R = (I_s/I_r)R_r$$

Here  $I_s$  denotes the intensity of the reflected light from the sample,  $I_r$  is the intensity of the reflected light from the standard reflector, and  $R_r$  is the percent reflectance of the etalon. As a rule, there is no linear relationship between the diffuse reflectance and absorption spectra; several models have been developed for describing this nonlinear relationship [141].

### 2.2.2 DRS Technique

The characteristics of DRS depend on many factors, such as the particle size, refractive index, homogeneity, packing, reflectance, the specifics of the measurement procedure and of the spectral instruments etc.

- **Measuring the Reflectance of Samples by collecting the Diffused Radiation**

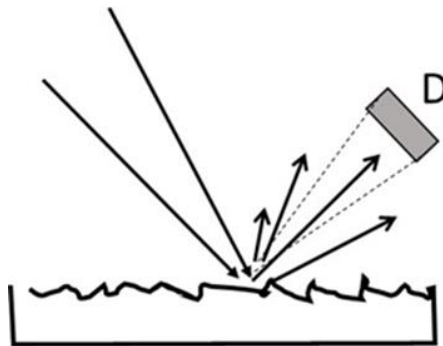


Figure 2.11. Sketch of the experimental setup. Detector D collects only a part of reflected light.

Figure 2.11 illustrates problems met when DRS spectra are being recorded: the detector collects only a part of the diffused light, within a limited solid angle. This arrangement works well if the sample is microscopically homogeneous and the fraction of light scattered towards the detector remains constant. However, when this condition is not fulfilled and the sample is moved, the focused beam will see a different part of the sample resulting in measurement-to-measurement differences; as a result, the SNR can be reduced significantly. In reality, samples are usually inhomogeneous, either because they are mixtures of different substances, or because they have a particle size comparable to the diameter of the detection beam. Therefore, to achieve an acceptable SNR, a large enough solid angle of detection is required. Thus, a device is needed which collects all the reflected light evenly from a sample. Usually, integrating spheres are used for this purpose which satisfy the following conditions [142].

- Both specular and diffuse reflected light is captured reliably.
- Reflectance is uniformly detected, even when the sample is inhomogeneous.

- Integral reflectance is measured correctly even for samples which reflect light anisotropically, in preferred directions.
- The effect of polarized light (caused by reflections from the sample and by the polarization of the illuminating beam) is reduced.
- It is possible to measure the absolute reflectance.

Figure 2.12 illustrate how the integrating sphere is used by Infrared Multi-Purpose analyzer [143].

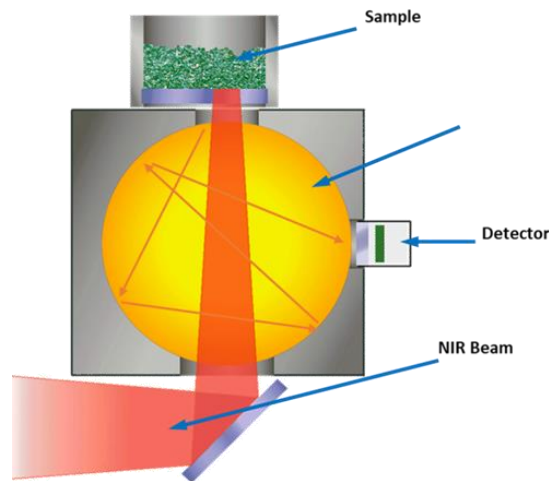


Figure 2.12. An example of DRS setup using an integrating sphere [143].

The integrating sphere is a hollow sphere coated internally with a matte finish; different types material are used (in our case, with gold). The coating on the inner surface of the sphere is a very diffuse coating with high reflectance in order to deliver a consistent integration of light and low absorbance losses. The sphere has ports – openings for an incoming beam of light, for a sample specimen and for a detector.

The incident light of broad-band spectrum hits the heterogeneous sample positioned in the rotating holder and the diffusely reflected light enters the integrating sphere. The entering light is scattered uniformly around the interior of the sphere through multiple reflections on the diffuse internal sphere coating. The resulting diffused light is detected at a port configured with a detector device.

The detector is a part of the Fourier transform infrared spectrometer (FTIR).

#### • Fourier Transform Infrared Spectrometer (FTIR)

In the modern devices for recording NIR spectra, mainly FTIR spectrometers are used. FTIR is based on the Michelson interferometer setup, shown in Figure 2.13.

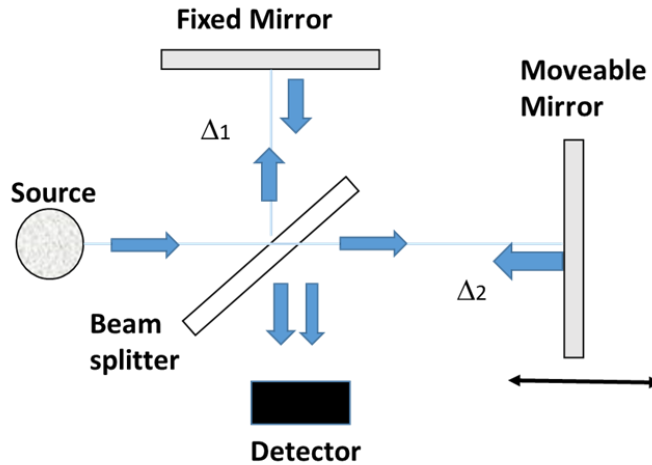


Figure 2.13. Michelson interferometer setup.

An interferometer consists of a beam splitter, a fixed mirror, and a moving mirror which can be moved very precisely back and forth. The beam splitter transmits half of the radiation striking it, and reflects the other half. Radiation from the source strikes the beam splitter and is divided into two beams. One beam is transmitted through the beam splitter to the fixed mirror and the second one is reflected off the beam splitter to the moving mirror.

When the fixed and moveable mirrors are equidistant from the beam splitter i.e. the optical path difference (retardation) is  $\Delta_1 - \Delta_2 = \delta = 0$  then the two beams are said to be in phase and constructive interference is produced. The intensity at the detector is equal to the intensity of the source. This condition is called zero path difference (ZPD). The beams meet in phase also when the optical path difference is an integer multiple of wavelength,  $n\lambda$ .

If the movable mirror is moved away, one light beam has to travel an additional distance (back and forth) and when  $\delta = \lambda/2$  or  $(2n + 1)\lambda/2$  ( $n = 0, 1, 2, \dots$ ), the two beams are said to be out of phase and destructive interference takes place. The intensity at the detector  $I_\delta$  is equal to zero.

The intensity  $I_\delta$  changes smoothly between these extreme values and is a sinusoidal function of the position of the movable mirror, and of the optical path difference  $\delta$ :

$$I_\delta = \frac{I_0}{2} \left[ 1 + \cos\left(\frac{2\pi}{\lambda} \delta\right) \right]$$

where  $I_0$  is the intensity of the source.

The intensity  $I_\delta$  as a function of the retardation  $\delta$  is called the interferogram. Each unique spectral component of wavelength  $\lambda$  contributes a single sinusoid with a frequency (wavenumber) inversely proportional to its wavelength. The period in the recorded interferogram depends on the light wavelength, the longer is the wavelength the larger is the period in the interferogram. For a broadband signal, the peak intensities of different wavelengths coincide only at ZPD.

When the optical path difference increases, different wavelengths produce peak readings at different positions, they never again reach their peaks at the same time.

Thus, as we move away from the central burst, the interferogram becomes a complex oscillatory signal with decreasing amplitude.

Once an interferogram  $I_{\delta}$  is collected, it needs to be translated into a spectrum (emission, absorption, transmission, etc.). This operation is realized by the Fast Fourier Transform algorithm, which transfers the intensity dependence on path difference into the intensity dependence on the wavenumber [144, 145].

### **2.2.3 Applications of Diffuse Reflectance NIR Spectroscopy in the analysis of different raw materials**

Near-infrared (NIR) spectroscopy is the fastest-growing and the most versatile analytical technique that can be implemented with little or no sample preparation and thus is well suited to applications such as process monitoring, materials science, medical uses, as well as in the industry [146, 147]

Examples of diffuse reflection spectroscopy in the analysis of raw materials are described in [148–151].

In the study [148], a mock-up of the conveyor belt was used. Different classes of samples (straw, coal, straw-coal blend) were tested. The straw samples were chopped to less than 80 mm in length until air drying and cleaning. After ground in mill, coal samples were passed through a 10 mm sieve and straw-coal blends of varying straw content were prepared for the experiment. All the classes of samples were stored in zip-lock plastic bags in a dry and shaded location until use. NIR spectra of prepared samples were acquired by an online measurement system consisting of a conveyor, a holder, a computer and a NIR spectrometer. Linear discriminant analysis was used for qualitative analysis and partial least squares regression was used for quantitative analysis. The NIR qualitative and quantitative analysis models of straw-coal blends were developed and compared at different level of conveyor belt speed and spectrometer installation height for establish the conditions of on-line NIR measurement. Changing the spectrometer installation height resulted in a spectrum shift, but the shift could be removed by pretreatment derivatives. The optimum value of height and speed was found. In general, the lower the conveyor speed, the more accurate and robust the model.

In studies [149, 150], a rapid analysis based on NIR spectroscopy was carried out in coal samples coming from several origins. 142 samples of coal from different suppliers were used. Some of them were raw coal coming from mines and other from power stations. All of the samples follow particle size specifications for pulverized coal burners. They were analyzed for moisture, ash, volatile matter, fixed carbon, heating value, carbon, hydrogen, nitrogen and sulfur by usual ISO standard methods. A sample was positioned in a diffuse reflectance sample cup (see Figure 2.12) and the instrument was controlled by software. NIR spectra in 1100–2500 nm range were obtained in absorbance and reflectance units.

Analytical and spectral values of samples differed significantly. Improving the calibration and prediction errors was achieved by dividing samples into clusters. The sample clusters were determined based on the values of the characteristics and spectral data. . Once the clusters were established, the discrimination between the clusters was performed via a linear discriminant analysis. The results showed that for some clusters, the characteristics of an organic coal matter, such as the content of volatile matter, heating value, fixed carbon, carbon content, can be determined with relative uncertainties around 1–3%, and therefore, the method is suitable for applying in an online system. The used calibration and classification methods made it possible to

calculate the characteristics of the coal with an accuracy similar or even better than when commercial online analyzers were used. This shows that the -NIR spectroscopy is a valid option for this task.

In the study [151], DRS technique was used for predicting the oil yield from oil shale samples. More than fifty oil shale samples were supplied with the compositional analysis by X-ray diffraction, and measures of the expected oil yield. Each sample was mixed mechanically and ground in a grinder. The samples were dried at 105 °C. A constant mass of each sample was placed on the sample cup (see Figure 2.12). Spectra in the range of 2500–13000 nm ( $4000\text{ cm}^{-1}$ – $769\text{ cm}^{-1}$ ) were recorded by FTIR, Figure 2.14. As one can see, the raw spectra are not very informative, but upon taking the second derivate of these spectra, it was possible to pinpoint the most characteristic bands of the spectrum. The principal spectral features emerge due to the combinations and overtones of the fundamental frequency of O-H and C-H absorption lines. The hydroxyl bands are found at 1900 and 2200 nm and are attributed to combination bands of non-bonded and bonded –OH complex, respectively. As the oil shale samples had been dried (at 105 °C) when received, absorption of atmospheric moisture could have taken place during the sample preparation. This can be the reason for the presence of the non-bonded –OH band at 1900 nm. Two bands appearing at 1728 and 1758 nm are attributable to the aromatic –CH, to the –CH<sub>2</sub> and to the –CH<sub>3</sub> combination bands. The bands at 2305 and 2348 nm are most likely due to aliphatics in the oil shale or aromatic –CH and –CC bands.

The intensity of the hydrocarbon spectral bands increased when the oil yield was increased. This made it possible to predict the oil yield with the relative uncertainty of 9%.

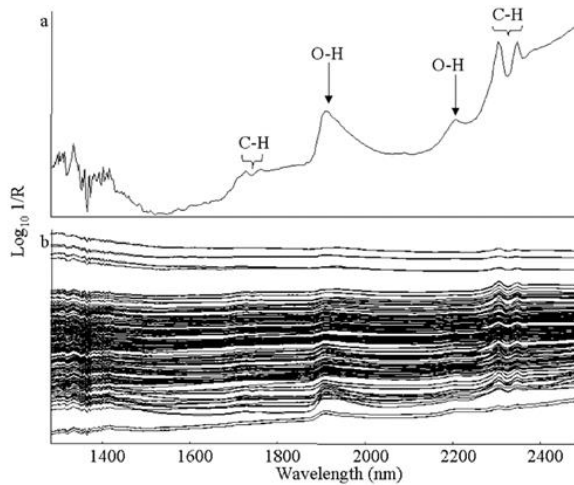


Figure 2.14. Graph a shows the second derivate of the averaged raw spectra. Graph b shows 212 diffuse reflectance raw spectra [151].

## 3 Experimental Methods

### 3.1 Samples

In LIBS studies overall three different types of samples were tested. The first preliminary measurements were made with single large-scale oil shale lumps of approximately ten centimetre in size. The next cycle of studies was carried out with air-dry samples of powder pellets. In the main cycle of measurements, crushed samples with the different values of the calorificity and the moisture content were used.

In DRS measurements the same set of crushed oil shale samples as in case of LIBS has been used but the method of changing the moisture content was slightly different.

#### 3.1.1 Powder Samples

A set of 10 samples of ground oil shale with different calorific values was prepared by the laboratory of Mines of Estonian Energy (EE), the grain size of these raw samples was below 0.1 mm. The samples represent commercial oil shale from the enrichment plant with the calorific value ranging from 6.3 to 11.6 MJkg<sup>-1</sup>, as it was determined by calorific bomb method. Using the same method, the measurements of the calorific value were repeated in the laboratory of Virumaa College of Tallinn University of Technology (PKK). Besides, in the latter laboratory the mass percentages of the main chemical composites of the samples were determined using standardized methods. In Figures 3.1A and 3.1B, the calorific values of the dry samples are presented as a function of the samples' number *s*; the data are taken from the Table 1 of the publication [P I].

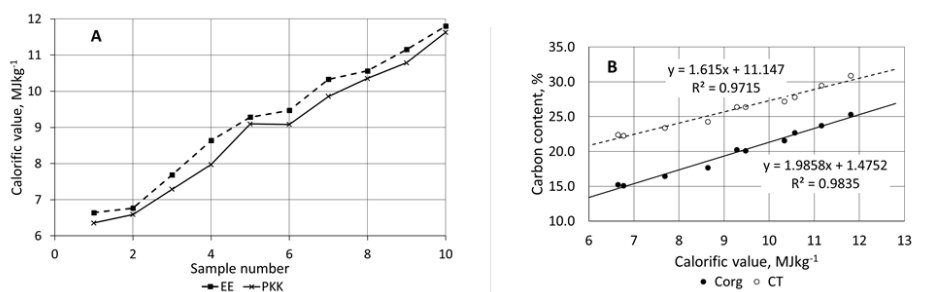


Figure 3.1. A – Calorific values of powder samples as measured by the two laboratories. The laboratory of Mines of Estonian Energy and the laboratory of Virumaa College of TalTech. B – the percentage of total carbon  $C_T$  (dashed line) and organic carbon  $C_{Org}$  (solid line) versus calorific value.

Figure 3.1A shows that calorific values follow almost a linear dependence on the sample number but the values determined in different laboratories have a systematic shift by  $\approx 4\%$ . Figure 3.1B confirms that, as expected, the coefficient of determination between the  $C_{Org}$  and calorific value is high, and shows that  $C_T$  is also strongly correlated with the calorificity.

A part of each sample was additionally grinded using mortar and pestle to particle size smaller than 60  $\mu\text{m}$ . Samples were pelletised without any binder, adding only 5 mass percentages (wt%) of distilled water to the air-dry powders. Powders were pressed into 25mm in diameter and approximately 6mm thick pellets under 18 tons held for 5 min. Four pellets from each sample were pressed. Thus, altogether 40 pellets were prepared. Example of pellets are presented in Figure 3.2.

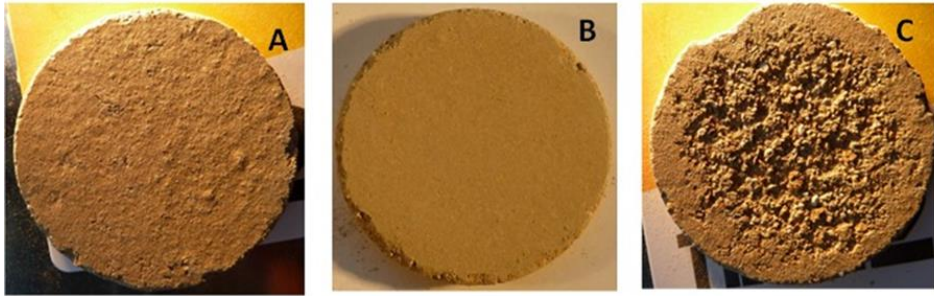


Figure 3.2. A – pellet from raw grinded powder; B – pellet from fine grinded powder; C – pellet after a number of laser shots.

Before the LIBS measurements, pellets were stored at the room temperature of 21 °C and at the relative humidity of ca 30% during a week to balance the water content of samples with the ambient humidity. The moisture content in these air-dry pellets was approximately 2 wt%.

### 3.1.2 Crushed Specimens

A detailed report of the collection of crushed specimens is presented in [152]. In what follows only the main data of the set of samples are presented.

Crushed specimens were collected by an exploration geologist from the Narva open cast mine, Estonia, from different layers of the oil shale and limestone interlayers A–F<sub>2</sub>. Altogether 11 specimens from different layers of oil shale and limestone interlayers were taken. In addition, 4 specimens were taken from the stopped conveyor belt of an enrichment plant of the underground mine “Estonia”. In the Table 3.1 these specimens are labelled by EST together with the daily average of the net calorific value  $Q$  ( $\text{MJkg}^{-1}$ ).

Specimens selected in this way covered the whole vertical extent of the currently mineable Estonian oil shale deposit and the main product ranges of the Estonia underground mine enrichment plant.

In addition to the information about the specimens and layers, Table 3.1 gives also information about the moisture content of the samples (cf. 3.1.3).

Table 3.1. Calorific value and moisture content of the samples [P II].

No	Specimen		Calorific value (Dry base) $Q^d$ , $\text{MJkg}^{-1}$	Moisture content $W_w$ , wt%				
	Layer index	Thickness, cm		W1	W2	W3	W4	W5
1	A'/B	19	0.503	11.3	9.7	8.2	6.9	2.8
2	C/D	17	0.721	9.6	7.4	5.9	5.6	1
3	D/E	7	1.811	10.3	8.8	6.2	5.7	2.1
4	B/C	26	2.32	10	8.3	5.9	5.5	1.7
5	EST $Q=1.5$	2.7	3.055	10.1	8	5.6	5.2	2.7
6	F2	29	4.502	9.7	7.9	6.3	5.8	1.2
	D	5	6.813	10.5	8.5	5.7	5.3	2.7
8	EST $Q=7$	2.5	9.1	14.9	13.3	11.7	9.3	7.1
9	F1	34	9.493	10.6	8.6	6.3	6	4
10	EST $Q=8$	3	10.064	16	13.9	12.1	8.6	8.5
11	E	50	12.616	11	9.3	7.4	5.3	3.8
12	EST $Q=11.4$	2.5	12.758	9.2	7.7	5.5	4.5	0.8
13	A+A'	25	13.605	23.4	20.6	18.8	10.7	10
14	C	52	15.581	10.6	8.6	6.1	5.3	4
15	B	36	21.123	15.3	13.2	11.5	7.7	7.3

All of the samples were crushed by jaw crusher to a fraction of approximately 0–25 mm at the enrichment plant of the mine “Estonia”, and for further transportation the samples were placed in plastic bags.

Further, each of the specimens was divided into two parts, one of which was used for the determination of the calorific value by the calorific bomb method in PKK, and the other part was used for spectral measurements. Examples of crushed oil shale are presented in Figure 3.3. We can see that the size of the lumps varies within a wide range. The specimens with higher calorific value tended to have a larger portion of small lumps.

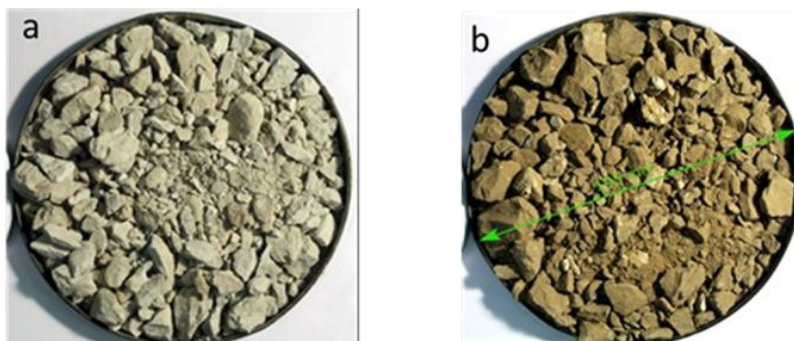


Figure 3.3. Specimens of crushed oil shale; a – a C/D specimen and b – a C specimen.

### 3.1.3 Variation of moisture content

The net calorificity is the most important parameter for optimization of industrial processes. However, as compared with the determination of the gross calorific value by the bomb method, measuring the actual moisture content is a more complicated procedure. Oil shale is characterized by a relatively high value of moisture content. Immediately after mining, the moisture content starts to change towards the equilibrium with the surrounding environment [153]. Evaporation of water depends on the composites of oil shale (limestone, kukersite), on the degree of crushing and on the temperature and humidity of the surrounding medium. Because of these reasons, at the arrival to the laboratory, the moisture content of specimens was undetermined.

To vary the moisture content of crushed specimens, the oven-drying method has been used [154]. In case of LIBS measurements, this procedure involved the following steps.

- A portion of ca 0.5 kg from each sample was used for testing.
- Samples were placed in hermetic jars, and distilled water in the amount of about 10% of the sample's weight was pipetted to each jar.
- The moisture homogenization was achieved by stirring and keeping the samples in hermetic jars for one week.
- Before LIBS measurements, mass  $m_w'$  of each sample was determined with the accuracy of 0.1g.
- After LIBS measurements, masses  $m_w''$  of samples were measured.
- Before the next cycle of measurements, samples were dried in open air for 24 hours.
- Then the jars were closed hermetically and kept in this state for one week to homogenize the moisture content at a lower level. For each sample, LIBS measurements were carried out at five different values of moisture.
- As a final step, samples were kept for 3–3.5 hours at atmospheric pressure in an oven at 105 °C temperature and masses of dry samples  $m_d$  were determined.

The moisture content of each sample was found as the difference  $\left(\frac{m_w' + m_w''}{2} - m_d\right)$ . It appeared that the difference  $(m_w' - m_w'')$  was less than 1 % from the total mass difference.

Table 3.1 documents all the samples used for LIBS testing: 15 x 5 samples with different calorific value  $Q^d$  (MJkg<sup>-1</sup>) and moisture content  $W_w$  (wt%).

Differently from LIBS measurements, the moisture content of the DRS samples was increased from low to high moisture level (up to 20%) by pipetting water, 4% of the sample weight, into the jar, followed by subsequent "homogenization" in closed jars. Table 1 in [P III] presents the data of the DRS samples.

The reliability of the described methods for determining the water content (wt%) depends on the homogeneity of the moisture distribution within oil shale lumps.

### 3.2 LIBS device

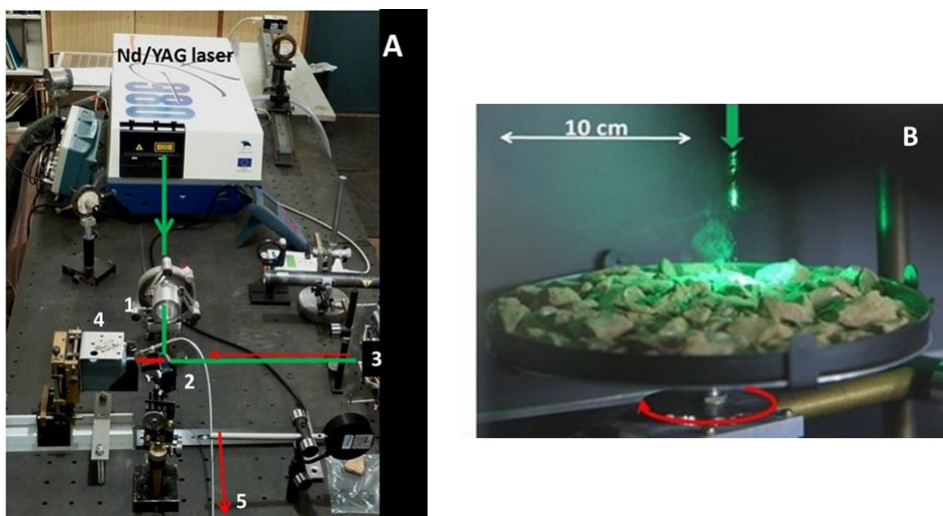


Figure 3.4. A – LIBS setup; B – a part of LIBS setup.

Two different setups were used. The preliminary measurements were made by using the setup 1 presented in Figure 3.4A. The frequency-doubled Nd:YAG (YG980 Quantel) laser pulse of 532 nm wavelength and of 9 ns full width half maximum (FWHM) was focused onto the sample surface with a plano-convex lens 1. On the way to the sample 3, the laser beam was reflected by a dichroic mirror 2 which had a high reflection coefficient near the 532 nm wavelength. Light emitted by the plasma plume at the sample surface passed the mirror 2 and was collected by a concave mirror 4 to the end of a fiber 5. The fiber delivered light to a spectrometer.

Most of the measurements were carried out with the setup 2, which was similar to the one presented in Figure 2.4, but in our case, the emitted light was collected by the help of a concave mirror. Samples were settled on the rotating stage. Figure 3.4B presents the moment when the laser beam passes through dust clouds produced by previous laser pulses and hits a lump of the crushed oil shale. The dust clouds scatter/absorb both the laser and emitted light, this disturbing effect was diminished by choosing a low repetition rate of laser pulse (one pulse per two seconds) and directing a stream of the air to the sample surface.

The laser pulse energy at the plane of the sample was measured with a pyroelectric laser energy meter “Ophir Nova II”. In experiments with pellets, the laser pulse energy was 75 mJ and the corresponding fluence at the pellet surface was  $\approx 27 \text{ Jcm}^{-2}$ . In experiments with crushed oil shale, the energy of the laser pulse was  $\approx 95 \text{ mJ}$ , but as the distance between the lens and the sample surface changed from shot to shot, together with the angle between the laser beam and the lumps’ facet, it was not feasible to speak about the average value of the fluence.

Figure 3.5 shows the laser energy changes in a sequence of 500 shots; the corresponding relative standard deviation was  $\text{RSD} = 0.03$ .

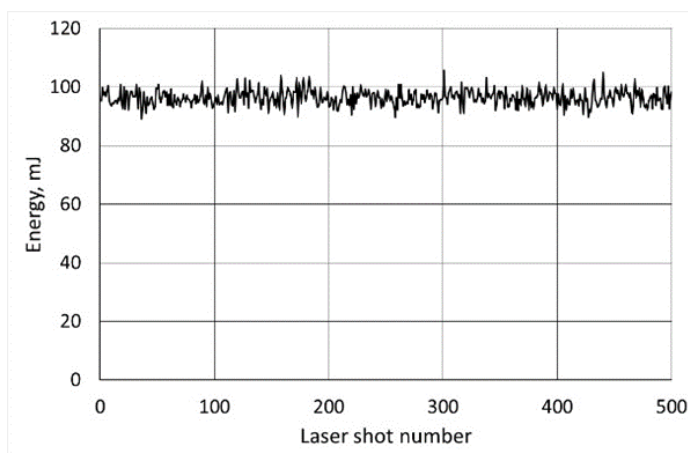


Figure 3.5. Laser energy versus shot number.

Spectra were recorded by a Mechelle 5000 spectrometer (Andor Technology), with a resolution of  $\lambda/\Delta\lambda = 5000$ . The spectrometer was equipped with an intensified charge coupled device Andor iStar. During a single laser shot, this device recorded the spectrum in the 220–850 nm range (single shot spectrum). It was possible to change the delay time  $t_d$  between the laser pulse and the opening of the gate for data acquisition as well as the temporal width  $\Delta t$  of the gate.

### 3.3 DRS device

A multipurpose analyser MPA-FT-NIR (Bruker Optik GmbH) was used. Fourier transform spectrometer recorded spectra in the range of 12500–3600  $\text{cm}^{-1}$  (800–2780 nm). Lumps of crushed oil shale filled a rotating Petri dish. The device functioned in diffuse reflectance mode (see 2.2.2) and it recorded directly the remittance. The relative remittance  $R'$  is determined as the ratio of intensity of the signal from the sample of the reference non-absorbing surface

The device had a number of options for data presentation; we opted for the absorbance as a function of the wavelength. Here, the term “absorbance” is just the apparent absorbance, introduced in analogy to the transmission spectroscopy, and is defined as  $A = \log(1/R')$ ; its value is directly related to the concentration of absorbing species.

### 3.4 Recording procedures and preprocessing of spectra

As it was pointed in 2.1.3, LIBS suffers from a poor shot-to-shot reproducibility. The role of fluctuations can be reduced by increasing the number of recordings. Our preliminary tests showed that starting from the 40th single-shot spectrum, the value of RSD does not change notably. Based on that observation, it deemed reasonable to assume that the average of 100 single-shot LIBS spectra can be considered as a “recording” which represents a sample with well-defined values of calorificity and moisture content. Information about the temporal changes at the sample’s surface, occurring during the measurements, was obtained by recording the sequence of five 100-shot spectra.

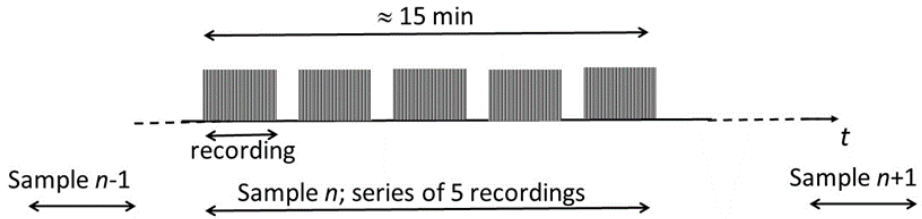


Figure 3.6. Cycle of measurements made with each sample.

Further the term “intensity” always denotes the integral intensity  $I$  of a spectral line. The intensity of spectral lines was found without subtracting the continuous component of the spectrum. As it was checked (see Figure 8, [P I]), such a subtraction changed the final results by a factor 1.3.

Internal normalization (see 2.1.3) is a way to decrease the role of fluctuations. For this purpose, we used for characterization of spectral regularities the reduced intensity  $I/I_T$ , where  $I_T$  is the total intensity.

Always when it is needed, the intensity and the reduced intensity are presented in their standardized form.

DRS device measured the average of 64 spectra (a “recording”). At a fixed moisture content each sample was characterized by at least three recordings.

## 4 Results and Discussion

### 4.1 LIBS results

74 spectral lines belonging to atoms and/or ions of Fe, C, Si, Mg, Al, Ca, Ti, Na, H, Li, N, K, O were selected to be used for the analysis of the samples. For all these lines, the main spectral characteristics, such as the energy level  $E_k$ , the statistical weight  $g_k$ , and the Einstein coefficient  $A_{ki}$  of  $k \rightarrow i$  transition, were available in the NIST database. Besides, these lines had an acceptable signal-to-noise ratio and the overlapping of these lines with neighboring lines was within acceptable limits. In most cases, it was possible to detect and use several spectral lines belonging to the same chemical element. However, in the case of carbon only 247.6 nm line was detectable and in the case of hydrogen, only  $H_\alpha$  line at 656.3 nm was detectable. The total intensity  $I_T$  was calculated over 220–850 nm wavelength range.

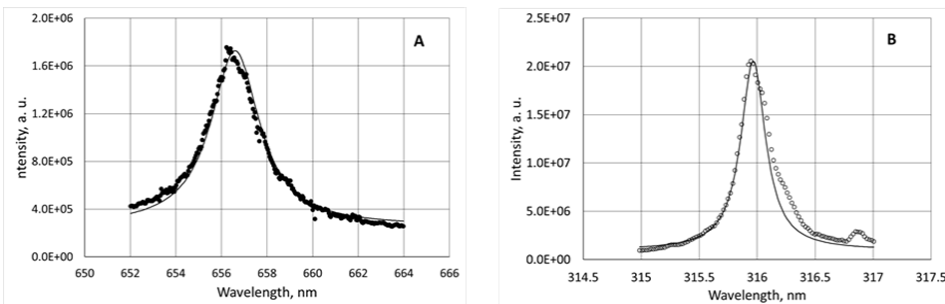


Figure 4.1. Spectral lines for the powder sample No 7. Graph A –  $H_\alpha$  line, halfwidth is 2.6 nm; Graph B – Ca II line, halfwidth is 0.26 nm. Experimental points are fitted by Lorentzian profiles.

In Figure 4.1, two spectral lines are shown, with intensities being averaged over 40 laser shots. Although the Ca II line on its right side is partly overlapped by another line, the Lorentzian fit was still the best one. Fitting with Lorentzian profile indicates that the main mechanism of the broadening of the spectral lines is the Stark effect.

The intensity of the spectral lines, of the background and of the width of the spectral lines have a strong dependence on the delay time.

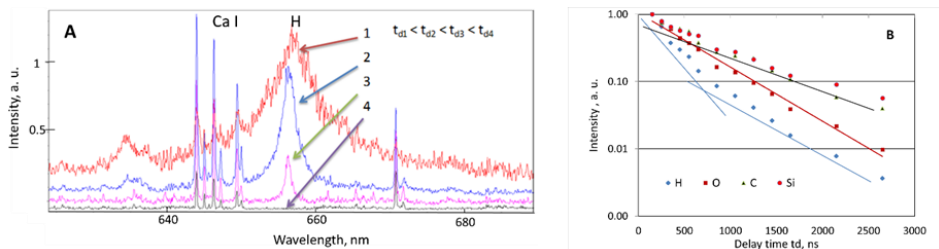


Figure 4.2. Spectral lines for the powder sample No 7. Graph A demonstrates that an increase of the delay time causes a considerable narrowing of the  $H_\alpha$  line ( $\lambda = 656\text{nm}$ ); lines to the left of the hydrogen line are Ca I lines;  $t_{d1} = 0.15\mu\text{s}$ ;  $t_{d4} = 4\mu\text{s}$ . Graph B shows the normalized intensities of the spectral lines of different elements vs the delay time  $t_d$  in semi-logarithmic scale.

In Figure 4.2A we can see that at the shortest delay time  $t_{d1} = 0.15 \mu\text{s}$ , the hydrogen line is very wide and the background intensity is high. Because of that the Ca I lines are hardly detectable. On the other hand, at the longest delay time  $t_{d4}$ , the calcium lines are easily detectable, but the hydrogen line has disappeared from the spectrum. Therefore, the optimal values for the delay time should be found. Figure 4.2B shows the dependence of the intensities of some elements on the delay time. We can see that for a majority of the lines, the intensity decreases with the delay time  $t_d$  exponentially, but the characteristic time constant is different for different elements. Thus, the ratio of intensities of spectral lines of two different elements does not remain constant.

Further we shall characterize the spectral lines by integral intensity. For a majority of the lines, the integral intensity equals to the sum of intensities of 6 pixels around the line's peak. As an exception,  $H_\alpha$  line was characterized by the sum of 61 pixels, and unresolved O triples at 777 and 844 nm were characterized by 21 pixels.

#### 4.1.1 Fluctuations

To study the reproducibility of the intensity of spectral lines, spectra from different spots at the surface of a single oil shale lump (Figure 4.3A) were recorded.

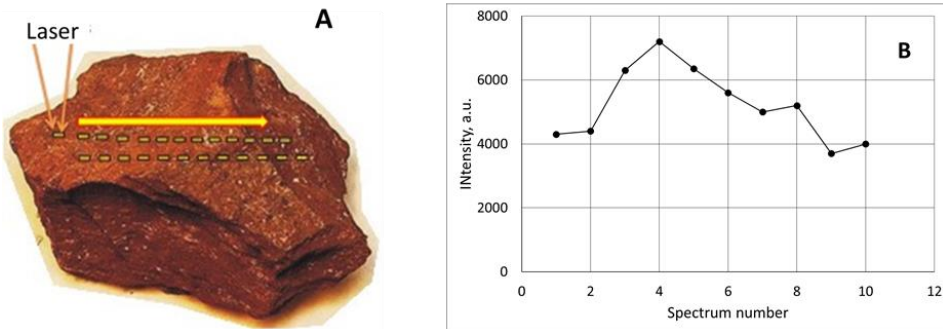


Figure 4.3. Image A shows the order in which the spectra were recorded along the surface of an oil shale lump. Graph B shows the intensity of the hydrogen line as a function of the spot number.

Figure 4.3B shows that the intensity of the hydrogen line has a strong dependence on the spectrum number. There are two main reasons for this variation:

- The absorption of the laser radiation changes from pulse to pulse because the surface morphology is different at different places on the lump surface.
- The oil shale chemical composition is different in different places.

The relationship between the intensity variations and the surface roughness is also supported by measurements with pellet samples made from powders of different level of grinding. (Figure 3.2).

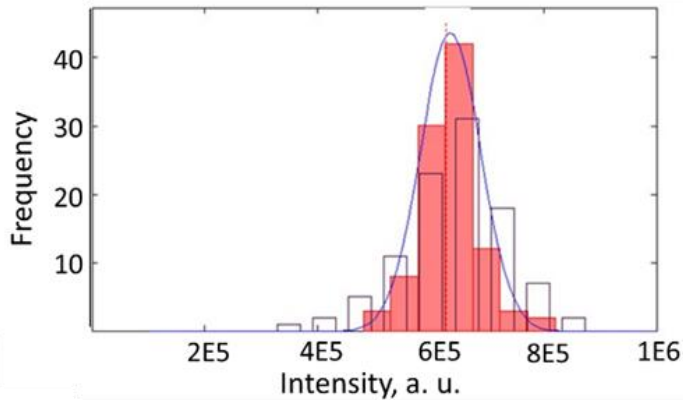


Figure 4.4. Histogram of the intensity distribution of  $H_{\alpha}$  line. Filled columns correspond to fine grinding; open columns – to raw grinding.

Histograms in Figure 4.4 show the intensity distributions of the hydrogen  $H_{\alpha}$  line in 100 spectra.

Both distributions are monodisperse and could be approximated by Gaussian curves. Fine-grinded samples have somewhat smaller value of the standard deviation but the mean value of distributions is almost the same.

Compared with pellet samples, the fluctuations of intensities of crushed samples were considerably larger. Figure 4.5 shows the changes of total intensities with the spectrum number. The apparent reason of larger fluctuations in case of crushed samples is related to the random orientation of facets of oil shale lumps. As a result, the angle of incidence of the laser beam varies randomly within  $0-90^{\circ}$  which leads to big changes of the “effective” value of fluence.

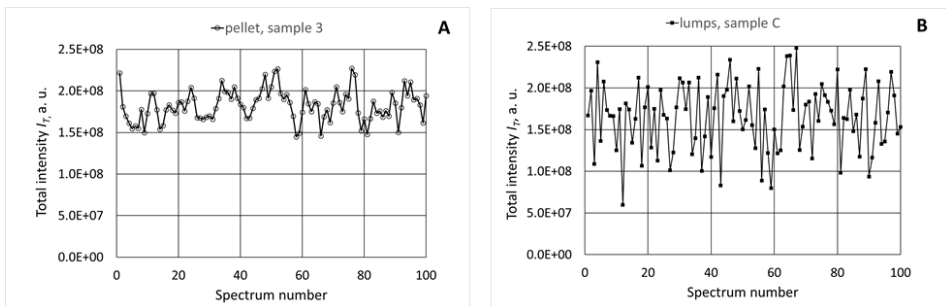


Figure 4.5. Total intensity as a function of the number of single shot spectra, air-dry samples. Graph A corresponds to pellet; graph B – to lumps.

As we can see in Figure 4.6, the histogram of the total intensity for the lumps is bimodal. The left hump at lower total intensity values of this distribution function corresponds to spectra belonging to larger angles of incidence of the laser beam. Meanwhile, the second and higher peak of the histogram for the crushed oil shale lumps is positioned almost at the same intensity value as the peak for the powder pellet sample.

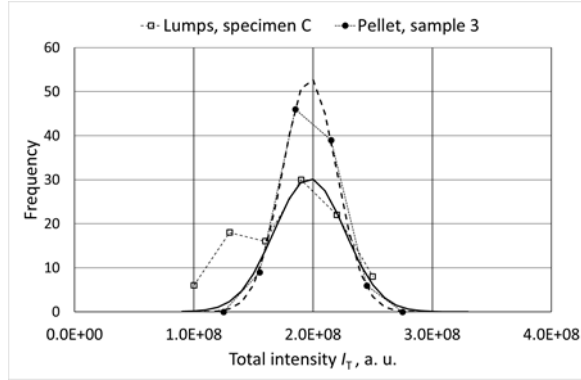


Figure 4.6. Histograms of total intensities; the solid line provides a Gaussian fit of the main peak in the case of the lumps.

It should be pointed out that the changes of the intensity of carbon line does not follow that of the total intensity. Figure 4.7 shows that the maximum, minimum and average values of the carbon line intensity do not match with the corresponding values of the total intensity. This result indicates that the concentration of the organic matter does not govern the total intensity of spectra.

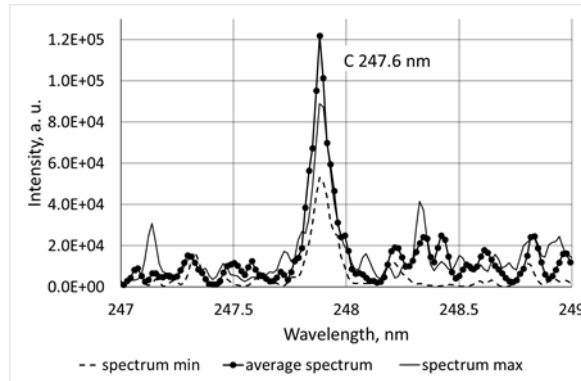


Figure 4.7. Sample C. Carbon line intensities corresponding to the maximum, minimum and average values of the total intensity. The gap between two pixels is 0.052 nm.

During a measurements cycle, the properties of samples do not remain unchanged. These temporal changes in spectra of powder samples were studied with rotating air-dry sample No 5. The sequence of 10 recordings temporally following each other was registered, each recording results to average of 40 laser shots. Intensities of spectral lines of different elements as well as the values of corresponding standard deviations differ remarkably. For better comparison of spectra of different elements, the intensities were standardized (see 2.1.4) according to the formula

$$IS_i^\lambda = \frac{I_i^\lambda - \overline{I^\lambda}}{SD}$$

where  $I_i^\lambda$  is the intensity of the spectrum number  $i$  at wavelength  $\lambda$ ,  $\overline{I^\lambda}$  is the average intensity and SD is the standard deviation.

Figure 4.8 depicts standardized intensities of spectral lines as a function of the recording number. In spite of comparatively big recording-to-recording fluctuations of the intensities, it is possible to separate two groups of lines with characteristic trends. The dominating trend in the case of most of the lines, Figure 4.8A, is the growth of intensity with the order number in the series of successive recordings. This trend can be explained by the roughening of the sample surface due to the action of laser pulses. Because of it, the laser radiation is absorbed more efficiently, which in turn increases the ablation rate and the intensity increases due to the increased amount of evaporated matter. Differently from other lines, intensities of N, O and H lines have initially a decreasing trend, and start increasing similarly to other lines only after passing a global minimum, see Figure 4.8B. The initial fall of intensities in the case of these lines can be explained by the fact that laser pulses reduce the number of air constituent molecules  $N_2$ ,  $O_2$ ,  $H_2O$  at the surface and in the pores of powder pellets.

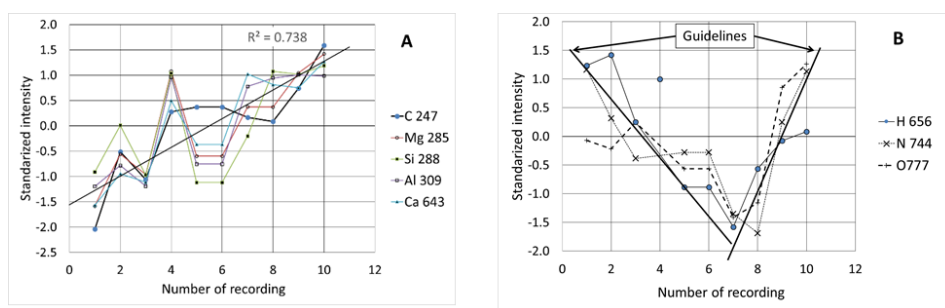


Figure 4.8. Intensity of different spectral lines as a function of the number of successive recordings in the case of air-dry powder samples.

#### 4.1.2 Crushed oil-shale samples with low moisture content

As it was reported earlier [133, 119], the moisture content has a considerable impact on LIBS results as due to the matrix effect, the intensities of spectral lines are affected by  $H_2O$  molecule which has a permanent dipole moment. Obviously the effect of moisture is particularly strong in the case of the hydrogen line. At the same time, hydrogen is an important element of the organic matter of oil shale (see Table 1.2). Thus, the presence of moisture complicates the understanding of the relationship between the LIBS spectra and the content of the organic matter in the oil shale. This is the main reason why it is reasonable to start with the samples with a low moisture content.

From the 75 samples of different calorific values and water content presented in Table 3.1, only samples of moisture content not exceeding 4% were chosen. The minimum value of moisture content of specimens A+A', B, Est 7 and Est 8 was higher than 4% and they were excluded from examination. From the remaining specimens, only the samples with lowest moisture content satisfied our condition. Thus, the spectra of 11 samples were analyzed.

There were some chemical elements which had many detectable spectral lines. As an example, the number of Ca I lines was 24. It appeared that intensities of these lines depended on the calorific value of samples almost identically, i.e. the data vectors in the 24-dimensional space where each axis corresponds to the intensity of one spectra line, were collinear. Figure 4.9 demonstrates the collinearity between the intensities of two spectral lines. For all pairs of Ca I lines, the slope of the trend-line of standardized

intensities was close to one but the factor  $R^2$  varied remarkably. For the further procedures, the line with the best signal-to-noise ratio was selected as the representative of Ca I atom. The similar choice was made for all atoms/ions, which had more than one detectable line.

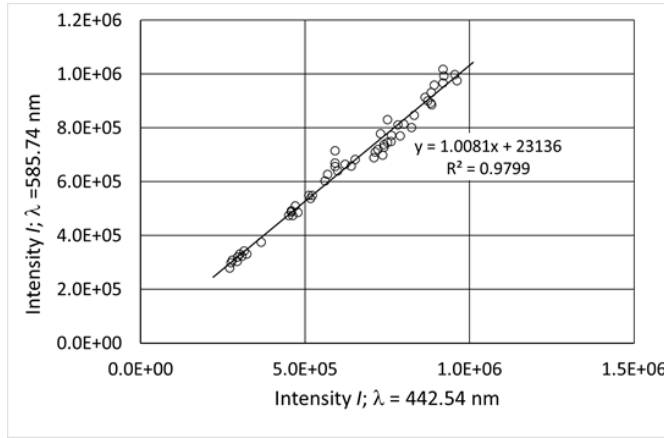


Figure 4.9. Relationship between intensities of two Ca I lines. Points belong to 55 recordings of 11 samples.

In Figure 4.10 we can see a gradual decrease of the total intensity  $I_T$  with the growth of the calorific value of the samples. This negative correlation serves as another evidence that magnitude of  $I_T$  grows with the content of inorganic matter in oil shale samples. Additionally, we can see from this graph that for a fixed sample, the shot-to-shot variations of the  $I_T$  values for the series of five recordings are fairly small, smaller the deviation of the data points from the linear trend-line.

As discussed in Section 3.4, using reduced intensities instead of directly recorded intensities helps to reduce the effect of fluctuations. This effect is demonstrated in Figure 4.11A where the reduced intensity  $I_C/I_T$  of the carbon line is plotted alongside with the intensity  $I_C$  against the calorific value of the sample. It appeared that for a fixed calorific value, there were no reliable trends in the temporal changes of the carbon line intensities for the sequence of five recordings. Because of that, for each calorificity, only the average of the five reduced intensity values is shown in the graph. We can see that the correlation between  $I_C/I_T$  and the calorific value  $Q^d$  is relatively big,  $R^2 = 0.848$ ; meanwhile, the coefficient of determination between  $I_C$  and  $Q^d$  is significantly smaller,  $R^2 = 0.212$  (the corresponding trend-line is not shown in the figure). Figure 4.11B presents the dependence of the standardized reduced intensity of the hydrogen line on the calorific value. Differently from what was observed for carbon line, for some calorific values, a small but clear temporal growth in the reduced intensity of the hydrogen line took place: the intensity increased slowly but persistently during the time interval of ca 15 minutes needed for taking all the five recordings. Such a behaviour can be explained by the fact that the moisture content of the samples was smaller than that of the ambient air. Hence, during the experiment, the samples' surface absorbed water vapors from the air.

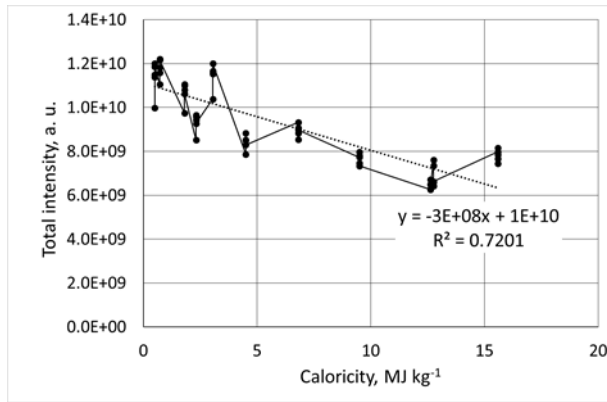


Figure 4.10. Total intensity as a function of the calorific value.

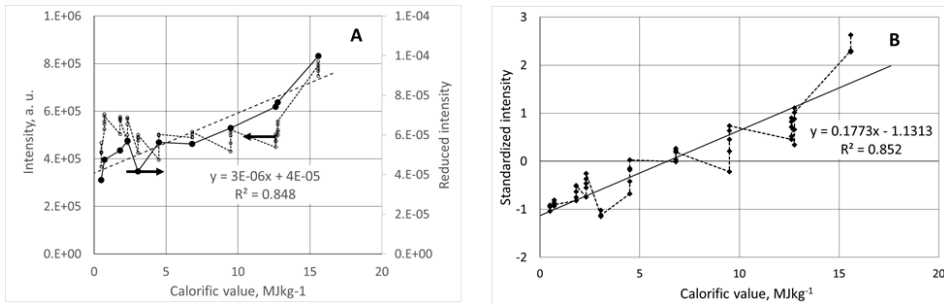


Figure 4.11. Graph A – intensity  $I_C$  and reduced intensity  $I_C/I_T$  of the carbon 427 nm line is plotted against the calorific value of the samples. Graph B – standardized reduced intensity  $I_H/I_T$  of hydrogen 656 nm line is plotted against the calorific value.

To find out the relationships between the reduced intensities of the spectral lines of different atoms /ions and correlations between these intensities and the calorific values of the samples, covariance of different pairs of variables was calculated. The covariance between variables  $x$  and  $y$  is defined as [155]

$$\text{cov}(x, y) = [\sum_{i=1}^N (x_i - \bar{x})(y_i - \bar{y})]/(N - 1),$$

where  $x_i, y_i$  are the results of the  $i$ -th measurement in a series of measurements, and  $\bar{x}, \bar{y}$  denote the average values of the corresponding quantities, averaged over the full series of measurements.

In calculations, both the reduced intensities  $I/I_T$  and calorific value  $Q$  had the standardized form. Note that when the standardized forms are used, the covariance varies from  $-1$  to  $1$ , and the squared covariance equals to the coefficient of determination  $R^2$ .

Table 4.1 presents the covariance matrix, where the matrix elements were found using the standardized intensities, averaged over the five recordings. According to the matrix, the calorificity has the highest positive correlation coefficient with the standardized intensity of the carbon and hydrogen lines. The covariance between Ca I and Ca II intensities with the calorificity as well as with all the other intensities of atoms/ions is negative. The strongest anticorrelation (with the highest absolute value of the covariance) is observed between the intensities of the Ca II and Si I spectral lines,

cf. Figure 4.12A. The origin of such an anticorrelation can be traced back if we look at the Figure 4.12B. First, notice that for a fixed sample, the deviation of the reduced intensity of the Ca II and Si I lines from the trend-line is much larger than the standard deviation of the intensities in the sequence of the five recordings (see the scattering in Figure 4.11A). The next thing to pay attention to is that the intensities deviate from the trend-lines in opposite directions: a higher Si I signal corresponds to a smaller Ca II signal and vice versa. This has a very natural explanation: samples with high-intensity Si I signal are composed dominantly from sandy clay, which leaves respectively less room for carbonates. Meanwhile, samples with an high-intensity Ca II signal are made predominatly from the carbonate compounds (see Table 1.2).

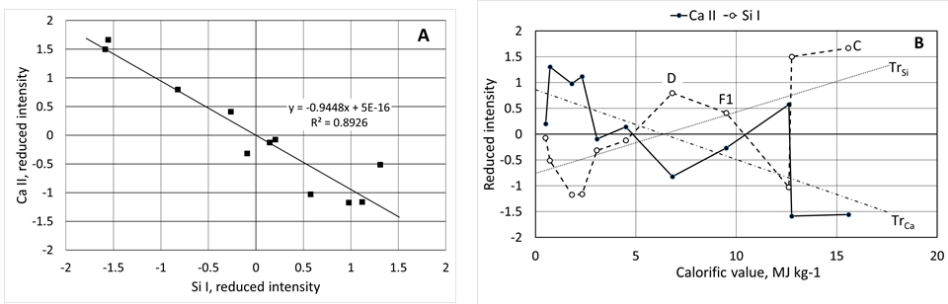


Figure 4.12. The scatter plot A demonstrates strong negative correlation between the intensities of the Ca II and Si I lines. Graph B – dependence of the intensities of the Ca II and Si I lines on the calorific value of the sample;  $Tr_{Si}$  and  $Tr_{Ca}$  are the corresponding trend-lines; labels near the data points denote the corresponding oil shale layers.

Table 4.1. Covariance matrix of samples with low moisture content.

	$\lambda$ , nm	247.856	656.279	720.219	315.887	288.158	251.611	250.69	309.284	500.721	336.121	670.776	323.622	238.204	744.229	777.194	588.995	769.896
	Q	1.00	0.94	-0.42	-0.73	0.64	0.34	0.52	0.70	0.81	0.63	0.54	0.79	0.82	0.78	0.78	0.78	0.79
	Cl	0.93	1.00	-0.30	-0.65	0.57	0.17	0.44	0.59	0.80	0.50	0.39	0.70	0.90	0.86	0.78	0.72	0.72
	HI	0.94	0.97	-0.45	-0.70	0.68	0.26	0.56	0.65	0.80	0.62	0.53	0.52	0.78	0.95	0.92	0.79	0.74
	Ca I	-0.42	-0.30	1.00	0.79	-0.90	-0.84	-0.98	-0.75	-0.17	-0.83	-0.32	-0.93	-0.86	-0.51	-0.54	-0.21	-0.42
	Ca II	-0.73	-0.65	0.79	1.00	-0.94	-0.85	-0.86	-0.96	-0.67	-0.93	-0.72	-0.96	-0.91	-0.62	-0.58	-0.59	-0.82
	Si I	0.64	0.57	-0.90	-0.94	1.00	0.83	0.94	0.94	0.54	0.97	0.64	0.99	0.94	0.64	0.64	0.55	0.75
	Mg I	0.34	0.17	-0.84	-0.85	0.83	1.00	0.85	0.83	0.25	0.83	0.55	0.96	0.73	0.19	0.19	0.22	0.55
	Mg II	0.52	0.44	0.56	-0.86	0.94	0.85	1.00	0.80	0.28	0.86	0.38	0.95	0.90	0.60	0.62	0.32	0.51
	Al I	0.70	0.59	-0.75	-0.96	0.94	0.83	0.80	1.00	0.68	0.96	0.84	0.96	0.89	0.52	0.49	0.68	0.89
	Ti I	0.81	0.80	-0.17	-0.67	0.54	0.25	0.28	0.68	1.00	0.62	0.78	0.50	0.53	0.63	0.54	0.87	0.89
	Ti II	0.61	0.50	-0.83	-0.93	0.97	0.83	0.86	0.96	0.62	1.00	0.73	1.02	0.86	0.55	0.53	0.59	0.81
	Li I	0.63	0.52	-0.32	-0.72	0.64	0.55	0.38	0.84	0.78	0.73	1.00	0.66	0.59	0.28	0.22	0.80	0.94
	Fe I	0.54	0.39	-0.93	-0.96	0.99	0.96	0.95	0.96	0.50	1.02	0.66	1.00	0.87	0.47	0.46	0.46	0.75
	Fe II	0.79	0.70	-0.86	-0.91	0.94	0.73	0.90	0.89	0.53	0.86	0.59	0.87	1.00	0.74	0.74	0.57	0.72
	N I	0.82	0.90	-0.51	-0.62	0.64	0.19	0.60	0.52	0.63	0.55	0.28	0.47	0.74	1.00	0.99	0.57	0.72
	O I	0.78	0.86	-0.54	-0.58	0.64	0.19	0.62	0.49	0.54	0.53	0.22	0.46	0.74	0.99	1.00	0.54	0.47
	Na I	0.78	0.78	-0.21	-0.59	0.55	0.22	0.32	0.68	0.87	0.59	0.80	0.46	0.57	0.60	0.54	1.00	0.90
	K I	0.79	0.72	-0.42	-0.82	0.75	0.55	0.51	0.89	0.89	0.81	0.94	0.75	0.72	0.54	0.47	0.90	1.00

### 4.1.3 Crushed oil-shale samples with different moisture contents

Now we discuss the data collected from of all the 15 specimens, each of which has 5 different values of moisture. As we can see from the Table 3.1, the method applied for varying the moisture content of crushed oil shale allowed us to vary the weight percentage of moisture  $W_w$  from 1 to 23.4%. However, there were considerable specimen-to-specimen variations: the same settings of the method resulted in different values of  $W_w$ ; importantly, the specific value of  $W_w$  which was achieved, was not related to the calorificity of specimens. As an example, for the specimen A+A' ( $Q^d = 13.6 \text{ MJ kg}^{-1}$ ), the moisture content varied from  $W_w = 10\%$  to  $W_w = 23\%$ , while for the specimen C with a fairly similar calorific value ( $Q^d = 15.58 \text{ MJ kg}^{-1}$ ) the moisture content was much smaller, from  $W_w = 4\%$  to  $10.6\%$ .

Total intensity  $I_T$  of the samples with a low moisture content had a clearly negative correlation with the calorific value  $Q^d$  (see Figure 4.10,  $R^2 = 0.72$ ). Meanwhile, this correlation disappeared when all the samples, with any values of  $W_w$ , were included into consideration: the coefficient of determination between  $I_T$  and  $Q^d$  dropped down to  $R^2 = 0.05$ . The moisture affected also the values of the elements of the covariance matrix, the results for the most important matrix elements are presented in the Table 4.2.

Table 4.2. Effect of moisture content on covariance value.

Element	Covariance of the reduced intensity with $Q^d$	
	Samples with $W_w < \text{wt } 4\%$	All samples
C I	0.93	0.92
H I	0.94	0.07
N I	0.82	0.13
O I	0.78	0.00

According to this table, reduced intensity of carbon has still a good correlation with the calorific value; this can be also observed in Figure 4.13A. However, the moisture reduces drastically the correlation between the reduced intensity of hydrogen and the calorificity. Figure 4.13B shows that the fluctuations of the values of  $I_H/I_T$  caused by the moisture are significantly larger for specimen with low calorific values. In order to explore this effect in more details, we have calculated the standard deviation SD characterizing these moisture-caused fluctuations of the reduced intensity: it appeared that the SD value decreases almost exponentially with the calorific value. Similarly, to the case of hydrogen, when all the samples with all the moisture content values are considered, the correlation between the calorific value and the reduced intensity of the nitrogen and oxygen lines disappears, too. Covariance between  $Q^d$  and other spectral lines was also dependent on the moisture content, but the changes were less dramatic, and remained below 50%.

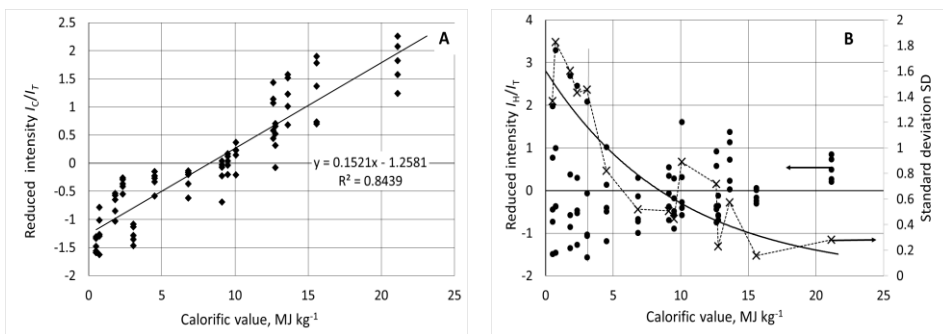


Figure 4.13. Reduced intensities of carbon (A) and hydrogen (B) lines is plotted as a function of calorific value recorded at five different values of moisture content. Each point presents the average of five recordings. Solid lines present linear (A) and exponential (B) fits.

In Figure 4.14 the total intensity  $I_T$  is plotted against the moisture content. It can be seen that for the given range of moisture content values, the intensity decreases with the increasing moisture content by an order of magnitude. Such a behavior where by a fixed laser pulse energy, of the total intensity  $I_T$  is decreasing with an increasing moisture content, is consistent with the results of the study [133] where the moisture in coal pellets caused a drop in the intensity of all the spectral lines. A likely reason of this effect is an extra loss of laser pulse energy for dissociation of the water vapor, which results in a lower concentration of matter in the plasma plume.

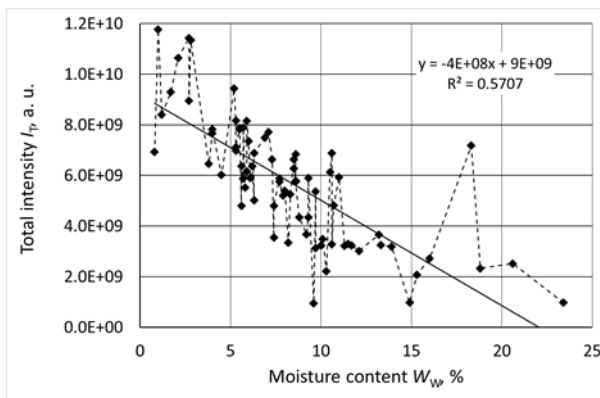


Figure 4.14. Total intensity as a function of the moisture content. Each point presents the average of five recordings.

It appears that at higher values of  $W_w$ , the temporal changes in the intensity ratio  $I_H/I_T$  taking place during a cycle of five recordings, depended on which specimen is used. Figure 4.15A shows that in the case of specimens with a high calorific value,  $I_H/I_T$  remained practically unchanged during the cycle, while in the case of specimens with a low calorific value, the intensity  $I_H/I_T$  gradually decreased with the order number of the recording within the series. Differences in the temporal behavior of  $I_H/I_T$  can be explained when we keep in mind that the hydrogen signal is related both to the content of the moisture, and to the content of the organic matter. Assuming that during a series of five successive recordings, the moisture content decreases at the sample surface, the intensity of the hydrogen signal should fall. This effect is more pronounced in the case of specimens

with a low calorific value, while for specimens with a high content of organic matter, this decay in the intensity remains unnoticeable. The average of the five recordings of  $I_H/I_T$  (cf. Figure 4.15B) shows a linear growth with the moisture content. It should be pointed that the outliers from this dependence belong to the specimens with low calorific value.

Table 4.3 shows the covariance matrix for such chemical elements for which the covariance with the moisture content  $W_w$  is relatively large. As we can see, all alkali metals belong to this table.

Additionally, this matrix shows that hydrogen, oxygen and nitrogen signals are highly correlated with each other. Keeping in mind that the correlation of the intensity of the spectral lines of these elements with the calorific value was almost missing (cf. Table 4.2), the last finding can be related to the presence of the air molecules at the surface and/or pores of samples.

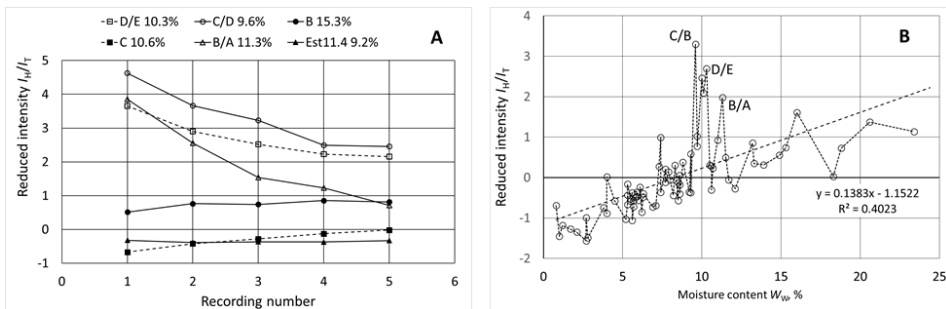


Figure 4.15. Graph A – temporal changes of the hydrogen signal occurring during one cycle of measurements recorded at relatively high values of  $W_w$ . Graph B –  $I_H/I_T$  is plotted as a function of  $W_w$ ; here each point presents the average of five recordings.

Table 4.3. Covariance matrix when all the samples with different values of moisture content are included into consideration.

	W	H I	Si I	Mg II	Al I	Ti I	Ti II	Li I	N I	O I	Na I	K I
W	1.00	0.64	0.55	0.50	0.55	0.56	0.59	0.68	0.44	0.50	0.63	0.75
H I	0.64	1.00	0.04	0.30	-0.01	0.22	0.22	0.40	0.90	0.95	0.38	0.37
Si I	0.55	0.04	1.00	0.75	0.97	0.52	0.88	0.53	-0.06	-0.06	0.41	0.66
Mg II	0.50	0.30	0.75	1.00	0.64	0.07	0.62	0.13	0.37	0.29	0.06	0.27
Al I	0.55	-0.01	0.97	0.64	1.00	0.63	0.88	0.61	-0.15	-0.15	0.52	0.73
Ti I	0.56	0.22	0.52	0.07	0.63	1.00	0.67	0.92	-0.02	0.04	0.88	0.93
Ti II	0.59	0.22	0.88	0.62	0.88	0.67	1.00	0.72	0.03	0.07	0.55	0.77
Li I	0.68	0.40	0.53	0.13	0.61	0.92	0.72	1.00	0.10	0.22	0.87	0.95
N I	0.44	0.90	-0.06	0.37	-0.15	-0.02	0.03	0.10	1.00	0.96	0.09	0.11
O I	0.50	0.95	-0.06	0.29	-0.15	0.04	0.07	0.22	0.96	1.00	0.19	0.19
Na I	0.63	0.38	0.41	0.06	0.52	0.88	0.55	0.87	0.09	0.19	1.00	0.87
K I	0.75	0.37	0.66	0.27	0.73	0.93	0.77	0.95	0.11	0.19	0.87	1.00

#### 4.1.4 Application of multivariate regression model for data processing.

In subsection 4.1.2 we saw that in case of samples with a low moisture content the univariate regression gave more-or less satisfactory correlation between the calorificity and the intensity of the carbon line as well as between the calorificity and the intensity of hydrogen line. Results of the subsection 4.1.3 showed us that in a more general case when the moisture of the samples varied within a wider range, values of covariance between the calorificity and some spectral lines (including hydrogen) changed drastically, cf. Table 4.2. Besides, we saw that at a fixed calorific value, a variation of the moisture content can cause big changes in the carbon line intensity. Thus, to be able to predict the

calorific value and the moisture content with a higher accuracy, a more sophisticated model of the multivariate linear regression must be used. The calculations were done using self-written Mathcad program. Here we provide only the basic principles of this regression model, together with the main results obtained by using it; for more details cf. our publications [P I, P II].

In order to apply the ordinary multivariate regression method, we use the reduced integral intensities of spectral lines as a set of observable variables.

According to the model of multiple linear regression (see 2.1.4), a dependent variable had to be introduced as a linear combination of independent variables. If the calorificity is taken as the dependent variable and the independent variables are the reduced intensities of spectral lines, then the corresponding relationship in a vector form could be written as

$$Q = K \cdot I.$$

Here,  $Q$  is the calorific value of a sample;  $I$  is an  $N$ -dimensional vector of intensities of selected spectral lines, and the components of  $K$  are the coefficients which need to be found during the calibration.

The components of the vector  $K$  were found as the linear regression coefficients of a least-square fit [156], calculated as

$$K = (A^T \cdot A)^{-1} \cdot A^T \cdot B,$$

where  $A$  denotes a  $M \times N$  matrix the elements of which are the reduced intensities  $I_{m,n}$ , measured for the calibration purposes,  $M$  denotes the number of different samples for which the spectra were measured, and  $B$  is a vector the  $M$  components of which are the known values of the calorificity. Superscript  $T$  denotes the transposed matrix.

Covariance matrices in subsections 4.1.2 and 4.1.3 gave the preliminary information about the correlation between the intensities of spectral lines and the calorificity  $Q^d$  (and with the moisture content  $W_w$ ). However, we want to work out a method to predict the relevant parameters of a sample from the LIBS spectra, and so we need to answer two more questions. First, what is the optimal number of different spectral lines which need to be used by the multivariate method, to achieve the best possible predictions. It appears that increasing the number of spectral lines does not necessarily improve the predictions. Second, can we test if our method of deducing the parameters of a sample from the measured spectra is sufficiently precise and reliable.

To answer these questions, we used the leave-one-out cross-validation method [157]. This method works as follows. We start with estimating the calorificity  $Q_i^d$  of the  $i$ -th test specimen with 5 different values of  $W_w$  (altogether  $5 \times 5 = 25$  recordings, see section 3.4), from the spectral measurements. To that end, the following steps were made. First, we found the calibration vector  $K$  by using the data of 14 remaining specimens, each of them represented with five different samples of different values of  $W_w$  (hence, altogether  $14 \times 5 \times 5 = 350$  recordings were used). Second, the obtained vector  $K$  was used to build a calibration curve, and the value of  $Q_i^d$  was found using the formula  $Q = K \cdot I$ .

This leave-one-out procedure was applied to all the 15 specimens. The standard deviation error of prediction (SDEP) was used as the criterion for the quality of the prediction

$$SDEP = \sqrt{\frac{1}{M} \sum_{i=1}^M (Q_i^d - Q_i^p)^2}.$$

Here  $Q_i^d$  denotes the calorific value of the  $i$ -th test sample measured with a bomb calorimeter and  $Q_i^p$  is the predicted calorific value of the sample.  $M$  stands for the total number of measurements ( $M = 375$ ).

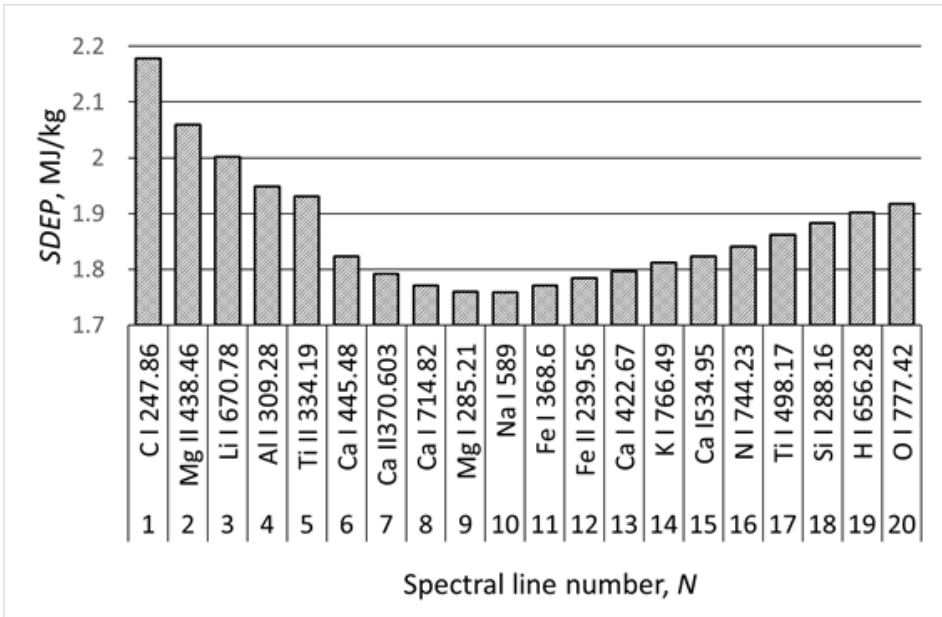


Figure 4.16. The graph shows the dependence of SDEP on the number of the spectral lines added incrementally to the set of variables [P II].

The regression model was applied to different sets of spectral lines but always the calculation of SDEP was started with the carbon line as it has the highest correlation with  $Q^d$ . The intensities of new spectral lines were progressively added to this multivariate regression model: among all the options, the one which gave the smallest value of SDEP was selected. Figure 4.16 shows how the resulting SDEP changed as a function of the number of the used spectral lines when this procedure was followed. We can see that when the spectral lines are incrementally added, SDEP decreases at first until reaches its minimum value at  $N = 10$ , and then starts to grow.

Data points in Figure 4.17 are calculated using the first 10 spectral lines in Figure 4.16. Both a linear and a polynomial fit were used to approximate the dependence between the LIBS results and the calorific value  $Q^d$  of the sample. The root-mean-square (denoted as SD) of the difference between the true calorific value and the LIBS prediction,  $Q^p - Q^d$ , was calculated. While the linear fit gave resulted in  $SD^{LIN} = 1.76 \text{ MJkg}^{-1}$ , the polynomial fit gave considerably better results with  $SD^{POL} = 0.8 \text{ MJkg}^{-1}$ .

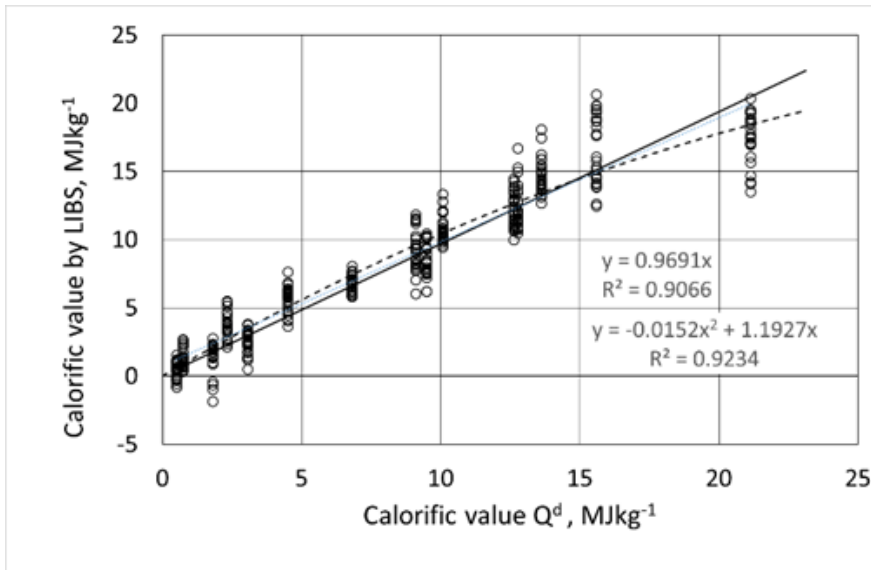


Figure 4.17. Calorific value determined from the LIBS measurements,  $Q^p$ , is plotted against the directly measured calorific value  $Q^d$ . Data points show the results of testing; solid line shows the linear fit and dashed line – the polynomial fit.

This multivariate regression method was also used for determining of the moisture content  $W_w$ , in a full analogy with how it was used for determining the calorific value. Now, the spectra were ranked by moisture content and not by calorific value. All the spectra were divided into five groups (see Table 3.1) with different moisture contents. Each group had  $15 \times 5$  recordings. Four groups out of these five were used for calibration and one was left for validation. This procedure was performed for all the five possible ways of selecting the validation group. According to Table 4.3, potassium line has the best correlation with  $W_w$  and so the SDEP calculations started from this line. It appeared that again, the SDEP value reached its minimum at  $N = 10$  lines. The root-mean-square of the difference ( $W_w - W_w^p$ ) was 1.94%. Keeping in mind that the average value of the moisture content is  $W_w \approx 10\%$ , we can see that the accuracy of the assessment of  $W_w$  is remarkably lower than that of  $Q^d$ . The reason of the relatively high uncertainty of the prediction of  $W_w$  is probably related to the temporal changes of spectral line intensities (see Figure 4.15) which, in turn, is caused by the fact that the surface of the samples dries during a series of five recordings.

Differently from the crushed oil shale samples, in the case of powder pellets, the information about the chemical composition was available to us ([P I], Table 1). This circumstance made it possible to apply LIBS for estimating the concentrations of different compounds by applying the same multivariate least square method which was used above for finding the calorificity and moisture content. Although the sulfur lines were out of the sensitivity range of our LIBS spectrometer, its presence ( $\text{wt}\% \leq 1.5$ ) influenced the intensities of other lines and this circumstance allowed us to find the sulfur concentration with the relative standard deviation  $\text{RSD} = 4\%$ .

## 4.2 DRS Results

In order to be able to compare the results obtained with DRS directly with those obtained by LIBS, the same set of specimens of the crushed oil shale was used. However, as described in Section 3.1.3, by DRS, a different method of the moisture content variation was used; this allowed us to reduce significantly the range over which the value of  $W_w$  changes within each moisture group, as one can see by comparing Table 3.1 with Table 1 in [P III].

The multipurpose analyser MPA-FT-NIR has different data presentation options; in the present study, we used the absorbance  $A = \log(1/R')$  as a function of the wavelength. At the  $8 \text{ cm}^{-1}$  spectral resolution, the average of 64 single spectra (“a recording”) was saved. At a fixed moisture content, each sample was characterized by at least three recordings.

For the analysis of spectra, the spectral range 1300–2600 nm was selected, as at shorter wavelengths, the absorption bands were missing, and at longer wavelengths, the absorption was too large.

In order to improve the visibility of the absorption bands, the first derivative of the absorbance was used for the characterization of the spectra. In Figure 4.18A, we can see five easily identifiable absorption bands [158–160].

Further the values of  $dA/d\lambda$  were used as the characteristics of bands intensities. Figure 4.18B shows that at a fixed moisture content, the absorbance grows with the calorificity at a decelerating rate; this suggests that the absorbance will saturate at high calorific values. The same type of behavior was observed in the case of all the used moisture values.

In the case of a certain specimen, the absorbance was a linear function of the moisture content but the slopes of these dependences differ remarkably (see Figure 4b in [P III]).

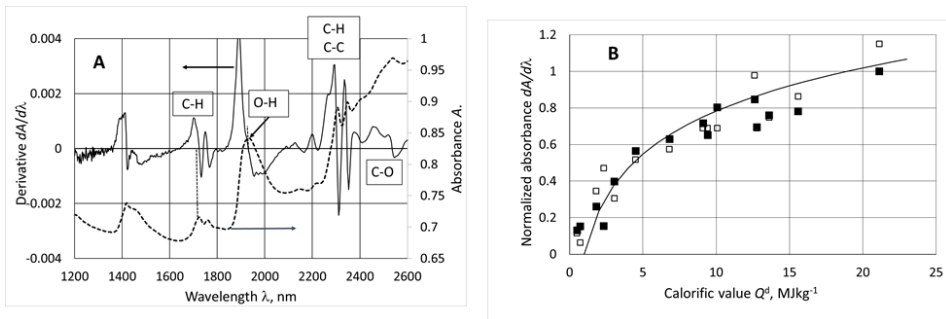


Figure 4.18. In graph A, absorbance  $A$  and its derivative  $dA/d\lambda$  are plotted against the wavelength for the specimen F1 with  $W_w = 7.5\%$ . In graph B,  $dA/d\lambda$  is plotted as a function of the calorificity for  $W_w = 14.5\%$ ; filled symbols correspond to the peak values at  $\lambda = 2305 \text{ nm}$ ; open symbols – to the peak values at  $\lambda = 1725 \text{ nm}$ ; solid line shows a logarithmic fit for the data at  $\lambda = 2305 \text{ nm}$ .

In this section, we have seen at a qualitative level that the vibrational spectra depend on the calorificity  $Q^d$  and moisture content  $W_w$ . To obtain quantitative information, we have used the built-in functionality of the software of the multipurpose analyzer – it can apply a multivariate analysis. Differently from LIBS, it is assumed that the sample composition influences the whole spectrum. For data analysis, the device’s software applies partial least square (PLS) linear regression method (see 2.1.4). The general approach is the same as in the case of LIBS. First, on the basis of spectra belonging to

samples with different calorific values and with different moisture content, the calibration curve is calculated; this curve is later used for the analysis of the unknown samples.

Using the minimum of the standard deviation error of prediction (SDEP) as the criterion (see 4.1.4), the device's software chose combinations of preprocessing methods and selected spectral ranges. The software used two types of validation. The first one was the leave one out method. The second validation type uses two independent sets of samples, one for the calibration (in the present study – 20% of the spectra were put into that set) and the other (in the present study – the remaining 80% of the spectra) for validating the model. The both types of validations yielded very similar prediction-characterizing dependences.

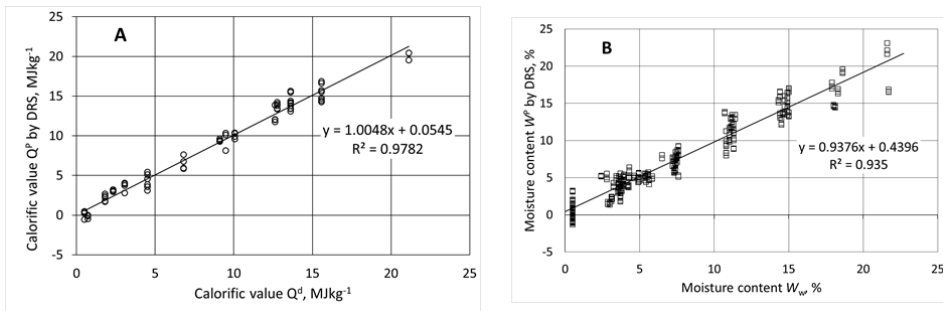


Figure 4.19. Graph A shows the predictions of calorificity based on the multivariate analysis of the DRS absorption spectra of the samples. Graph B shows the predictions of the moisture content. Both graphs present the results of the one-leave out method.

Dependences in Figure 4.19 show a good correlation between the calorific value and moisture content determined by DRS and traditional laboratory methods.

### 4.3 Conclusions

In the modern era, a profitable industrial production has to take into account the limitations set by environmental protection requirements. One way of mitigating the contradictory requirements of profitability and of environmental protection is to develop such methods which consider and make use of the properties of the source materials in as much details as possible.

The existing industrial methods of the oil shale quality control are sufficiently precise, but too time-consuming and hence, unsuitable for real-time monitoring of the properties of the samples on the conveyer belt. At the same time, the actual oil-shale samples on the conveyer belt fluctuate in composition and properties considerably over a fairly short time scale. This can result in a big mismatch between the daily average data of the calorific value (from the precise but slow measurements), and the actual calorific value of many pieces of the excavated oil shale. Indeed, as we can see from Table 3.1, the difference between the daily average calorific values and the calorific value of a specific specimen taken from a stopped conveyer belt on that day (the samples labeled with “EST”) may be really big. In the extreme case of the sample “EST Q = 1.5”, the daily average calorific value 1.5 MJkg<sup>-1</sup> differs more than two-fold from the sample's actual calorificity of 3.05 MJkg<sup>-1</sup>. For other “EST”-labeled specimens, the difference was less dramatic, but typically still around 20%. These results demonstrate unambiguously that

in order to increase the efficiency of streamlined technologies of the oil shale treatment, a continuous real-time control of the quality of raw materials is needed. For similar purposes, user-friendly non-invasive optical techniques have been applied in different contexts, as discussed in sections 2.1.5, 2.2.3.

In section 1.7, we have formulated main requirements for techniques used for real-time oil shale testing. These considerations serve us here as a guideline for summarizing the main findings obtained by LIBS-testing of samples under conditions close to the ones on a running conveyer belt. The main aim of this thesis is developing a method for predicting the gross calorific value and the moisture content using LIBS data. More specifically, we are dealing with the findings based on the comparison of the LIBS results for crushed oil shale samples [P I] with the LIBS results for the powder pellets [P II], and with the respective results obtained while using the DRS technique [P III].

During a single laser shot, numerous spectral lines belonging to 12 chemical elements in the wavelength range from 220 to 850 nm were recorded. In addition to the intensities of individual spectral lines, the total intensity  $I_T = \int_{220}^{850} I(\lambda) d\lambda$  was calculated. As the samples contain lumps of organic and inorganic matter with variable properties and the facets of lumps had random orientation with respect to the direction of the laser beam, intensities in single spectra varied significantly. We managed to reduce the amplitude in which the spectral line intensities fluctuate, quantitatively characterized by the standard deviation, by introducing and making use of the reduced intensity  $I/I_T$ , where  $I_T$  is the total intensity. In order to obtain statistically significant information about the samples, a large number of spectra were recorded (see section 3.4). Overall, 75 samples were tested, with each sample having its own fixed value of calorificity and moisture content.

The first step of the spectral data preprocessing was calculating the covariance matrices, with the matrix elements being the covariances between the calorific values or moisture contents on the one hand, and intensities of the different spectral lines, on the other hand, as well as covariances between different pairs of spectral lines (see Tables 4.1 and 4.3). In a full agreement with theoretical expectations, the intensity of carbon line turned out to be strongly correlated with the calorific value; this behavior is robust and is almost independent on the moisture content. At the same time, the moisture content did affect strongly the covariances between the calorificity and the intensity of the hydrogen line: while for low values of the moisture content, the correlation was strong, for higher moisture values, the correlation between the calorificity and the intensity of the hydrogen line was almost completely lost (see Table 4.2).

The dependence of the carbon line intensity on the calorific value can be used as a rough way to estimate the calorificity. However, in order to achieve a better prediction, we have applied a multivariate analysis by using the model of multiple linear regression. With this model, linear regressions of the calorific value and of the moisture content with different combinations of spectral lines were calculated, and the leave-one-out cross-validation method was applied; the standard deviation error of prediction (SDEP) served us as the criterion of the evaluating the quality of the fit. It appeared that a set of around 10 spectral lines was needed to reach the minimum of the standard deviation.

Table 4.4. Quality of the calorific value and moisture content predictions.

Method	Type of samples	Analyzed Quantity	Range	Trend-line slope	$R^2$	SDEP	Ref.
LIBS	Powder pellets, air-dry	$Q^d$	6.4-11.6 MJ kg <sup>-1</sup>	1*	0.98	0.24 MJ kg <sup>-1</sup>	[P I]
	Lumps & variable moisture	$Q^d$	0.5-21.1 MJ kg <sup>-1</sup>	0.91*	0.91	1.76 MJ kg <sup>-1</sup>	[P II]
		$W_w$	1-23.4 %	0.83*	0.82	1.94 %	
DRS	Lumps & variable moisture	$Q^d$	0.5-21.1 MJ kg <sup>-1</sup>	1* 1**	0.98 0.97	0.85 MJ kg <sup>-1</sup> 0.84 MJ kg <sup>-1</sup>	[P III]
		$W_w$	0.5-22.3 %	0.94* 0.97**	0.93 0.94	1.35 % 1.33 %	

\*leave-one-out validation

\*\*test set validation

Table 4.4 summarizes results obtained for different sets of samples and different optical methods. In this table columns “Trendline slope”, “ $R^2$ ”, and “SDEP” characterize the quality of the predictions of the calorific value and moisture content based on the optical methods by comparing the respective predictions with the more accurate measurement results obtained by calorific bomb and weighing. As we can see, the accuracy of the prediction of the calorificity was the highest in the case of air-dry powder samples. In that case, the achieved SDEP values approached the uncertainty of determination of our reference values obtained with the calorimetric bomb (0.13 MJ kg<sup>-1</sup> [P I]). Although this method is accurate, it is also slow, time needed for preparing the powder pellets is comparable with the one needed for calorific bomb measurements. Much more importantly, our powder pellet study demonstrated that multivariate regression analysis of LIBS spectra can be used to determine the dominating constituents of oil shale with high accuracy, with the relative standard deviation being less than 5%.

When crushed oil shale samples were used instead of powder pellets, both LIBS and DRS measurements of the calorific value  $Q^d$  were less accurate. While there are several potential explanations for such a behavior, effects related to the moisture content seem to be the main reason for the increased prediction error of  $Q^d$ . This conclusion is based on the fact that when only air-dry crushed oil shale samples are used, predicting the value of  $Q^d$  with LIBS becomes much more accurate, with  $R^2 = 0.96$  and the standard deviation taking values around 1.1 MJ kg<sup>-1</sup> (cf. [P II]). It was shown in section 4.1.3 that the moisture affects the intensities of many spectral lines which are used in  $Q^d$  calculation. Similar effect happens in the case of DRS spectra where the moisture causes changes not only in the OH bands, but also in other parts of the spectra (cf. [P III]). Both LIBS and DRS techniques use information obtained from the surface layers of samples; thus far, it has been assumed that the conditions at the surface are the same as inside the samples. However, in the present experiments, this assumption is likely to fail, because at the surface, so fast changes are taking place, (cf. Fig 4.15A) that the moisture content inside lumps is unable to adapt.

Mismatch between the conditions at the surface and inside the samples can be expected to be the reason for the difference between the moisture content values determined by weighing and by the optical methods.

As one can see from Table 4.4, the DRS technique predicted calorific value at least two times more accurately than the LIBS technique. The likely cause of this that by integrating it over a sphere, the DRS spectrometer is collecting and averaging the light more efficiently.

Regarding the prospects of developing the LIBS device further as a part of the real conveyer belt, it should be pointed out that in the present LIBS studies, the fast changes at the surface of the oil shale lumps on the rotating stage were caused by a continuous airflow. The drying effect caused by airflow will be less pronounced in the case of a real running conveyer belt.

Also, the sets of crushed oil shale specimens used by the current study belong to layers with very different concentrations of components; this gave rise to big fluctuations in how the intensity depends on the calorificity (cf. Fig 4.12B), resulting in larger values of SDEP. At the same time, the modern selective mining (cf. 1.3) is producing more homogeneous composition of the raw material. This circumstance is expected to improve the prediction of the oil shale parameters.

Finally, recall that our study was based on linear regression models for data processing. However, we saw that a polynomial fit gave noticeably better results, see Fig 4.17. Thus, a software upgrade is a feasible way of increasing the prediction accuracy.

This feasibility study showed that the laser induced breakdown spectroscopy (LIBS) is the technique which can be used for real-time control of the oil shale properties. Apart from the fact that it can be used for determining such integral quantities as the calorificity and the moisture, LIBS makes it possible to determine the elemental composition of the raw material. This additional ability of LIBS is important when oil shale is being used as a raw material in fine chemistry. When corresponding calibration data are used, the LIBS-based measurement results can be also used for designing the processing methods of the oil shale by-products.

## References

- [1] Bauert, H. (2015). Shelly phosphate rocks of Estonia. In: Bauert, H., Soesoo, A., & Hade, S. (eds.) *Proceedings of the Strategic Raw Materials of Estonia*. Rakvere, Estonia; 16–17 October 2015; pp. 24-32. Available: <https://www.researchgate.net/publication/283255735> [Accessed 20th October 2021].
- [2] Berger, M. (ed.) *Estonian oil shale industry yearbook 2018*. Eesti Energia (EE), Viru Keemia Grupp (VKG), Kiviõli Keemiatööstus (KKT), and the Oil Shale Competence Centre at the TalTech Virumaa College (OSCC); 2018. Available: <https://www.vkg.ee/cms-data/upload/uudised/polevkivi-aastaraamat-2019-eng-veeb.pdf> [Accessed 20th October 2021].
- [3] Rivas, S., Urraca, R., Bertoldi, P., & Thiel, C. (2021). Towards the EU Green Deal: Local key factors to achieve ambitious 2030 climate targets. *Journal of Cleaner Production*, 320, 128878.
- [4] Riispapp, J. (2021). Eesti elektritoodang kukkus paari aastaga poole võrra. *Postimees*, January 17, 2021. Available: <https://majandus.postimees.ee/7157778/eesti-elektritoodang-kukkus-paari-aastaga-poole-vorra> [Accessed 20th October 2021].
- [5] Wikipedia contributors. (2021, October 8). Pumped-storage hydroelectricity. In Wikipedia, The Free Encyclopedia. Available: [https://en.wikipedia.org/w/index.php?title=Pumped%20storage\\_hydroelectricity&oldid=1048926693](https://en.wikipedia.org/w/index.php?title=Pumped%20storage_hydroelectricity&oldid=1048926693) [Accessed 21st October 2021].
- [6] International Energy Agency. (2019, June). The Future of Hydrogen. IEA - International Energy Agency. Available: <https://www.iea.org/reports/the-future-of-hydrogen> [Accessed 20th October 2021].
- [7] Eesti Energia. (2020, April 22). Eesti Teaduste Akadeemia president Tarmo Soomere: lisaks julgetele lahendustele viib maailma edasi ka vajadus midagi teha. Available: <https://www.energia.ee/uudised/avalett/-/newsv2/2020/04/22/eesti-teaduste-akadeemia-president-tarmo-soomere-lisaks-julgetele-lahendustele-viib-maailma-edasi-ka-vajadus-midagi-teha> [Accessed 20th October 2021].
- [8] Konist A., & Uibu, M. (2021). Kliimamuutuste Leevendamise Läbi CCS Ja CCU Tehnoloogiate. Lõpparuanne, Project RITA1/02-20. Available: <https://www.etag.ee/wp-content/uploads/2021/04/L%C3%B5pparuanne.pdf> [Accessed 20th October 2021].
- [9] Veetil, S. K. P., Rebane, K., Yörük, C. R., Lopp, M., Triikkel, A., & Hitch, M. (2021). Aqueous mineral carbonation of oil shale mine waste (limestone): A feasibility study to develop a CO<sub>2</sub> capture sorbent. *Energy*, 221, 119895.
- [10] Sutter, H. (2020, April 6). Uue Enefit280 õlithase rajamiseks on õige aeg. Enefit; 2020. Available: <https://drive.google.com/file/d/1a6wLrgBTaVAqBvPGX41uYwl-PebUvws3/view> [Accessed 20th October 2021].
- [11] Kaldas, K., Preegel, G., Muldma, K., & Lopp, M. (2020). Wet Air Oxidation of Oil Shales: Kerogen Dissolution and Dicarboxylic Acid Formation. *ACS omega*, 5(35), 22021-22030.
- [12] Noll, R. (2012). Laser-induced breakdown spectroscopy. In *Laser-Induced Breakdown Spectroscopy*, pp. 7-15. Springer, Berlin, Heidelberg.

- [13] Dyni, J. R. (2006). Geology and resources of some of the world's oil-shale deposits. Scientific investigation report 2005–5294. U.S. *Geological Survey, Reston, VA*, 42.
- [14] Urov, K. E., & Sumberg, A. I. (1999). Characteristics of oil shales and shale-like rocks of known deposits and outcrops. *Estonian Acad. Publ. Oil Shale*, 16(3). pp. 1-64.
- [15] Reinsalu, E., & Aarna, I. (2015). About technical terms of oil shale and shale oil. *Oil shale*, 32(4). pp. 291-293.
- [16] Soesoo, A. (2014). More out from oil shale? *Oil Shale*, 31(3). pp. 207-210.
- [17] Oja, V., & Suuberg E. M. (2020). Oil Shale Processing, Chemistry and Technology. *Fossil Energy*. pp. 47-83.
- [18] Kann, J., Raukas, A., & Siirde, A. (2013). About The Gasification of Kukersite *Oil Shale*. *Oil Shale*, 30(2S), pp. 283-293.
- [19] Allix, P., Burnham, A., Fowler, T., Herron, M., Kleinberg, R., & Symington, B. (2010). Coaxing oil from shale. *Oilfield Review*, 22(4), pp. 4-15.
- [20] Väli, E., Valgma, I., & Reinsalu, E. (2008). Usage of Estonian oil shale. *Oil Shale*, 25(2S), pp. 101-114.
- [21] Francu, J., Harvie, B., Laenen, B., Siirde, A., Veiderma, M., Collins, P., & Steiger, F. (2007). A study on the EU oil shale industry—viewed in the light of the Estonian experience. A report by EASAC to the Committee on Industry, Research and Energy of the European Parliament. European Academies Science Advisory Council.
- [22] Plamus, K. (2012). The Impact of Oil Shale Calorific Value on CFB Boiler Thermal Efficiency and Environment. TUT Press.
- [23] Lille, Ü., Heinmaa, I., Pehk, T. (2003). Molecular model of Estonian kukersite kerogen as evaluated by <sup>13</sup>C MAS NMR spectra. *Fuel*, 82(7), pp. 799–804.
- [24] Kattai, V., & Lokk, U. (1998). Historical review of the kukersite oil shale exploration in Estonia. *Oil Shale*, 15(2), pp. 102-110.
- [25] Knaus, E., Killen, J., Biglarbigi, K., & Crawford, P. (2010). An overview of oil shale resources. In: Ogunsola, O.I., Hartstein, A., Ogunsola, O. (eds.) *Oil Shale: A Solution to the Liquid Fuel Dilemma. ACS Symposium Series*, 1032. American Chemical Society. pp. 3-20.
- [26] Arro, H., Prikk, A., & Pihu, T. (2003). Calculation of qualitative and quantitative composition of Estonian oil shale and its combustion products. Part 1. Calculation on the basis of heating value. *Fuel*, 82(18), 2179-2195.
- [27] Engineering ToolBox, (2010). Standard Grade Coal - Heat Values. Available: [https://www.engineeringtoolbox.com/coal-heating-values-d\\_1675.html](https://www.engineeringtoolbox.com/coal-heating-values-d_1675.html) [Accessed: 24th October 2021].
- [28] Valgma, I., Karu, V., Viil, A., & Lohk, M. (2007, January). Oil shale mining developments in Estonia as the bases for sustainable power industry. In: Lahtmets, R. (eds.) *4th International Symposium "Topical Problems in the Field of Electrical and Power Engineering": Doctoral School of Energy and Geotechnology: Kuressaare, Estonia*. Elektriajam, Tallinn.
- [29] Nikitin, O., Väli, E., Sabanov, S., & Pastarus, J. R. (2007, June). The surface miner sustainable technology introduction for oil-shale mining in Estonia. In: Noviks, G. Morozov, V. Tepfers, R. Leal, W. Chrzan, T. (eds.) *6th international Scientific and Practical Conference on Environment, Technology and Resources. Proceedings of the International Scientific and Practical Conference*, Vol. 1, pp. 55-61.

- [30] Väli, E. (2011). Analysis of oil shale high-selective mining with surface miner in Estonia. *Oil Shale*, 28(1), 49.
- [31] Šommet, J.; Sabanov, S.; Pastarus, J.-R. 2010. Analyses of crushed limestone quality developed by different methods for conditions of sustainable mining. *Проблемы Недропользования. Санкт-Петербургский Государственный Горный Инс*, 189(1). pp. 133-135.
- [32] Pastarus, J. R., Adamson, A., Sabanov, S., Väli, E., Nikitin, O. (2008). Wirtgen 2500 SM ja killustiku tootmine karjäärides. Killustiku kaevandamine ja kasutamine. Report, Tallinn University of Technology, Estonia.
- [33] Lohk, M., Väli, E., Tohver, T., & Pastarus, J. R. (2008, January). Surface miner technology impact on the environment. In: Lahtmetts, R. (eds.) *5th International Symposium "Topical problems in the field of electrical and power engineering"*. Doctoral school of energy and geotechnology. Tallinn University of Technology, pp. 44-47.
- [34] Adamson, A. (1998). Breakage of oil shale by mining. *Oil Shale*. 15(2), pp. 186-205.
- [35] Wikipedia contributors. (2020, October 4). Gravity separation. In *Wikipedia, The Free Encyclopedia*. Available: [https://en.wikipedia.org/w/index.php?title=Gravity\\_separation&oldid=981760654](https://en.wikipedia.org/w/index.php?title=Gravity_separation&oldid=981760654) [Accessed 21st October 2021].
- [36] Eesti Energia, Gravel: High quality is a valuable building material. Available: <https://www.energia.ee/en/ari/toostuslahendused/killustik> [Accessed: 24th October 2021].
- [37] Singh, A., & Parihar, S. (2020). A Technical Review on Use of Waste Material Plastic in Flexible Pavement. *Dogo Rangsang Research Journal*, 10(06).
- [38] Kuenen, J., Pacyna, J. M., Rentz, O., Oertel, D., Trozzi, C., Pulles, T., & Appelman, (2013). W. NFR: 2.A.2 Lime production, Guidebook 2013.
- [39] Hordijk, D. A., Wolsink, G. M., & De Vries, J. (1995). Fracture and fatigue behaviour of a high strength limestone concrete as compared to gravel concrete. *Heron-English Edition*, 40, pp. 125-146.
- [40] Kann, J., Elenurm, A., Rohtla, I., Golubev, N., Kaidalov, A., & Kindorkin, B. (2004). About thermal low-temperature processing of oil shale by solid heat carrier method. *Oil Shale*, 21(3), pp. 195-204.
- [41] Wikipedia contributors. (2021, August 1). Shale oil extraction. In *Wikipedia, The Free Encyclopedia*. Available: [https://en.wikipedia.org/w/index.php?title=Shale\\_oil\\_extraction&oldid=1036542956](https://en.wikipedia.org/w/index.php?title=Shale_oil_extraction&oldid=1036542956) [Accessed: 21st October 2021].
- [42] Wikipedia contributors. (2021, September 2). Kiviter process. In *Wikipedia, The Free Encyclopedia*. Available: [https://en.wikipedia.org/w/index.php?title=Kiviter\\_process&oldid=1041912781](https://en.wikipedia.org/w/index.php?title=Kiviter_process&oldid=1041912781) [Accessed: 21st October 2021].
- [43] Golubev, N. (2003). Solid oil shale heat carrier technology for oil shale retorting. *Oil Shale*, 20(3), pp. 324-332.
- [44] Neshumayev, D., Pihu, T., Siirde, A., Järvik, O., & Konist, A. (2019). Solid heat carrier oil shale retorting technology with integrated CFB technology. *Oil Shale*, 36(2S), pp. 99-113.

- [45] Yefimov, V. (2000). Oil shale processing in Estonia and Russia. *Oil Shale*, 17(4), pp. 367-385.
- [46] KKT kiviõli keemiatööstus. Production. Available: <https://www.keemiatööstus.ee/en/production/> [Accessed: 24th October 2021].
- [47] Gavrilova, O., Vilu, R., & Vallner, L. (2010). A life cycle environmental impact assessment of oil shale produced and consumed in Estonia. *Resources, conservation and recycling*, 55(2), pp. 232-245.
- [48] Bridgwater AV. (2012). Review of fast pyrolysis of biomass and product upgrading. *Biomass and bioenergy*, 38, pp. 68-94.
- [49] Kwon KC, Mayfield H, Marolla T, Nichols B, Mashburn M (2011). Catalytic deoxygenation of liquid biomass for hydrocarbon fuels. *Renew Energy* 36, pp. 907-915.
- [50] Kim, J. S. (2015). Production, separation and applications of phenolic-rich bio-oil—a review. *Bioresource technology*, 178, pp. 90-98.
- [51] Maaten, B., Järvik, O., Pihl, O., Konist, A., & Siirde, A. (2020). Oil shale pyrolysis products and the fate of sulfur. *Oil Shale*, 37(1), pp. 51-69.
- [52] Viru Keemia Grupp. Fine Chemicals. Available: <https://www.vkg.ee/en/fine-chemicals/> [Accessed: 24th October 2021].
- [53] Konist, A., Pihu, T., Neshumayev, D., & Siirde, A. (2013). Oil shale pulverized firing: boiler efficiency, ash balance and flue gas composition. *OilShale*, 30(1), pp. 6-18.
- [54] Pihu, T., Konist, A., Neshumayev, D., Loosaar, J., Siirde, A., Parve, T., & Molodtsov, A. (2012). Short-term tests on firing oil shale fuel applying low-temperature vortex technology. *Oil Shale*, 29(1), pp. 3-17.
- [55] Arro, H., Prikk, A., & Pihu, T. (2005). Combustion of Estonian oil shale in fluidized bed boilers, heating value of fuel, boiler efficiency and CO<sub>2</sub> emissions. *Oil Shale*, 22(4S), pp. 399-406.
- [56] Hotta, A., Parkkonen, R., Hiltunen, M., Arro, H., Loosaar, J., Parve, T., Pihu, T., Prikk, A., & Tiikma, T. (2005). Experience of Estonian oil shale combustion based on CFB technology at Narva Power Plants. *Oil Shale*, 22(4S), pp. 381-398.
- [57] Pihu, T., Arro, H., Prikk, A., Rootamm, R., & Konist, A. (2009). Corrosion of air preheater tubes of oil shale CFB boiler. Part 1. Dew point of flue gas and lowtemperature corrosion. *Oil Shale*, 26(1), pp. 5-12.
- [58] Suik, H., Pihu, T., & Molodtsov, A. (2008). Wear of the fuel supply system of CFB boilers. *Oil Shale*, 25(2), pp. 209-216.
- [59] Suik, H., & Pihu, T. (2009). Warranty reliability of CFB boiler burning oil shale. *Oil Shale*, 26(2), pp. 99-107.
- [60] Parve, T., Loosaar, J., Mahhov, M., & Konist, A. (2011). Emission of fine particulates from oil shale fired large boilers. *Oil Shale*, 28(1S), pp. 152-161.
- [61] Ots, A. (2007). Estonian oil shale properties and utilization in power plants. *Energetika*, (2).
- [62] Electrical4U (2020) Pulverized Fuel Firing of Boiler. Available: <https://www.electrical4u.com/pulverized-fuel-firing-of-boiler/> [Accessed: 24th October 2021].

- [63] Wikipedia contributors. (2021, March 31). Circulating fluidized bed. In *Wikipedia, The Free Encyclopedia*. Available: [https://en.wikipedia.org/w/index.php?title=Circulating\\_fluidized\\_bed&oldid=1015336386](https://en.wikipedia.org/w/index.php?title=Circulating_fluidized_bed&oldid=1015336386) [Accessed: 21st October 2021].
- [64] Hupa, M. (2005). Interaction of fuels in co-firing in FBC. *Fuel*, 84(10), pp. 1312-1319.
- [65] Vamvuka, D., Pitharoulis, M., Alevizos, G., Repouskou, E., & Pentari, D. (2009). Ash effects during combustion of lignite/biomass blends in fluidized bed. *Renewable Energy*, 34(12), pp. 2662-2671.
- [66] Doshi, V., Vuthaluru, H. B., Korbee, R., & Kiel, J. H. (2009). Development of a modeling approach to predict ash formation during co-firing of coal and biomass. *Fuel Processing Technology*, 90(9), pp. 1148-1156.
- [67] Basu, P., Butler, J., & Leon, M. A. (2011). Biomass co-firing options on the emission reduction and electricity generation costs in coal-fired power plants. *Renewable energy*, 36(1), pp. 282-288.
- [68] Aho, M., Envall, T., & Kauppinen, J. (2013). Corrosivity of flue gases during co-firing Chinese biomass with coal at fluidised bed conditions. *Fuel processing technology*, 105, pp. 82-88.
- [69] Pronobis, M. (2006). The influence of biomass co-combustion on boiler fouling and efficiency. *Fuel*, 85(4), pp. 474-480.
- [70] Konist, A., Pihu, T., Neshumayev, D., & Kuelaots, I. (2013). Low Grade Fuel-Oil Shale and Biomass Co-Combustion in CFB Boiler. *Oil Shale*, 30.
- [71] Jantti, T., Sarkki, J., & Lampenius, H. (2010, June). The Utilization of CFB Technology for Large-Scale Biomass Firing Power Plants. *Power-Gen Europe*, pp. 8-10.
- [72] Eesti Energia, Oil shale ash: By using ash you are contributing to the circular economy. Available: <https://www.energia.ee/en/ari/toostuslahendused/tuhk> [Accessed: 25th October 2021].
- [73] Laur, T., & Kikas, V. (2000). Oil Shale Ash: Its Characterization and Possible Use in Remediation at the Sillamäe Site. In: *Turning a Problem into a Resource: Remediation and Waste Management at the Sillamäe Site, Estonia*, pp. 207-213. Springer, Dordrecht.
- [74] Blinova, I., Bityukova, L., Kasemets, K., Ivask, A., Käkinen, A., Kurvet, I., ... & Kahru, A. (2012). Environmental hazard of oil shale combustion fly ash. *Journal of Hazardous Materials*, 229, pp. 192-200.
- [75] Arro, H., Loosaar, J., Pihu, T., & Prikk, A. (2007). Estonian oil shale power plants' ash handling problems. *Energy and Sustainability, WIT Transactions on Ecology and the Environment*, 105, pp. 247-255
- [76] Eesti Energia, Enefit. Value-added Revenue Streams. Available: <https://www.enefit.com/by-products/home> [Accessed: 24th October 2021].
- [77] Romanovich, G. (2019) Unustatud põlevkivituhk jõuab taas põldudele. Põhjarannik, January 24, 2019. Available: <https://pohjarannik.postimees.ee/6506409/unustatud-polevkivituhk-jouab-taas-poldudele> [Accessed: 24th October 2021].
- [78] Hilger, J. (2003). Combined utilization of oil shale energy and oil shale minerals within the production of cement and other hydraulic binders. *Oil shale*, 20(3; SUPP), pp. 347-355.

- [79] Hanni, R. (1996). Energy and valuable material by-product from firing Estonian oil shale. *Waste Management*, 16(1-3), pp. 97-99.
- [80] Al-Hasan, M. (2006). Behavior of concrete made using oil shale ash and cement mixtures. *Oil Shale*, 23(2), pp. 135-143.
- [81] Kikas, V., Rass, J., & Hralovich, J. (1986). Influence of ash content of Kukuriste oil shale on the properties of self-stressing shale ash cement. *Proceedings of Tallinn Polytechnic Institute*, 618(9), 17.
- [82] Sarapik, A. (ed.) (2016). Eesti Energia to begin wholesale distribution of oil shale ash fertilizer, April 21, 2016 Available: <https://news.err.ee/118034/eesti-energia-to-begin-wholesale-distribution-of-oil-shale-ash-fertilizer> [Accessed: 23rd October 2021].
- [83] Vänäa, R. (12 June 2020), Press Release: Ragn-Sells invests in resource saving carbon capture and utilisation project in Estonia. Available: <https://www.mynewsdesk.com/ragnsells/pressreleases/ragn-sells-invests-in-resource-saving-carbon-capture-and-utilisation-project-in-estonia-3007479> [Accessed: 23rd October 2021].
- [84] Valgma, I., Reinsalu, E., Sabanov, S., & Karu, V. (2010). Quality control of oil shale production in Estonian mines. *Oil Shale*, 27(3), pp. 239-249.
- [85] Reinsalu, E. (2000). Relationship between crude mineral cost and quality. *Mineral Resources Engineering*, 9(02), pp. 205-213.
- [86] Estonian Centre for Standardisation and Accreditation (EVS-ISO 1928:2016) Available: <https://www.evs.ee/en/evs-iso-1928-2016> [Accessed: 23rd October 2021].
- [87] Estonian Centre for Standardisation and Accreditation (EVS 668:2018) Available: <https://www.evs.ee/et/evs-668-2018> [Accessed: 23rd October 2021].
- [88] Atwater, Gordon, I., Riva, Joseph P. and Boak, J. (2020, January 28). *Oil shale*. *Encyclopedia Britannica*. Available: <https://www.britannica.com/science/oil-shale> [Accessed: 23rd October 2021].
- [89] Wikipedia contributors. (2021, October 17). Environmental impact of the oil shale industry. In *Wikipedia, The Free Encyclopedia*. Available: [https://en.wikipedia.org/w/index.php?title=Environmental\\_impact\\_of\\_the\\_oil\\_shale\\_industry&oldid=1050460655](https://en.wikipedia.org/w/index.php?title=Environmental_impact_of_the_oil_shale_industry&oldid=1050460655) [Accessed: 21st October 2021].
- [90] European Academies Science Advisory Council, (2007). A study on the EU oil shale industry--viewed in the light of the Estonian experience. *A report by EASAC to the Committee on Industry, Research and Energy of the European Parliament*. Available: <https://easac.eu/publications/details/study-on-the-eu-oil-shale-industry/> [Accessed: 23rd October 2021].
- [91] Molder, L. (2004). Estonian oil shale retorting industry at the crossroads. *Oil Shale*, 21(2), pp. 97-99.
- [92] Tuvikene, A., Huuskonen, S., Koponen, K., Ritola, O., Mauer, U., & Lindström-Seppä, P. (1999). Oil shale processing as a source of aquatic pollution: monitoring of the biologic effects in caged and feral freshwater fish. *Environmental Health Perspectives*, 107(9), pp. 745-752.
- [93] Republic of Estonia Ministry of Environment. (15th July 2021) Waste, emissions Circular economy. Available: <https://www.envir.ee/en/waste> [Accessed: 23rd October 2021].

- [94] Kahru, A., & Põllumaa, L. (2006). Environmental hazard of the waste streams of Estonian oil shale industry: an ecotoxicological review. *Oil Shale*, 23(1), pp. 53-93.
- [95] Anku, W. W., Mamo, M. A., & Govender, P. P. (2017). Phenolic compounds in water: sources, reactivity, toxicity and treatment methods. *Phenolic compounds-natural sources, importance and applications*, pp. 420-443.
- [96] Gad, N. S., & Saad, A. S. (2008). Effect of environmental pollution by phenol on some physiological parameters of *Oreochromis niloticus*. *Global Veterinaria*, 2(6), pp. 312-319.
- [97] Teinemaa, E., Kirso, U., Strommen, M. R., & Kamens, R. M. (2003). Deposition flux and atmospheric behavior of oil shale combustion aerosols. *Oil Shale*, 20(3; SUPP), pp. 429-440.
- [98] Wan, J. Q. (2009). Environmental impacts of oil shale and pollution control technologies. In: Jinsheng, G. (eds.) *Coal, Oil Shale, Natural Bitumin, Heavy Oil and Peat*, 2, pp. 129-40.
- [99] Sheta, S., Afgan, M. S., Hou, Z., Yao, S. C., Zhang, L., Li, Z., & Wang, Z. (2019). Coal analysis by laser-induced breakdown spectroscopy: a tutorial review. *Journal of Analytical Atomic Spectrometry*, 34(6), pp. 1047-1082.
- [100] Bogaerts, A., & Chen, Z. (2005). Effect of laser parameters on laser ablation and laser-induced plasma formation: A numerical modeling investigation. *Spectrochimica Acta Part B: Atomic Spectroscopy*, 60(9-10), pp. 1280-1307.
- [101] Lindon, J. C., Tranter, G. E., & Koppenaal, D. (2016). *Encyclopedia of spectroscopy and spectrometry*. Academic Press.
- [102] Pasquini, C., Cortez, J., Silva, L., & Gonzaga, F. B. (2007). Laser induced breakdown spectroscopy. *Journal of the Brazilian Chemical Society*, 18(3), pp. 463-512.
- [103] Russo, R. E. (1995). Laser ablation. *Applied Spectroscopy*, 49(9), 14A-28A.
- [104] Laan, M., Aints, M., Hakola, A., Karhunen, J., Likonen, J., Lissovski, A., Paris, P. (2011). Laser induced plasma spectroscopy, EFDA Work Programme 2011 Emerging Technologies & System Integration, Dust and Tritium Management, Task WP11-ETS-DTM-01-05/TEKES/BS, Task WP11-ETS-DTM-01-05-02/TEKES/PS, Final report University of Tartu.
- [105] Hahn, D. W., & Omenetto, N. (2010). Laser-induced breakdown spectroscopy (LIBS), part I: review of basic diagnostics and plasma-particle interactions: still-challenging issues within the analytical plasma community. *Applied Spectroscopy*, 64(12), 335A-366A.
- [106] Mao, X. L., Ciocan, A. C., Borisov, O. V., & Russo, R. E. (1998). Laser ablation processes investigated using inductively coupled plasma-atomic emission spectroscopy (ICP-AES). *Applied surface science*, 127, pp. 262-268.
- [107] Cabalin, L. M., & Laserna, J. J. (1998). Experimental determination of laser induced breakdown thresholds of metals under nanosecond Q-switched laser operation. *Spectrochimica Acta Part B: Atomic Spectroscopy*, 53(5), pp. 723-730.
- [108] Anabitarte, F., Cobo, A., & Lopez-Higuera, J. M. (2012). Laser-induced breakdown spectroscopy: fundamentals, applications, and challenges. *International Scholarly Research Network, 2012*, pp. 12. Available: <https://doi.org/10.5402/2012/285240> [Accessed: 23rd October 2021]

- [109] Cho, Y., Sugita, S., Ishibashi, K., Ohno, S., Kamata, S., Kurosawa, K. & Matsui, T. (2010, March). Effects of Laser Energy on LIBS Spectra. In *Lunar and Planetary Science Conference* (No. 1533, p. 2158). Available: <https://www.lpi.usra.edu/meetings/lpsc2010/pdf/2158.pdf> [Accessed: 23rd October 2021]
- [110] Konidala, S. K., Kamala, G., & Koralla, S. (2016). Laser induced breakdown spectroscopy. *Research Journal of Pharmacy and Technology*, 9(1), pp. 91-100.
- [111] Coons, R. W., Harilal, S. S., Hassan, S. M., & Hassanein, A. (2012). The importance of longer wavelength reheating in dual-pulse laser-induced breakdown spectroscopy. *Applied Physics B*, 107(3), pp. 873-880.
- [112] Fahad, M., Farooq, Z., & Abrar, M. (2019). Comparative study of calibration-free laser-induced breakdown spectroscopy methods for quantitative elemental analysis of quartz-bearing limestone. *Applied optics*, 58(13), pp. 3501-3508.
- [113] Rai, V. N. (2014). Laser-induced breakdown spectroscopy: A versatile technique of elemental analysis and its applications. *arXiv preprint arXiv:1407.0132*.
- [114] Ball, D. W. (2006). *Field guide to spectroscopy* (Vol. 8). Bellingham, Washington: Spie Press.
- [115] Zhang, D. C., Hu, Z. Q., Su, Y. B., Hai, B., Zhu, X. L., Zhu, J. F., & Ma, X. (2018). Simple method for liquid analysis by laser-induced breakdown spectroscopy (LIBS). *Optics express*, 26(14), pp. 18794-18802.
- [116] Luo, W., Tang, J., Gao, C., Wang, H., & Zhao, W. (2010). Spectroscopic analysis of element concentrations in aluminum alloy using nanosecond laser-induced breakdown spectroscopy. *Physica Scripta*, 81(6), 065302.
- [117] Xiong, Z., Hao, Z., Li, X., & Zeng, X. (2019). Investigation on the reduction of self-absorption effects in quantitative analysis using fiber laser ablation laser-induced breakdown spectroscopy. *Journal of Analytical Atomic Spectrometry*, 34(8), pp. 1606-1610.
- [118] Aguilera, J. A., & Aragón, C. (2008). Characterization of laser-induced plasmas by emission spectroscopy with curve-of-growth measurements. Part II: Effect of the focusing distance and the pulse energy. *Spectrochimica Acta Part B: Atomic Spectroscopy*, 63(7), pp. 793-799.
- [119] Paris, P., Piip, K., Lepp, A., Lissovski, A., Aints, M., & Laan, M. (2015). Discrimination of moist oil shale and limestone using laser induced breakdown spectroscopy. *Spectrochimica Acta Part B: Atomic Spectroscopy*, 107, pp. 61-66.
- [120] Awasthi, S., Kumar, R., Devanathan, A., Acharya, R., & Rai, A. K. (2017). Multivariate methods for analysis of environmental reference materials using laser-induced breakdown spectroscopy. *Analytical chemistry research*, 12, pp. 10-16.
- [121] Guezenc, J., Gallet-Budynek, A., & Bousquet, B. (2019). Critical review and advices on spectral-based normalization methods for LIBS quantitative analysis. *Spectrochimica Acta Part B: Atomic Spectroscopy*, 160, 105688.
- [122] Zheng, J., Lu, J., Zhang, B., Dong, M., Yao, S., Lu, W., & Dong, X. (2014). Experimental study of laser-induced breakdown spectroscopy (LIBS) for direct analysis of coal particle flow. *Applied spectroscopy*, 68(6), pp. 672-679.
- [123] Jolliffe, I. T. (1986). Principal components in regression analysis. In *Principal component analysis*, pp. 129-155. Springer, New York, NY.

- [124] Abdi, H. (2003). Partial least square regression (PLS regression). *Encyclopedia for research methods for the social sciences*, 6(4), pp. 792-795.
- [125] Wang, Z., Feng, J., Li, L., Ni, W., & Li, Z. (2011). A multivariate model based on dominant factor for laser-induced breakdown spectroscopy measurements. *Journal of Analytical Atomic Spectrometry*, 26(11), pp. 2289-2299.
- [126] Abbass, Q., Ahmed, N., Ahmed, R., & Baig, M. A. (2016). A comparative study of calibration free methods for the elemental analysis by laser induced breakdown spectroscopy. *Plasma Chemistry and Plasma Processing*, 36(5), pp. 1287-1299.
- [127] Redoglio, D., Golinelli, E., Musazzi, S., Perini, U., & Barberis, F. (2016). A large depth of field LIBS measuring system for elemental analysis of moving samples of raw coal. *Spectrochimica Acta Part B: Atomic Spectroscopy*, pp. 116, 46-50.
- [128] Gaft, M., Dvir, E., Modiano, H., & Schone, U. (2008). Laser induced breakdown spectroscopy machine for online ash analyses in coal. *Spectrochimica Acta Part B: Atomic Spectroscopy*, 63(10), pp. 1177-1182.
- [129] Gaft, M., Sapir-Sofer, I., Modiano, H., & Stana, R. (2007). Laser induced breakdown spectroscopy for bulk minerals online analyses. *Spectrochimica Acta Part B: Atomic Spectroscopy*, 62(12), pp. 1496-1503.
- [130] Body, D., & Chadwick, B. L. (2001). Simultaneous elemental analysis system using laser induced breakdown spectroscopy. *Review of Scientific Instruments*, 72(3), pp. 1625-1629.
- [131] Ctvrtnickova, T., Mateo, M. P., Yanez, A., & Nicolas, G. (2011). Application of LIBS and TMA for the determination of combustion predictive indices of coals and coal blends. *Applied surface science*, 257(12), pp. 5447-5451.
- [132] Yao, S., Lu, J., Dong, M., Chen, K., Li, J., & Li, J. (2011). Extracting coal ash content from laser-induced breakdown spectroscopy (LIBS) spectra by multivariate analysis. *Applied spectroscopy*, 65(10), pp. 1197-1201.
- [133] Chen, M., Yuan, T., Hou, Z., Wang, Z., & Wang, Y. (2015). Effects of moisture content on coal analysis using laser-induced breakdown spectroscopy. *Spectrochimica Acta Part B: Atomic Spectroscopy*, 112, pp. 23-33.
- [134] Yuan, T., Wang, Z., Lui, S. L., Fu, Y., Li, Z., Liu, J., & Ni, W. (2013). Coal property analysis using laser-induced breakdown spectroscopy. *Journal of Analytical Atomic Spectrometry*, 28(7), pp. 1045-1053.
- [135] Washburn, K. E. (2015). Rapid geochemical and mineralogical characterization of shale by laser-induced breakdown spectroscopy. *Organic Geochemistry*, 83, pp. 114-117.
- [136] Birdwell, J. E., & Washburn, K. E. (2015). Rapid analysis of kerogen hydrogen-to-carbon ratios in shale and mudrocks by laser-induced breakdown spectroscopy. *Energy & Fuels*, 29(11), pp. 6999-7004.
- [137] Sanghapi, H. K., Jain, J., Bol'Shakov, A., Lopano, C., McIntyre, D., & Russo, R. (2016). Determination of elemental composition of shale rocks by laser induced breakdown spectroscopy. *Spectrochimica Acta Part B: Atomic Spectroscopy*, 122, pp. 9-14.
- [138] Pasquini, C. (2003). Near infrared spectroscopy: fundamentals, practical aspects and analytical applications. *Journal of the Brazilian chemical society*, 14(2), pp. 198-219.

- [139] Fang, Q., Hong, H., Zhao, L., Kukolich, S., Yin, K., & Wang, C. (2018). Visible and near-infrared reflectance spectroscopy for investigating soil mineralogy: A review. *Journal of Spectroscopy*.
- [140] Companion, A. L. (1965). Theory and applications of diffuse reflectance spectroscopy. In: Davis E.N. (eds.) *Developments in Applied Spectroscopy*, Vol 4. pp. 221-234. Springer, Boston, MA.
- [141] Fuller, M. P., & Griffiths, P. R. (1978). Diffuse reflectance measurements by infrared Fourier transform spectrometry. *Analytical chemistry*, 50(13), pp. 1906-1910.
- [142] Scott Little, P., & Kempfert, K. (2004). What's New at PIKE Technologies? Available: <http://monoceros.physics.muni.cz/~jancely/PPL/Texty/IntegracniKoule/Integrating%20Sphere.pdf> Accessed [23rd Oct 2021]
- [143] Holger, L. (2012). PowerPoint-Präsentation: Company Bruker Optik GmbH.
- [144] Oriol Instruments. (2002). Introduction to FT-IR Spectroscopy. Available: [https://www3.pi2.uni-stuttgart.de/official/g.denninger/EXP\\_SS2004/PDF/ftir\\_introduction.pdf](https://www3.pi2.uni-stuttgart.de/official/g.denninger/EXP_SS2004/PDF/ftir_introduction.pdf) [Accessed: 24th October 2021].
- [145] Merenda, F. (2009). Basics: Fourier Transform Spectrometry. ARCOptix, Switzerland.
- [146] Tsuchikawa, S., & Kobori, H. (2015). A review of recent application of near infrared spectroscopy to wood science and technology. *Journal of Wood Science*, 61(3), pp. 213-220.
- [147] Jamrógiewicz, M. (2012). Application of the near-infrared spectroscopy in the pharmaceutical technology. *Journal of pharmaceutical and biomedical analysis*, 66, pp. 1-10.
- [148] He, C., Yang, Z., Chen, L., Huang, G., Liao, N., & Han, L. (2014). Influencing factors of on-line measurement of straw-coal blends using near infrared spectroscopy. *Transactions of the Chinese Society of Agricultural Engineering*, 30(9), pp. 192-200.
- [149] Andres, J. M., & Bona, M. T. (2005). Analysis of coal by diffuse reflectance near-infrared spectroscopy. *Analytica chimica acta*, 535(1-2), pp. 123-132.
- [150] Bona, M. T., & Andrés, J. M. (2007). Coal analysis by diffuse reflectance near-infrared spectroscopy: Hierarchical cluster and linear discriminant analysis. *Talanta*, 72(4), pp. 1423-1431.
- [151] Romeo, M. J., Adams, M. J., Hind, A. R., Bhargava, S. K., & Grocott, S. C. (2002). Near infrared prediction of oil yield from oil shale. *Journal of near infrared spectroscopy*, 10(3), pp. 223-231.
- [152] Aosaar, H. (2015). Põlevkivi proovid Narva ja Eesti kaevandustest. Report, Estonian Energy.
- [153] Riisalu, H. (2019) private communication.
- [154] O'Kelly, B. C. (2005). Oven-drying characteristics of soils of different origins. *Drying technology*, 23(5), pp. 1141-1149.
- [155] Glen, S. (2021). Covariance in Statistics: What is it? Example. In: *StatisticsHowTo.com: Elementary Statistics for the rest of us!* Available: <https://www.statisticshowto.com/probability-and-statistics/statistics-definitions/covariance/> [Accessed 24th October 2021].
- [156] Martens, H., & Naes, T. (1992). *Multivariate calibration*. John Wiley & Sons.

- [157] El Haddad, J., Canioni, L., & Bousquet, B. (2014). Good practices in LIBS analysis: Review and advices. *Spectrochimica Acta Part B: Atomic Spectroscopy*, 101, pp. 171-182.
- [158] Gaffey, S. J. (1986). Spectral reflectance of carbonate minerals in the visible and near infrared (0.35-2.55 microns); calcite, aragonite, and dolomite. *American Mineralogist*, 71(1-2), pp. 151-162.
- [159] Gunasekaran, S., Anbalagan, G., & Pandi, S. (2006). Raman and infrared spectra of carbonates of calcite structure. *Journal of Raman Spectroscopy: An International Journal for Original Work in all Aspects of Raman Spectroscopy, Including Higher Order Processes, and also Brillouin and Rayleigh Scattering*, 37(9), pp. 892-899.
- [160] Douglas, R. K., Nawar, S., Alamar, M. C., Mouazen, A. M., & Coulon, F. (2018). Rapid prediction of total petroleum hydrocarbons concentration in contaminated soil using vis-NIR spectroscopy and regression techniques. *Science of the Total Environment*, 616, pp. 147-155.

## Acknowledgements

First and foremost, I would like to say special thanks to my supervisors, Prof. Jaan Kalda and Associate Prof. Matti Laan for their guidance, support and encouragement during my study period and they have all taken their tasks seriously and read my drafts thoroughly. Matti, who is my co supervisor has shown a special interest for the big picture and several times presented various new interpretations of my material.

My thanks belong to all members of the plasma physics laboratory UT, where were done all my measurements and where I participated on seminars. I am especially thankful to Dr. Peeter Paris for his technical support throughout in labs for my experiments. I am thankful for Mr. Andres Siiman who provide us device and guidance about device for the DRS experiments. I thank Dr. Hella Riisallu who helped us in interpretation of our results. I also thanks Dr. Märt Aints who had done some Mathcad programs used in calculations.

I am thankful for my colleagues Dr. Indrek Jõgi, Dr. Jüri Raud for their guidance, suggestions and encouragements during my PhD study.

I am especially thankful to Jawad Hassan who helped me in arriving Estonia and thanks to Irina Bichele who helped in adjusting here in Estonia.

I would like to express my particular gratitude to all people in Estonia who have helped me in various ways for this work.

I would like to express my gratitude to all my friends and their families in Estonia, whose presence made my stay in Estonia more fun. Thank you all.

Finally, none of this would have been possible without the love, countless prayers, continuous encouragement, and unwavering support of my parents. I will be eternally grateful, for everything you have done for me since my childhood. Special thanks to my sister and brothers (Abida, Mubasher, Mohsin) for their love and care. I would also like to thank my mother and father in law and all in law's family for their prayers and advices.

I would not have finished this thesis without support, encouragement and help of my husband Muhammad Tufail who helped me throughout in my PhD journey, my daughter Ambar Fatima (8 years old), who says "she wants to become an author, but not writing '*boring books*' like me". My son Subhan Hassan (4 Years old), who was born, nursed and raised with this thesis, have not expressed any opinion about my work, yet. Perhaps he will, once he start school.

I express my gratitude to the following entities for their financial support during my PhD studies:

- Estonian National Scholarship Programme for International Students, Researchers and Academic staff.
- EURUfusion program and contract with the Institute of Technology of the UT where I partly participated in LIBS studies.

## Abstract

### Fast Assessment of Oil Shale Quality by Spectral Methods

The yield of oil as well as the efficiency the oil shale valorization in other fields, depend on the information about the content of organic and inorganic parts of the raw material. However, the present time-consuming laboratory testing could not meet the requirement of real-time control of oil shale composition and optimization of non-stop industrial processes. Among different on-line quality control methods, the optical methods are non-invasive and user-friendly.

In the present cycle of studies, the main attention is paid to the characterization of oil shale by laser induced breakdown spectroscopy (LIBS) technique. Results of another optical method, diffused reflectance spectroscopy (DRS) is used for comparison.

The aim of the thesis was to evaluate the feasibility of using LIBS for determination of calorific value and moisture content in conditions comparable to those of industrial ones.

Specimens for the study were collected from the layers of the Narva open cast mine and from the stopped conveyor belt of the beneficiation plant of the Estonia underground mine. For calibration of the results obtained by optical methods, traditional laboratory methods have been used. The gross calorific value of the samples was determined by calorific bomb method. The content of moisture of specimens was varied and the quantity of moisture was found by weighing. In all, 75 crushed oil shale samples with different calorificity and/or moisture content were used.

Experiments were carried out in ambient air at atmospheric pressure. Oil shale lumps of different size and orientation were spread out on the rotating stage which was a mock-up of the running conveyor belt. Results obtained with crushed oil shale samples were compared with those found by LIBS testing of powder pellet samples.

In LIBS setup pulsed Nd:YAG laser ( $\lambda = 532 \text{ nm}$ ) was used and a single-shot spectra were recorded in 220–850 nm wavelength range. Each sample was characterized by 375 single-shot spectra. DRS measurements were carried out using a multipurpose analyzer, where near infrared spectrum was recorded in 12500–3600  $\text{cm}^{-1}$  (800–2780 nm) interval. The average of 355 spectra characterized each sample.

As a first step of LIBS data preprocessing, covariance between the gross calorific value (or moisture content) and different spectral lines as well as between different pairs of spectral lines were found. On the basis of this information a set of spectral lines was chosen, which was used in the further analysis. The intensity of the carbon line has a strong correlation with the calorific value and the variation of moisture does not change it remarkably. However, the accuracy of prediction of the calorific value only on the basis of the carbon line intensities was not high enough and calculations of the calorific value and the moisture content were made by using the ordinary linear regression model. It appeared that a set of ca 10 spectral lines gave a minimum value of the standard deviation of prediction.

For DRS data analysis, from the options of the device software, the partial least square linear regression method was used.

In case of crushed oil shale samples, the standard deviation of prediction of the calorific value was 1.76  $\text{MJ kg}^{-1}$  and that of the moisture content was 1.94%. The corresponding value found by DRS were 0.85  $\text{MJ kg}^{-1}$  and 1.35%. At the same time, the standard deviation of the calorific value of air-dry powder pellets samples was 0.24  $\text{MJ kg}^{-1}$ . Comparison of these results allowed us to find out two main reasons which determine the standard deviations for the parameters of crushed oil shale samples.

The first reason was the uncertainty of measuring the moisture content. It is likely that in the case of a real conveyor belt and as-mined oil shale, the uncertainty will be considerably smaller. The second reason was that a linear regression model was applied instead of a nonlinear one; using a nonlinear estimation model reduced the standard deviation of calorific value to almost as small values as what were observed for DRS measurements.

Additionally, LIBS allowed us to predict the concentrations of main chemical species with a 5% accuracy.

To sum up, our study shows that LIBS is a technique which makes it possible to perform real-time on-line control of the oil shale properties.

## Lühikokkuvõte

### Põlevkivi kvaliteedi kiirmääramine spektraalsetel meetoditel

Nii õlisaagis kui ka teiste põlevkivi väärtustamisviiside efektiivsus sõltub teabest toorme orgaanilise ja anorgaanilise osa koosseisu kohta. Paraku on praegused laboratoorsed põlevkivi testimisviisid aeganõudvad ja ei pruugi vastata pideva tootmisprotsessi kontrollile/juhtimisele reaajas. Optilised meetodid, mis võimaldavad pidevalt toimivate protsesside kontrolli reaajas, on kontaktivabad ja kasutajasõbralikud. Käesolevas uurimistsükliis on põhitähelepanu pööratud laserindutseeritud läbilöögi spektroskoopiale (LIBS), kus laservälke mõjul aurustatakse väike hulk märklaua materjalist ja registreeritakse tekkinud plasma spekter. Saadud tulemusi võrreldakse teise optilise meetodiga, difuusse peegeldumise spektroskoopia (DRS), saadud tulemustega. Dissertatsiooni eesmärgiks oli hinnata LIBSi kasutatavust tükikivi kütteväärtuse ja niiskusesisalduse määramiseks tingimustes, mis on lähedased tööstuslikele.

Tükikivi eksemplarid koguti Narva karjääri põlevkivikihtidest ja Estonia kaevanduse rikastusvabriku konveierilindilt. Optiliste mõõtmistulemuste kalibreerimiseks kasutati traditsioonilisi laboratoorseid meetodeid. Ülemine kütteväärtus määrati kalorimeetrilise pommiga ja niiskusesisaldus määrati kaalumismeetodil. Ühtekokku oli testimiseks 75 tükikivi objekti, mida iseloomustas erinev kütteväärtus ja/või niiskusesisaldus.

Eksperimendikeskkonnaks oli laboriõhk atmosfäärirõhul. Erineva suuruse ja orientatsiooniga põlevkivitükid paiknesid pöörleval alusel, mis kujutas endast konveierilindi imitatsiooni. Tükikivi testimistulemusi võrreldi tulemustega, mis saadi põlevkivipulbrist tablettide testimisel.

LIBSi katseesetades kasutati Nd:YAG impulslaserit ( $\lambda = 532$  nm) ning ühe laservälke tulemusena registreeriti spekter lainepikkuste vahemikus 220–850 nm. Igat objekti iseloomustati 375 üksispektriga. DRS mõõtmised tehti tööstusliku multi-analüsaatoriga, mis registreeris spektri vahemikus 12500–3600  $\text{cm}^{-1}$  (800–2780 nm).

LIBSi andmete eeltötluse esimeseks sammuks oli kütteväärtuse ja erinevate elementide spektrijoonte kovariatsiooniväärtuste leidmine, samuti leiti erinevate spektrijoonte vahelised kovariatsioonid. Selle informatsiooni baasil valiti edasiseks analüüsiks kasutatavad spektrijooned. Süsiniku spektrijoone korrelatsioon kütteväärtusega oli tugev ja niiskusesisalduse mõju oli väike. Ilmnes aga, et kütteväärtuse prognoosi täpsus süsiniku spektrijoone järgi ei ole piisav ning objektide kütteväärtuse ja niiskusesisalduse leidmiseks kasutati mitme-muutuva lineaarse regressiooni mudelit. Saadud tulemused näitasid, et prognoosi iseloomustava standardhälbe miinimum saavutatakse  $\approx 10$  spektrijoone kasutamisel. DRS andmete töötlemiseks valiti multi-analüsaatori tarkvarast osaline vähimruutude meetodi algoritm.

Tükikivi objektide kütteväärtuse prognoosi iseloomustas standardhälve 1.76  $\text{MJ kg}^{-1}$  ja niiskusesisalduse puhul oli standardhälveks 1.94%. DRSi iseloomustavad suurused olid vastavalt 0.85  $\text{MJ kg}^{-1}$  ja 1.35%. Õhk-kuivade tablettide kütteväärtuse standardhälveks aga oli 0.24  $\text{MJ kg}^{-1}$ . Nende arvnäitude võrdlus lubas välja selgitada kaks peamist põhjust, mis määravad tükikivi objektide standardhälve. Esimeseks põhjuseks oli niiskusesisalduse leidmise määramatus. On tõenäoline, et reaalse konveierilindi puhul saab seda määramatust oluliselt vähendada. Teine põhjus seisnes oletuses, et spektrijoonte ja kütteväärtuse vaheline seos on lineaarne, kuid kasutades nende suuruste vahelise sõltuvuse hindamiseks ruutsõltuvust, saime kütteväärtuse standardhälveks DRS standardhälvega ligilähedase väärtuse.

Lisaks kütteväärtuse ja niiskusesisalduse määramisele võimaldas LIBS 5% täpsusega määrata põlevkivi peamiste keemiliste ühendite kontsentratsioonid.

Töö tulemusena leidsime, et LIBS on meetod, mis võimaldab põlevkivi omaduste kontrolli reaalajas.

# Appendix 1

## Paper - P I

Aints, M., Paris, P., Laan, M., Piip, K., Riisalu, H., & Tufail, I. (2018). Determination of heating value of Estonian oil shale by laser-induced breakdown spectroscopy. *Journal of Spectroscopy*, 2018.



## Research Article

# Determination of Heating Value of Estonian Oil Shale by Laser-Induced Breakdown Spectroscopy

M. Aints,<sup>1</sup> P. Paris ,<sup>1</sup> M. Laan,<sup>1</sup> K. Piip,<sup>1</sup> H. Riisalu,<sup>2</sup> and I. Tufail<sup>1</sup>

<sup>1</sup>*Institute of Physics, University of Tartu, Tartu, Estonia*

<sup>2</sup>*Virumaa College, Tallinn University of Technology, Kohtla-Järve, Estonia*

Correspondence should be addressed to P. Paris; peeter.paris@ut.ee

Received 25 August 2017; Revised 3 November 2017; Accepted 21 November 2017; Published 9 January 2018

Academic Editor: Alessandro De Giacomo

Copyright © 2018 M. Aints et al. This is an open access article distributed under the Creative Commons Attribution License, which permits unrestricted use, distribution, and reproduction in any medium, provided the original work is properly cited.

The laser-induced breakdown spectroscopy (LIBS) combined with multivariate regression analysis of measured data were utilised for determination of the heating value and the chemical composition of pellets made from Estonian oil shale samples with different heating values. The study is the first where the oil shale heating value is determined on the basis of LIBS spectra. The method for selecting the optimal number of spectral lines for ordinary multivariate least squares regression model is presented. The correlation coefficient between the heating value predicted by the regression model, and that measured by calorimetric bomb, was  $R^2 = 0.98$ . The standard deviation of prediction was 0.24 MJ/kg. Concentrations of oil shale components predicted by the regression model were compared with those measured by ordinary methods.

## 1. Introduction

Oil shale is used for production of fuel oil and various chemical products and is also used as a fuel in Estonian power plants. New boilers of oil shale power plants as well as oil retorts require a relatively constant quality of raw materials and fuel. The basic parameter of oil shale quality is the heating value. Heating value can vary considerably within the location in a deposit and depends substantially on concretions and limestone content [1]. Optimal operation of boilers requires continuous monitoring of heating value of incoming fuel. Up to now, the heating value of oil shale in laboratories of Estonian enterprises is measured using oxygen bomb calorimeters, which are the standard instruments for measuring heating values of solid and liquid combustible samples. However, this precise method is time consuming and thus not useable for online monitoring of the continuous flow of raw material.

Laser-induced breakdown spectroscopy (LIBS) as a fast diagnostic method has been widely used for characterization of coals and lignite. Overview of activities in this field can be found for example in [2] and references therein. LIBS

adapted with advanced data processing methods provides real-time information required by boiler operators nowadays. In addition to elemental composition, other important properties of coal, such as ash content and ash fusion temperature or even heating value that have complicated relation to elemental composition, are determined on the basis of LIBS spectra using multivariate analysis methods [3–5]. Contrary to numerous studies dealing with LIBS diagnostic of coals and lignite, the number of papers related to LIBS diagnostics of oil shale is rather limited.

In [6, 7], laser-induced pyrolysis was used for determination of oil shale characteristics. Directing a number of laser shots with high repetition rate to the same spot of the sample under an argon purge, the changes in the spectral line intensities in LIBS spectra over the course of measurements were related to H/C ratios determined on isolated kerogens from the rock samples. Predicted kerogen H/C ratios from the LIBS measurements of whole rock samples were well correlated ( $R^2 = 0.99$ ) to values determined for kerogen isolates measured by elemental analysis [6]. An important advantage of the method is that the decay of intensities of H and C lines with the growth of laser shot number allowed a clear

TABLE 1: Composition of dry samples.

Sample number	1	2	3	4	5	6	7	8	9	10
Heating value by bomb, $Q^b$ (MJ/kg)	6.36	6.60	7.28	7.98	9.10	9.08	9.86	10.36	10.78	11.62
Analytical moisture (%)	0.6	0.6	0.7	0.7	0.8	0.8	0.8	0.8	0.8	0.8
C (%)	22.4	22.3	23.4	24.3	26.4	26.4	27.2	27.8	29.5	30.9
C inorganic (%)	7.2	7.2	6.9	6.6	6.1	6.3	5.6	5.1	5.8	5.6
C organic (%)	15.2	15.1	16.5	17.7	20.3	20.1	21.6	22.7	23.7	25.3
S (%)	1.0	1.2	1.2	1.3	1.4	1.4	1.3	1.5	1.2	1.3
N (%)	0.07	0.07	0.07	0.08	0.08	0.08	0.09	0.1	0.09	0.09
H (%)	1.9	1.9	2.1	2.2	2.6	2.6	2.7	3.0	2.9	3.0
$Fe_2O_3$ (%)	2.0	1.9	2.1	2.2	2.3	2.5	2.2	2.5	2.1	1.9
$SiO_2$ (%)	11.2	10.1	10.8	11.1	13.0	13.3	15.9	16.6	12.7	12.2
MgO (%)	3.2	3.1	2.1	3.0	3.2	3.5	2.8	2.7	2.8	2.7
CaO (%)	32.9	32.1	31.2	26.4	27.7	32.1	26.6	22.7	31.6	30.4
$K_2O$ (%)	1.5	2.2	2.2	3.8	3.6	1.7	1.7	1.4	2.9	1.4
$Al_2O_3$ (%)	1.9	2.4	3.6	3.7	3.5	3.0	2.6	2.9	3.4	2.4
$Na_2O$ (%)	4.4	5.4	8.6	8.2	4.3	5.6	1.7	2.5	7.9	5.7

separation of H and C in the organic part of oil shale from that in the inorganic part. However, it is not realistic to apply the above-described laser-induced pyrolysis method for online monitoring of raw material on a running belt.

In [8], elemental composition of Marcellus Shale was determined with a high precision using LIBS spectra and multivariate analysis. However, for calculation of heating value on the basis of known elemental composition, additional information about the content of elements in the organic fraction is needed.

In [9], we applied LIBS diagnostics on Estonian oil shale samples for testing the moisture-caused matrix effects. The mineral and elemental composition of tested oil shale and waste rock (kerogenic limestone) samples were very similar, except the low percentage of organics in waste rock. Changes of both, content of kerogen and content of moisture, had strong effect on intensities of analytical spectral lines. A proper choice of spectral lines allowed reliable distinction of oil shale and limestone independently of moisture content.

The oil shale chemical composition and physical properties differ significantly from those of coal and lignite. The oil shale heating value is correlated with the concentrations of elements C, H, O, S, N, and Cl in the organic fraction of oil shale [10]. However, these elements are also present in large quantities in inorganic fraction of oil shale. Besides, as it is shown in [10], calculation of heating value using only elemental composition did not work well for Estonian oil shale. Mendeleev's and Dulong's formulae are widely used and accepted for calculation of heating value on the basis of elemental composition of organic part of many solid fuels, but situation with Estonian oil shale is more complicated than the applications for which these formulae were intended. "There is also the possibility that describing the heat of formation of a solid fuel using only elemental composition (as is inherent in all these methods) simply does not work quite as well for oil shale organics as for other organics" [10]. These reasons could complicate also the oil shale

diagnostics by LIBS. Furthermore, elements belonging to surrounding air constituents cause an extra interference to LIBS spectra. According to the best of our knowledge, no investigation has been done to clarify the feasibility of LIBS for online determination of oil shale heating value.

The main aim of the present study was the evaluation of the LIBS applicability for determination of the heating value of Estonian oil shale using statistical methods of data processing. As an extra task, the LIBS-based estimation of the oil shale chemical composition was done. Experiments were done in conditions close to real industrial conditions: measurements were done in ambient air and spectra were recorded from different spots at the moving/rotating pellet surface.

## 2. Experimental

**2.1. Samples.** 10 samples of ground oil shale with different heating values were prepared by the laboratory of Mines of Estonian Energy. The samples represent commercial oil shale from concentration plant with heating value ranging from 6.3 to 11.6 MJ/kg. Samples, each about 1 kg, had grain size below 0.1 mm. The heating value  $Q^b$  and the mass percentage of the main composites of samples (Table 1) were determined in the laboratory of Virumaa College of Tallinn University of Technology using standardised methods. Concentration of C, H, and N was determined according to Standard Test Methods for Determination of Carbon, Hydrogen, and Nitrogen in Analysis Samples of Coal ASTM D5373; MgO, CaO, and  $Al_2O_3$  according to EVN-EN ISO 7980; and  $K_2O$  and  $Na_2O$  according to ISO 9964.

About 200 g of each sample was additionally grinded using mortar and pestle to particle size smaller than 60  $\mu$ m (i.e., 10 times smaller than the laser spot diameter) assuring sample homogeneity for different laser shots [11, 12]. Samples were pelletised without any binder, whereas before pressing 5 wt% of distilled water was added to the room dry

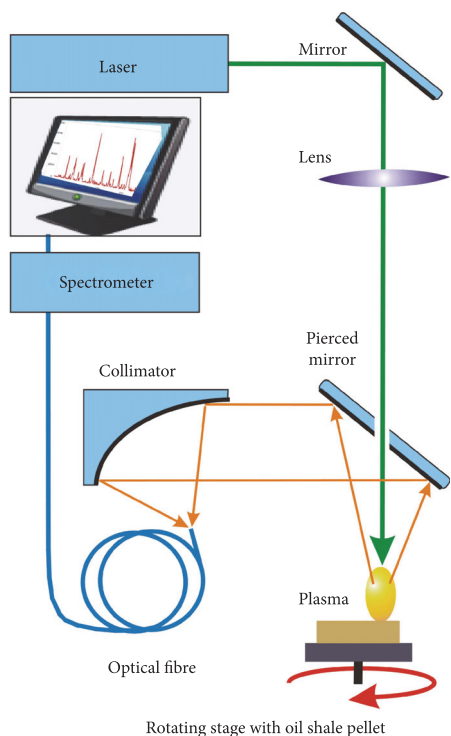


FIGURE 1: Sketch of the setup of measurements. Q-switched Nd:YAG laser YG980 and spectrometer Mechelle5000 were used.

powders. Powders were pressed into 25 mm in diameter and approximately 6 mm thick pellets under 18 tons held for 5 min. Four pellets from each sample were pressed. Thus, altogether 40 pellets were prepared. These pellets were stored in lab conditions at room temperature 21°C and relative humidity about 30% during a week to balance the moisture content of samples with the humidity of ambient air resulting approximately in about 2 wt% of moisture in pellets.

**2.2. LIBS Measurements.** A sketch of the laboratory LIBS setup is presented in Figure 1. The frequency-doubled Nd:YAG (YG980 Quantel) laser pulse of 532 nm wavelength and of 9 ns FWHM was focused onto the pellet surface with a plano-convex lens of 40 cm focal length in air. The focal plane of the lens was set about 3 cm under the samples' surface to avoid air breakdown in the focal point. The laser spot diameter at the sample surface was about 0.6 mm. The laser pulse energy at the plane of sample was measured with the pyroelectric laser energy meter Ophir Nova II. The pulse energy was set to 75 mJ making fluence at the pellet surface about 27 J/cm<sup>2</sup>. The plasma emission was collected collinearly along the laser beam axis with the off-axis parabolic mirror collimator CC52 (Andor Technology) with focal length of 52 mm and delivered via the optical fibre of 50 μm diameter to the Mechelle5000 (Andor Technology) spectrometer equipped with an intensified charge-coupled device

(ICCD) camera (Andor iStar DH334T-18F-03). The spectrum in 220–850 nm range with  $\lambda/\Delta\lambda = 5000$  resolution was recorded. The delay time  $t_d = 800$  ns between the laser pulse and the beginning of data acquisition was used. The recording time-gate  $\Delta t$  was 1 μs. These timing parameters were optimal for the signal-to-background ratio for carbon (C I) line at the wavelength 247.8 nm. Samples were fastened on a rotating stage driven with stepper motor supplying a fresh sample surface to each successive laser pulse avoiding possible pyrolysis-caused effects to the recorded spectra. The repetition rate of laser pulses was 0.55 Hz and the distance between the consecutive laser spots was more than 3 mm. Measurements were carried out under ambient atmospheric conditions. A continuous airflow of about 3 m/s was provided above the sample to remove laser-produced aerosols and dust between laser pulses [13]. To suppress the effect of possible sample heterogeneity, each pellet was characterised by a sum of 100 spectra. The relative standard deviation (RSD) of the shot-to-shot fluctuations of laser energy was 0.03.

### 3. Data Processing and Results

**3.1. Selection of Spectral Lines.** More than a hundred emission lines belonging to 12 major elements in oil shale (C, N, H, Fe, Mg, Si, Ca, K, Al, Na, Li, and Ti) were identified in recorded spectra using NIST atomic spectra database [14]. Spectral lines strongly overlapping with neighbouring lines and those with known strong self-absorption such as Ca II lines at 393.4 and 396.8 nm were removed from further analysis after preliminary investigations.

The heating value of oil shale is determined mainly by its kerogen concentration. It is known that carbon and hydrogen are the main constituent elements of kerogen [15]. In 220–850 nm spectral range, the only reliably detectable carbon line was the one at 247.8 nm. In [16, 17], molecular compounds C<sub>2</sub> and CN formed in the plasma plume were additionally used for carbon detection. Due to strong overlapping by other spectral lines, in our case, the usage of these bands was infeasible. Segments of oil shale LIBS spectra containing carbon line at 247.8 nm and hydrogen line at 656.3 nm are presented in Figure 2.

Integral intensity of a spectral line was characterised by a sum of counts belonging to pixels which cover approximately the half-width of the line (Figure 2(a)). For most of the spectral lines, the number of pixels,  $p$ , covering approximately the full width at half maximum (FWHM) comprises 9 pixels of the ICCD camera, whereas for H<sub>α</sub> line, which was strongly broadened by Stark effect, 60 pixels were used, and for whole triplet of O at 777 nm, 20 pixels were used. Usually, especially when recording with ungated detectors, for getting the actual spectral line intensities, the background should be subtracted. In the present study with gated camera and long enough delay time between the laser pulse and the recording gate, the background intensity was comparatively low. Besides, because of the presence of a number of overlapped low-intensity lines nearby some analytical lines, it was difficult to reliably measure the intensity of the background. As we checked (Section 3.4), the final result was not remarkably

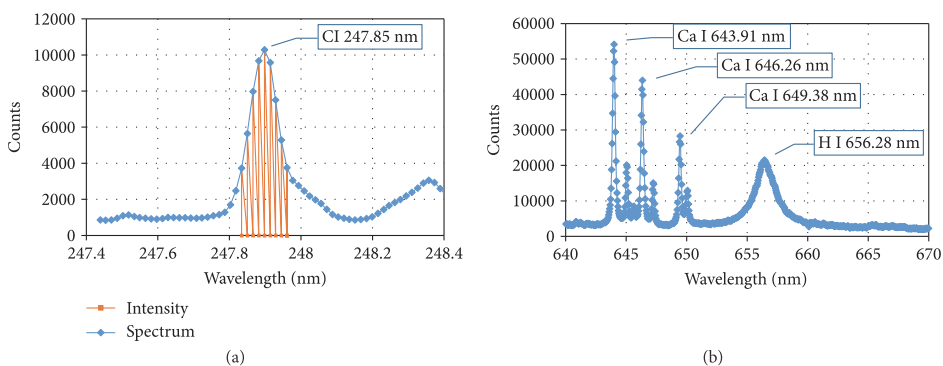


FIGURE 2: (a) A segment of the spectrum with carbon line (sample 1). (b) A segment with Ca and  $H_{\alpha}$  lines.

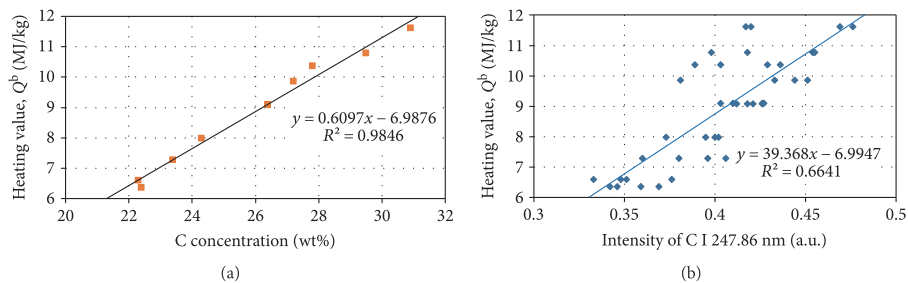


FIGURE 3: (a) Heating value of oil shale versus concentration of total C, data from Table 1. (b) Heating value as a function of the normalised intensity of C I line at 247.86 nm.

influenced by background subtraction and therefore we dropped this procedure.

Poor repeatability of LIBS signal is reported in many works [12, 18, 19]. Guidelines to reduce fluctuations of measured signals are reviewed in [12]. In case of oil shale, the chemical element with a constant concentration is missing and this is why the normalisation by internal standard [18] was not applicable.

In the present study, similarly to the papers [20–24], the role of laser pulse energy and plasma fluctuations was diminished by normalising the line intensity with the total intensity recorded between 220 and 850 nm.

Figure 3(a) based on Table 1 shows a high correlation coefficient  $R^2 = 0.9846$  between the mass fraction of total carbon and the heating value. At the same time, the LIBS measurements gave a correlation coefficient between the carbon line intensity and heating value only  $R^2 = 0.664$  (Figure 3(b)).

Similarly, the correlation coefficients between the line intensities and the heating values were found for all identified spectral lines. Calculated correlation coefficients between the heating value and normalised intensities of 43 preselected lines are presented in Figure 4. Lines of low absolute value of the correlation coefficient and lines having low signal-to-background ratio were excluded from further usage.

As one can see in Figure 4, the maximum value of correlation coefficient  $R = 0.861$  belongs to H line. Absolute values

for most of spectral lines of these correlation coefficients are less than 0.6. Since Ca and Mg lines represent mostly carbonates of waste rock, the values of correlation coefficients for Ca I, Ca II, and Mg I lines are negative. Indeed, the higher percentage of waste rock leads to a lower heating value.

It is known that one reason for the low values of correlation coefficients is matrix effect [25]. Low-value correlation coefficients indicate that the prediction of heating value by only a single spectral line intensity will have low accuracy. The use of multivariate analysis helps to minimise the matrix effect of complex geochemical materials and increase the accuracy of prediction [20, 26].

**3.2. Multivariate Linear Regression Model.** We assumed that the heating value of an oil shale sample could be expressed as a linear combination of intensities of measured spectral lines like it was done for lignite and coal [5, 27]:

$$Q = \mathbf{X} \cdot \mathbf{I}. \quad (1)$$

Here,  $Q$  denotes the heating value of a sample, vector  $\mathbf{I}$  elements  $I_n$  are intensities of spectral lines, and vector  $\mathbf{X}$  elements  $x_n$  are coefficients which values must be estimated in the course of calibration. The index  $n$  has values  $0, \dots, N$  where  $N$  is the number of spectral lines chosen for calibration.

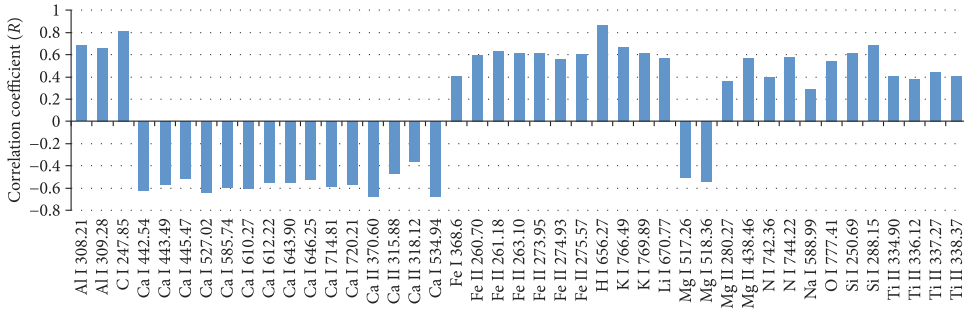


FIGURE 4: Correlation coefficients between normalised spectral line intensity and heating value.

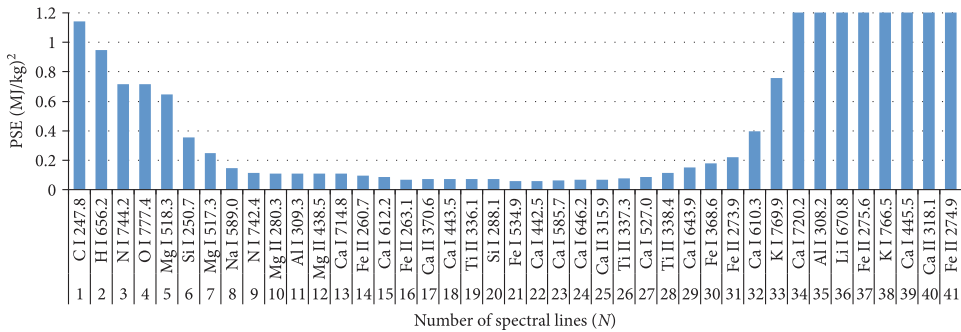


FIGURE 5: Predictive square error as a function of number of used spectral lines (N).

Coefficients of  $\mathbf{X}$  were calculated according to the ordinary least square regression [12, 28] as

$$\mathbf{X} = (\mathbf{A}^T \cdot \mathbf{A})^{-1} \cdot \mathbf{A}^T \cdot \mathbf{B}, \quad (2)$$

where  $\mathbf{A}$  is a  $M \times N$  matrix which elements  $I_{m,n}$  are normalised intensities of spectral lines obtained in the course of calibration and  $M$  is the number of pellets used for calibration.  $\mathbf{B}$  is a  $M$  element vector which elements are heating values determined by calorimetric bomb method (Table 1) for samples used for calibration. Superscript  $T$  denotes the transposed matrix.

**3.3. Cross-Validation.** The leave-one-out (LOO) cross-validation method [29–32] was used to find out the optimal set of spectral lines and to estimate the regression model predictivity. We used spectra of 36 pellets with nine different heating values for calibration, and for testing, we left out a subset of spectra of four pellets of the same sample having the known heating value from calorimetric measurements. This procedure was repeated leaving out one by one each of 4-pellet subsets of 10 samples.

The predictive square error (PSE) was used to evaluate the predictivity of the model:

$$\text{PSE} = \frac{1}{K} \sum_{i=1}^K \left( Q_i^p - Q_i^b \right)^2. \quad (3)$$

Here  $Q_i^b$  denotes the heating value of the  $i$ th pellet measured with bomb calorimeter (Table 1) and  $Q_i^p$  is calculated using relationships (1) and (2), whereby the  $i$ th spectrum is left out from the calibration set.  $K$  is the number of pellets tested ( $K = 40$ ).

As the first step, PSE was calculated using only the C line for calculation of the heating value. The C line was selected because the carbon concentration is directly related to the heating value (Figure 3(a)).  $H_\alpha$  line intensity correlation with the heating value is even higher than that of C line (see Figure 4), but  $H_\alpha$  line intensity has also a strong correlation with the moisture content [33]. The next step was the calculation of the heating value and PSE using additionally to the C I line one of the remaining 42 preselected lines (Figure 4). This step was repeated 42 times using one by one all remaining lines. A two-line combination with the minimal value of PSE was selected and the procedure of seeking the minimal value of PSE was repeated for combinations of 3 lines, two of them being selected from the previous step. Increasing step by step the number of lines, the minimal PSE at a certain number of lines was obtained. The dependence of minimal PSE on the number of involved lines is presented in Figure 5.

As one can see in Figure 5, the initial fast decrease of the PSE value continues until  $N$  reaches the value of about 10. Intensities of the first two lines, C and  $H_\alpha$ , in the succession of spectral lines in Figure 5 have the highest value of correlation with the heating value (Figure 4). The presence of O, Mg,

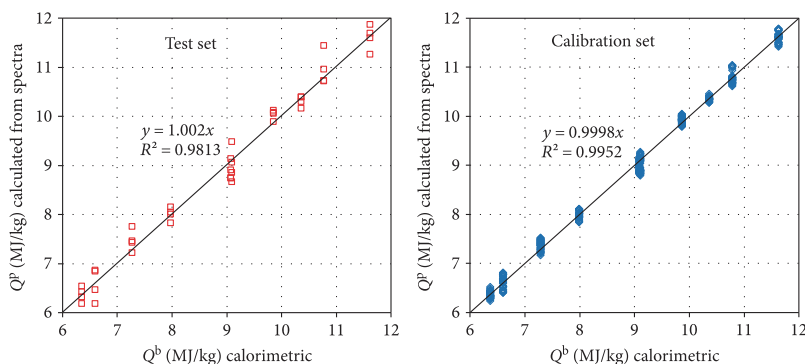


FIGURE 6: Heating value of oil shale  $Q^p$  determined by LIBS versus calorimetric heating value  $Q^b$ . Solid lines are linear fits for data points, whereby the intercept is set to zero.

Si, Na, Ca, and Al in the initial part of progression of lines with fast decrease of PSE is also expectable as they belong to compounds presented in oil shale in relatively large quantities (Table 1, composition of samples). However, the presence of nitrogen lines there is somewhat surprising as the nitrogen content in the oil shale is very low. At the same time, nitrogen is the main component of the ambient air and its presence in the initial part of sequence could be related to the air breakdown on the surface of the samples as proposed by [34]. PSE in Figure 5 has its minimum value,  $PSE_{\min} = 0.056$ , at  $N_{\min} = 21$ . Fast growth of PSE up to very high values takes place when  $N$  becomes close to the number of pellets used for calibration which is a common behaviour for ordinary least square regression.

The heating value predicted by the set of first 21 lines in Figure 5 is presented in Figure 6.

The value of the correlation coefficient,  $R^2 = 0.981$ , between the heating value  $Q^p$  predicted by LIBS and the calorimetric heating value  $Q^b$ , is close to the correlation coefficient between  $Q^b$  and the total carbon content of oil shale (Figure 3(a)).

Figure 7 presents the distribution of the difference between the “true” heating value and the heating value predicted by LIBS:  $\Delta Q = Q^b - Q^p$  for the test set.

Achieved standard deviation value  $SD = 0.24$  MJ/kg differs from the uncertainty  $0.13$  MJ/kg of the calorimetric measurements only by a factor of two. According to Figure 5, near the vicinity of the  $PSE_{\min}$ , the value of PSE depends weakly on  $N$ . Indeed, using instead of 21 lines only the first 10 lines, gives for  $SD = 0.33$  MJ/kg and  $R^2 = 0.963$ .

**3.4. Effect of Initial Data Variation.** We tested the effect of the preselection of spectral lines as well as the procedure of the determination of integral intensity of spectral lines on the final results. Both the succession of lines and the number of spectral lines  $N_{\min}$  resulting to the minimum of PSE value (Figure 5)  $PSE_{\min}$  depended on those factors. The succession changed when for determination of line intensities, the background was taken into account, or the number of pixels,  $p$ , which was considered for integral

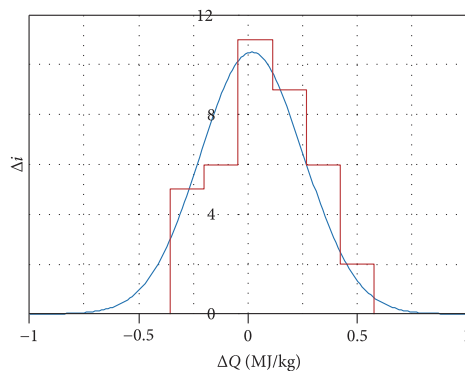


FIGURE 7: Histogram of  $\Delta Q = Q^b - Q^p$ . Solid line—Gaussian fit for data points. The width of Gaussian curve (standard deviation (SD)) is  $0.24$  MJ/kg.

intensity determination was varied. Similarly, the succession of lines altered with the variation in the list of preselected lines. Different successions gave a little bit different values of  $PSE_{\min}$ . Figure 8 shows how the value of  $PSE_{\min}$  and  $N_{\min}$  depend on the used numbers of pixels,  $p$ . For most of lines, the value of  $p$  was varied from 3 to 15. For wide lines O at  $777$  nm and H at  $656$  nm, the number of pixels remained unchanged.

$PSE_{\min}$  and  $N_{\min}$  as a function of  $p$  was calculated for two preselections, one of them containing 54 lines, and another, being the subset of the first one, containing 43 lines (Figure 8). For both cases, intensity of lines was calculated with and without subtraction of the background. The background for each line was determined as the lowest intensity in spectral region 50 pixels left and right from the line.

Figure 8 demonstrates that in the case of 54 preselected lines,  $PSE_{\min}$  is always below  $0.1$  (MJ/kg)<sup>2</sup>, and in the case of 43 lines,  $PSE_{\min}$  is below  $0.15$  (MJ/kg)<sup>2</sup>. Variations of  $PSE_{\min}$  and  $N_{\min}$  with  $p$  seem to have a random character.

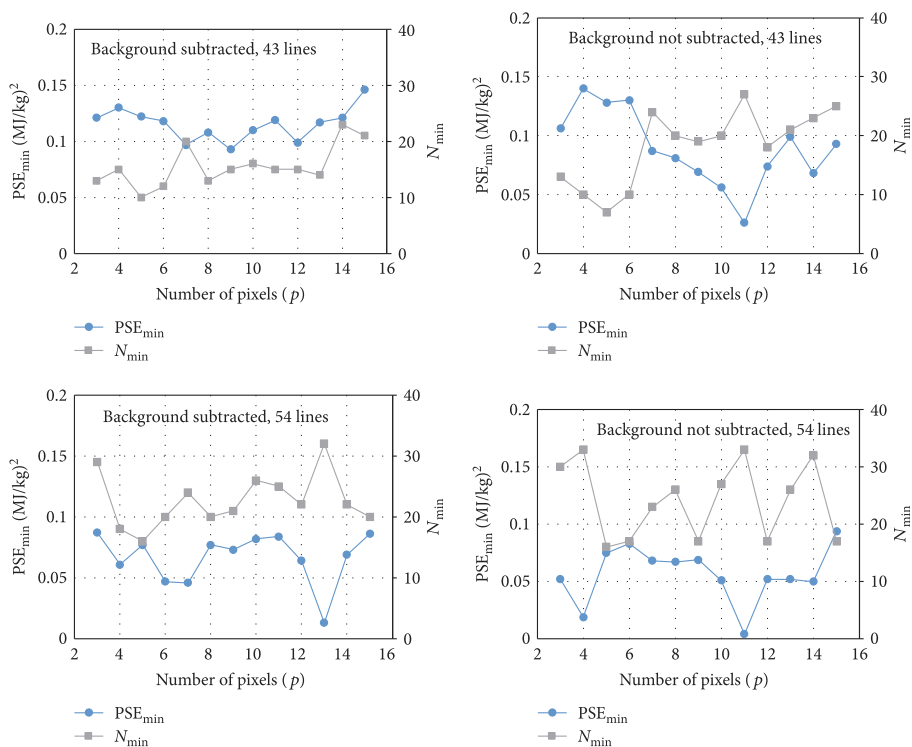


FIGURE 8:  $PSE_{\min}$ : minimum value of PSE as a function of number of pixels accounted for determination of integral intensities;  $N_{\min}$ : value of  $N$  at minimum PSE.

The shape of  $PSE = f(N)$  curves was independent of choice of  $p$  and stayed similar to that in Figure 5. The initial fast decrease of the PSE took place until  $N \approx 10$  followed by much slower decrease until  $N_{\min}$ . When  $N$  became close to the number of pellets used for calibration, a fast increase of PSE started.  $N_{\min}$  was below 35 in the case of 54 lines, and below 25 for 43 lines.

Like in Figure 5, when the background was not subtracted, lines of C, O, Si, Mg, H, and N were always present within the first ten lines of the succession. When the background was subtracted, the H line was not always in the list of the first ten lines.

Results presented in Sections 3.3 and 3.5 are obtained under the following conditions:

- (i)  $p=9$  because this number of pixels corresponded best to the full width at half maximum of most of spectral lines.
- (ii) The background was not subtracted, because the determination of real value of background was complicated.
- (iii) We use the preselection of 43 lines because the calculations are less time consuming.

TABLE 2: RSD and  $R^2$  for ingredients of oil shale.

	RSD	$R^2$
C	0.015	0.982
N	0.016	0.984
H	0.027	0.973
CaO	0.03	0.933
SiO <sub>2</sub>	0.031	0.964
Fe <sub>2</sub> O <sub>3</sub>	0.049	0.729
MgO	0.136	0.281
Al <sub>2</sub> O <sub>3</sub>	0.137	0.629
Na <sub>2</sub> O	0.251	0.691
K <sub>2</sub> O	0.296	0.533
S	0.041	0.869

However, as Figure 8 shows, most of tested values for  $p$  and other tested factors give a satisfactory ( $PSE_{\min} < 0.1$ ) results as well.

**3.5. Prediction of Ingredients Concentrations.** The procedure of the ordinary least square regression applied for prediction of the heating value was applied also to predict the

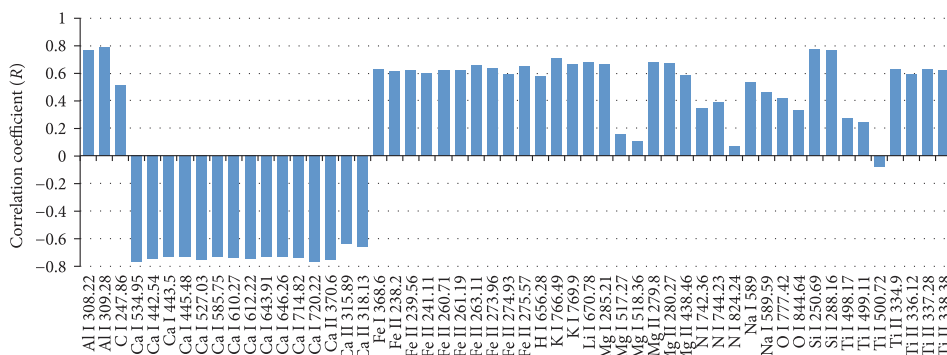


FIGURE 9: Correlation of spectral line intensity with concentration of sulphur.

concentration of the ingredients determined at the laboratory of Virumaa College of Tallinn University of Technology (Table 1). The only change introduced to the method described above was the replacing in relationships (1) and (3) the heating value,  $Q$ , by the concentration of a component and finding by (2) the set of coefficients which corresponds to this component. For each of the oil shale constituents determined in the laboratory, the set of spectral lines giving minimum of PSE was determined and the relative standard deviation (RSD) of prediction and correlation coefficient ( $R^2$ ) between prediction by LIBS and laboratory measured data were calculated. Values of RSD and  $R^2$  are presented in Table 2.

The minimum RSD=1.5% was obtained for the total carbon. The highest values of RSD were found for constituents containing Na, K, and Al. The likely reason is that these elements were characterised by resonant lines which have a strong self-absorption [35] and as a result, the intensity of these lines is not a linear function of element concentration.

Strong sulphur lines at 921.3, 922.8, and 923.8 nm were out the wavelength range of our spectrometer. However, intensities of spectral lines of other elements are correlated with the sulphur concentration determined at the laboratory. According to Figure 9, a number of lines have values of the correlation coefficient  $R=0.6-0.8$ . This indicates that the presence of sulphur influences spectral line intensities of other elements. By our opinion, this influence can be attributed to the matrix effect. It was possible to predict the sulphur concentration on the basis of other lines (Figure 10) with  $RSD_S=4.1\%$ .

#### 4. Conclusions

The study showed that LIBS diagnostics gives reliable results for oil shale heating value in laboratory conditions using homogenised pellets of samples.

The most important results are as follows:

(i) The multivariate linear regression is applicable for determination of the oil shale heating value. The

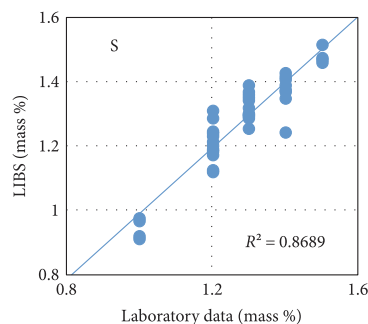


FIGURE 10: Sulphur content determined by LIBS versus laboratory data. Solid line is a linear fit for data points.

used method of selection of spectral lines enables to find out minimal number of spectral lines needed for determination of the heating value and concentrations of constituents with an acceptable accuracy.

- (ii) The root mean square error of predicted heating value of commercial oil shale was 0.24 MJ/kg. This value is comparable with uncertainty of determination of heating value with calorimetric bomb (0.13 MJ/kg).
- (iii) The method allows to determine the dominating constituents of oil shale (C, H, CaO, SiO<sub>2</sub>, and Fe<sub>2</sub>O<sub>3</sub>) with the value of relative standard deviation < 5%.
- (iv) Determination of sulphur concentration is possible using a proper statistical model for description of relation between LIBS spectrum and sample composition.

#### Conflicts of Interest

The authors declare that they have no conflicts of interest.

## Acknowledgments

This work was financially supported by Environmental Investment Centre of Estonia (Project no. 7594).

## References

- [1] I. Valgma, E. Reinsalu, S. Sabanov, and V. Karu, "Quality control of oil shale production in Estonian mines," *Oil Shale*, vol. 27, no. 3, pp. 239–249, 2010.
- [2] C. E. Romero and R. De Saro, "LIBS analysis for coal," in *Laser-Induced Breakdown Spectroscopy*, S. Musazzi and U. Perini, Eds., vol. 182 of Springer Series in Optical Sciences, Springer, Berlin, Heidelberg, 2014.
- [3] S. Yao, J. Lu, M. Dong, K. Chen, J. Li, and J. Li, "Extracting coal ash content from laser-induced breakdown spectroscopy (LIBS) spectra by multivariate analysis," *Applied Spectroscopy*, vol. 65, no. 10, pp. 1197–1201, 2011.
- [4] J. Craparo, R. De Saro, C. Romero, Z. Yao, A. Whitehouse, and A. Weisberg, "Measuring thermal properties of coal with a commercial bench top LIBS system," in *Applied Industrial Optics: Spectroscopy, Imaging and Metrology 2012*, pp. 4–6, Monterey, California United States, 2012.
- [5] T. Yuan, Z. Wang, S.-L. Lui et al., "Coal property analysis using laser-induced breakdown spectroscopy," *Journal of Analytical Atomic Spectrometry*, vol. 28, no. 7, p. 1045, 2013.
- [6] J. E. Birdwell and K. E. Washburn, "Rapid analysis of kerogen hydrogen-to-carbon ratios in shale and mudrocks by laser-induced breakdown spectroscopy," *Energy and Fuels*, vol. 29, no. 11, pp. 6999–7004, 2015.
- [7] K. E. Washburn, "Rapid geochemical and mineralogical characterization of shale by laser-induced breakdown spectroscopy," *Organic Geochemistry*, vol. 83–84, pp. 114–117, 2015.
- [8] H. K. Sanghvi, J. Jain, A. Bol'Shakov, C. Lopano, D. McIntyre, and R. Russo, "Determination of elemental composition of shale rocks by laser induced breakdown spectroscopy," *Spectrochimica Acta Part B: Atomic Spectroscopy*, vol. 122, pp. 9–14, 2016.
- [9] P. Paris, K. Piip, A. Lepp, A. Lissovski, M. Aints, and M. Laan, "Discrimination of moist oil shale and limestone using laser induced breakdown spectroscopy," *Spectrochimica Acta Part B: Atomic Spectroscopy*, vol. 107, pp. 61–66, 2015.
- [10] H. Arro, A. Prikk, and T. Pihu, "Calculation of qualitative and quantitative composition of Estonian oil shale and its combustion products," *Fuel*, vol. 82, no. 18, pp. 2179–2195, 2003.
- [11] R. B. Anderson, R. V. Morris, S. M. Clegg et al., "The influence of multivariate analysis methods and target grain size on the accuracy of remote quantitative chemical analysis of rocks using laser induced breakdown spectroscopy," *Icarus*, vol. 215, no. 2, pp. 608–627, 2011.
- [12] E. Tognoni and G. Cristoforetti, "[Invited] Signal and noise in laser induced breakdown spectroscopy: an introductory review," *Optics & Laser Technology*, vol. 79, pp. 164–172, 2016.
- [13] R. Wisbrun, I. Schechter, R. Niessner, H. Schroder, and K. L. Kompa, "Detector for trace elemental analysis of solid environmental-samples by laser-plasma spectroscopy," *Analytical Chemistry*, vol. 66, no. 18, pp. 2964–2975, 1994.
- [14] A. Kramida, Y. Ralchenko, J. Reader, and NIST ASD Team, *NIST Atomic Spectra Database (Ver. 5.2)*, National Institute of Standards and Technology (NIST), Gaithersburg, MD, 2013.
- [15] U. Lille, I. Heinmaa, and T. Pehk, "Molecular model of Estonian kukersite kerogen evaluated by C-13 MAS NMR spectra," *Fuel*, vol. 82, no. 7, pp. 799–804, 2003.
- [16] M. Dong, X. Mao, J. J. Gonzalez, J. Lu, and R. E. Russo, "Time-resolved LIBS of atomic and molecular carbon from coal in air, argon and helium," *Journal of Analytical Atomic Spectrometry*, vol. 27, pp. 2066–2075, 2012.
- [17] X. Li, H. Yin, Z. Wang, Y. Fu, Z. Li, and W. Ni, "Quantitative carbon analysis in coal by combining data processing and spatial confinement in laser-induced breakdown spectroscopy," *Spectrochimica Acta Part B: Atomic Spectroscopy*, vol. 111, pp. 102–107, 2015.
- [18] D. Diaz, D. W. Hahn, and A. Molina, "Evaluation of laser-induced breakdown spectroscopy (LIBS) as a measurement technique for evaluation of total elemental concentration in soils," *Applied Spectroscopy*, vol. 66, no. 1, pp. 99–106, 2012.
- [19] J. M. Mermet, P. Mauchien, and J. L. Lacour, "Processing of shot-to-shot raw data to improve precision in laser-induced breakdown spectrometry microprobe," *Spectrochimica Acta Part B: Atomic Spectroscopy*, vol. 63, no. 10, pp. 999–1005, 2008.
- [20] J. B. Sirven, B. Bousquet, L. Canioni, and L. Sarger, "Laser-induced breakdown spectroscopy of composite samples: comparison of advanced chemometrics methods," *Analytical Chemistry*, vol. 78, no. 5, pp. 1462–1469, 2006.
- [21] B. Bousquet, J. B. Sirven, and L. Canioni, "Towards quantitative laser-induced breakdown spectroscopy analysis of soil samples," *Spectrochimica Acta Part B: Atomic Spectroscopy*, vol. 62, no. 12, pp. 1582–1589, 2007.
- [22] J. Feng, Z. Wang, Z. Li, and W. Ni, "Study to reduce laser-induced breakdown spectroscopy measurement uncertainty using plasma characteristic parameters," *Spectrochimica Acta Part B: Atomic Spectroscopy*, vol. 65, no. 7, pp. 549–556, 2010.
- [23] A. Ciucci, M. Corsi, V. Palleschi, S. Rastelli, A. Salvetti, and E. Tognoni, "New procedure for quantitative elemental analysis by laser-induced plasma spectroscopy," *Applied Spectroscopy*, vol. 53, no. 8, pp. 960–964, 1999.
- [24] D. Body and B. L. U. Chadwick, "Optimization of the spectral data processing in a LIBS simultaneous elemental analysis system," *Spectrochimica Acta Part B: Atomic Spectroscopy*, vol. 56, no. 6, pp. 725–736, 2001.
- [25] A. S. Eppler, D. A. Cremers, D. D. Hickmott, M. J. Ferris, and A. C. Koskelo, "Matrix effects in the detection of Pb and Ba in soils using laser-induced breakdown spectroscopy," *Applied Spectroscopy*, vol. 50, no. 9, pp. 1175–1181, 1996.
- [26] J. M. Tucker, M. D. Dyar, M. W. Schaefer, S. M. Clegg, and R. C. Wiens, "Optimization of laser-induced breakdown spectroscopy for rapid geochemical analysis," *Chemical Geology*, vol. 277, no. 1–2, pp. 137–148, 2010.
- [27] J. Feng, Z. Wang, L. West, Z. Li, and W. Ni, "A PLS model based on dominant factor for coal analysis using laser-induced breakdown spectroscopy," *Analytical and Bioanalytical Chemistry*, vol. 400, no. 10, pp. 3261–3271, 2011.
- [28] H. Martens and T. Naes, *Multivariate calibration*, John Wiley & Sons, Chichester, 2014.
- [29] M. Shahlai, "Descriptor selection methods in quantitative structure – activity relationship studies: a review study," *Chemical Reviews*, vol. 113, no. 10, pp. 8093–8103, 2013.
- [30] P. Filzmoser, B. Liebmann, and K. Varmuza, "Repeated double cross validation," *Journal of Chemometrics*, vol. 23, no. 4, pp. 160–171, 2009.

- [31] M. Forina, S. Lanteri, and M. Casale, "Multivariate calibration," *Journal of Chromatography A*, vol. 1158, no. 1-2, pp. 61–93, 2007.
- [32] J. El Haddad, L. Canoni, and B. Bousquet, "Good practices in LIBS analysis: review and advices," *Spectrochimica Acta Part B: Atomic Spectroscopy*, vol. 101, pp. 171–182, 2014.
- [33] Y. Zhao, L. Zhang, S.-X. Zhao et al., "Review of methodological and experimental LIBS techniques for coal analysis and their application in power plants in China," *Frontiers of Physics*, vol. 11, no. 6, article 114211, 2016.
- [34] L. Zhang, Z. Y. Hu, W. B. Yin et al., "Recent progress on laser-induced breakdown spectroscopy for the monitoring of coal quality and unburned carbon in fly ash," *Frontiers of Physics*, vol. 7, no. 6, pp. 690–700, 2012.
- [35] R. Yi, L. Guo, C. Li et al., "Investigation of the self-absorption effect using spatially resolved laser-induced breakdown spectroscopy," *Journal of Analytical Atomic Spectrometry*, vol. 31, no. 4, pp. 961–967, 2016.

## Appendix 2

### **Paper - P II**

Aints, M., Paris, P., Tufail, I., Jogi, I., Aosaar, H., Riisalu, H., & Laan, M. (2018). Determination of the calorific value and moisture content of crushed oil shale by LIBS. *Oil Shale*, 35(4), 339-355.



## DETERMINATION OF THE CALORIFIC VALUE AND MOISTURE CONTENT OF CRUSHED OIL SHALE BY LIBS

MÄRT AINTS<sup>(a)</sup>, PEETER PARIS<sup>(a)</sup>, IRAM TUFAIL<sup>(a,b)</sup>,  
INDREK JÕGI<sup>(a)</sup>, HARDI AOSAAR<sup>(c)</sup>, HELLA RIISALU<sup>(d)</sup>,  
MATTI LAAN<sup>(a)\*</sup>

<sup>(a)</sup> Institute of Physics, University of Tartu, Ostwaldi 1, 50411 Tartu, Estonia

<sup>(b)</sup> Department of Cybernetics, Tallinn University of Technology, Akadeemia tee 21, 12618 Tallinn, Estonia

<sup>(c)</sup> Eesti Energia AS, Lelle 22, 11318 Tallinn, Estonia

<sup>(d)</sup> Virumaa College, Tallinn University of Technology, Järveküla tee 75, 30322 Kohtla-Järve, Estonia

**Abstract.** *Laser-induced breakdown spectroscopy (LIBS) was used for the quantitative assessment of the calorific value of Estonian oil shale. Samples were collected from different layers of oil shale and limestone from Narva open cast mine, Estonia.*

*Lumps of crushed oil shale without any special preparation were tested on a mock-up of a moving conveyor belt. The moisture content of oil shale samples was varied. Multivariate regression analysis was applied for processing of spectroscopic data. The results obtained using the bomb calorimetric method were used for calibration. The method for selecting the optimal number of spectral lines for data processing is presented. The standard deviation of prediction of the calorific value was 1.76 MJ/kg and the moisture content was 1.94%.*

**Keywords:** *crushed oil shale, calorific value, moisture content, laser-induced breakdown spectroscopy.*

### 1. Introduction

Estonian oil shale is used for oil production [1] as well as a fuel in power plants [2]. Both the yield of oil and the efficiency of boilers depend on the organic and moisture content of raw material. At present the calorific value, which characterizes the oil shale organic content, is mostly measured using oxygen bomb calorimeters. The respective laboratory method is sufficiently precise but the periodic grab sampling and time-consuming laboratory

---

\* Corresponding author: e-mail [matti.laan@ut.ee](mailto:matti.laan@ut.ee)

testing could not meet the requirement of real-time control and optimization of industrial processes. Moreover, the calorific value of oil shale may vary considerably within a deposit [3] which in turn confirms the urgent need for a rapid on-line monitoring of the continuous flow of raw material.

Nowadays, industry uses three on-line methods for quality control. In coal industry, X-ray fluorescence (XRF) as well as prompt gamma neutron activation analysis (PGAA) have proven their efficiency and sufficient speed for continuous monitoring. The third method, laser-induced breakdown spectroscopy (LIBS), has also shown acceptable accuracy and precision. Besides, LIBS is safer and has lower installation and operating costs compared with the abovementioned two other methods [4].

LIBS is a method of emission spectroscopy where a pulse of the laser beam (laser shot) evaporates a small amount of the sample and a plasma plume forms at the sample surface. The plume emits light whose spectrum reflects the elemental composition of sample [5]. Application of LIBS for characterization of coals and lignite is the subject of many papers. An overview can be found, for example, in the paper by Romero and De Saro [6] and references therein. The LIBS testing was carried out in conditions which were close to those of the conveyer belt and the calibration curves for elements were built [7]. In addition to elemental composition, other important properties of coal, such as ash content, ash fusion temperature, or even calorific value, which has a complicated relation to elemental composition, are calculated on the basis of LIBS spectra using multivariate analysis methods [8–10].

As reported earlier, moisture content has a considerable impact on LIBS results, decreasing the intensity of spectral lines of most elements [11]. This dependence of LIBS spectra on moisture allows one to use the said analysis technology for the moisture content measurement as demonstrated in case of coal [10]. Thus, in principle, LIBS spectra can be used for the simultaneous determination of the calorific value and moisture content.

Contrary to numerous studies dealing with LIBS diagnostics of coals and lignite, papers related to the similar diagnostics of oil shale are rather few. LIBS-induced pyrolysis has been used for determination of oil shale characteristics [12, 13]. An important advantage of the method is that the decay of intensities of hydrogen (H) and carbon (C) lines with the growth of laser shot number allowed a clear separation of H and C present in the organic part of oil shale from its inorganic part. The elemental composition of Marcellus Shale was determined with a high precision using LIBS spectra coupled with multivariate analysis [14]. Aints et al. [15] investigated the applicability of LIBS for determination of the calorific value of Estonian oil shale. As an extra task, the LIBS-based estimation of the oil shale chemical composition was done. Air-dry pellets with different known calorific values pressed from homogenized powder (particle size < 60  $\mu\text{m}$ ) were tested. Measurements were done in ambient air and LIBS spectra were recorded from different spots at the rotating pellet surface. The study showed that

LIBS diagnostics in laboratory conditions combined with multivariate regression analysis gives reliable results for homogenized dry pellets. The root mean square error of calorific value prediction by LIBS was 0.24 MJ/kg. This value is comparable with the uncertainty of the calorific value determined using the ISO 1928:2009 bomb calorimetric method, 0.13 MJ/kg. Paris et al. [16] studied the qualitative effect of moisture on LIBS spectra of Estonian oil shale samples. It appeared that the moisture had a strong effect on these spectra, which complicated the distinction between oil shale and limestone.

The aim of the present paper was to evaluate the feasibility of using LIBS for determination of calorific value and moisture content in conditions comparable to industrial ones. Differently from previous studies, crushed oil shale without any special preparation was tested by LIBS on a mock-up of a moving conveyor belt. Besides, LIBS was used for the quantitative determination of the moisture content.

## 2. Samples

Samples for the study were collected by an exploration geologist from Narva open cast mine, Estonia, from layers A–F2 of the 7th trench's west-side exposure (outcrop). Altogether 11 samples from different oil shale layers and limestone interlayers were taken. Oil shale layers A, B and E of the mineable seam are the richest in organic matter, containing up to 60% kerogen. Other oil shale layers contain large- or small-scale limestone concretions [17]. The organic content of layers A' and F is the lowest, while interlayers A'/B, B/C, C/D and D/E consist mostly of barren limestone with minor kerogen content. A more detailed overview about the composition of Estonian oil shale and its stratification and layers in the deposit is provided by Ots [2].

In addition, four samples with different calorific values sorted by density in a floatation tank were taken from the stopped conveyor belt of the beneficiation plant of the Estonia underground mine. These samples are labelled EST.

The samples selected for this study covered the whole vertical extent of the currently mineable Estonian oil shale deposit and the main product ranges of the Estonia underground mine beneficiation plant.

All samples were crushed in a jaw crusher to a fraction of around 0–25 mm. The weight of individual samples varied from 2.5 to 7.7 kg. Each sample was divided into two equal parts. The laboratory of Virumaa College, Tallinn University of Technology, determined the calorific value of the samples by using the bomb calorimetric method (ISO 1928:2009). The calorific values  $Q^d$  of dry samples are presented in Table 1 in ascending order.

An about 0.5 kg portion of each sample was used for LIBS measurements. For variation of moisture content, the samples were placed in

**Table. Calorific value and moisture content of samples**

Sample		Calorific value (dry base) $Q^d$ , MJ/kg	Moisture content $W_w$ , %				
No	Layer index		W1	W2	W3	W4	W5
1	A'/B	0.503	11.3	9.7	8.2	6.9	2.8
2	C/D	0.721	9.6	7.4	5.9	5.6	1
3	D/E	1.811	10.3	8.8	6.2	5.7	2.1
4	B/C	2.32	10	8.3	5.9	5.5	1.7
5	EST Q = 1.5	3.055	10.1	8	5.6	5.2	2.7
6	F2	4.502	9.7	7.9	6.3	5.8	1.2
7	D	6.813	10.5	8.5	5.7	5.3	2.7
8	EST Q = 7	9.1	14.9	13.3	11.7	9.3	7.1
9	F1	9.493	10.6	8.6	6.3	6	4
10	EST Q = 8	10.064	16	13.9	12.1	8.6	8.5
11	E	12.616	11	9.3	7.4	5.3	3.8
12	EST Q = 11.4	12.758	9.2	7.7	5.5	4.5	0.8
13	A + A'	13.605	23.4	20.6	18.8	10.7	10
14	C	15.581	10.6	8.6	6.1	5.3	4
15	B	21.123	15.3	13.2	11.5	7.7	7.3

hermetic jars and distilled water of about 10% of a sample weight was pipetted to each jar. The moisture homogenization was achieved by stirring and keeping the samples in hermetic jars for one week.

Before LIBS measurements, each sample was weighed with an accuracy of 0.1 g to determine its moisture content by employing the oven-drying method [18]. The samples were weighed again after LIBS testing (see section 3 below). It appeared that even if the moisture content of the sample was the highest, its weight during LIBS measurements did not change more than 0.7%.

After this cycle of measurements, samples were dried in open air for 24 hours. The jars were then closed hermetically and kept for one week to homogenize the moisture content at a lower level. Before the next cycle of LIBS measurements, drier samples were weighed again. For each sample, LIBS measurements were carried out at five different values of moisture content. Presented in Table, the actual moisture content of the samples was determined after their final drying in an evacuated oven at 105 °C during about 24 hours until constant weight was achieved.

### 3. Set-up and procedure of LIBS measurements

A detailed description of the used experimental set-up is presented in the paper by Aints et al. [15]. A sketch of the LIBS set-up is shown in Fig. 1a. The laser pulse with a wavelength of 532 nm and a full width at half maximum of 9 ns was focused onto the sample with a plano-convex lens of a

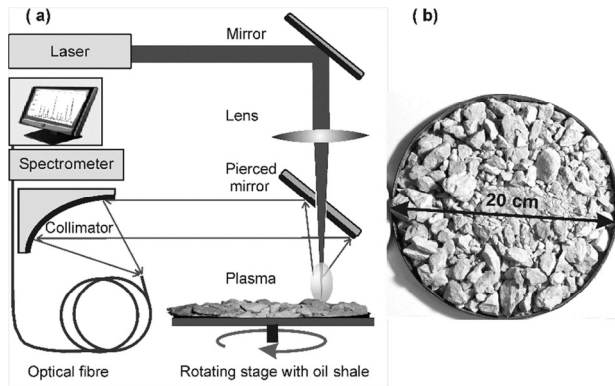


Fig. 1. (a) Sketch of the LIBS set-up; (b) crushed oil shale on the rotating stage, sample No 2.

focal length of 40 cm. The pulse energy was set to 100 mJ. The repetition rate of laser pulses was 0.55 Hz. The relative standard deviation, RSD, of the shot-to-shot fluctuations of the laser energy was 0.03.

Oil shale lumps of different size and orientation were spread out on the 20-cm-diameter rotating stage (Fig. 1b), which was driven by a stepper motor. The stage rotation speed, 8.57 1/min, was adjusted in a way that excluded the hitting by the laser beam the same spot on the sample twice during 100 consecutive pulses. Measurements were carried out in an air-conditioned room at a temperature of 22 °C and the relative humidity of 26%. To suppress the effect of laser-produced aerosols and dust [19], a blast draft of air of about 3 m/s was blown above the sample surface.

The emission of the laser-produced plasma was collected collinearly along the laser beam axis with the off-axis parabolic mirror collimator with a focal length of 52 mm and delivered via the optical fibre of a diameter of 50  $\mu\text{m}$  to the Mechelle 5000 spectrometer (Andor Technology), with a resolution of  $\lambda/\Delta\lambda = 5000$ . The spectrometer was equipped with an intensified charge coupled device Andor iStar. During a single laser shot this device recorded the spectrum in the 220–850 nm range (single shot spectrum). Time-gated LIBS spectra were recorded with data acquisition time  $\Delta t = 1 \mu\text{s}$  [5]. The delay time  $t_d = 800 \text{ ns}$  between the laser pulse and the opening of the gate for data acquisition was used. These timing parameters provided an optimal signal-to-noise ratio for the carbon line at the wavelength of 247.8 nm which had the highest coefficient of correlation with the oil shale calorific value in the spectral range used [15]. In addition to the carbon line, we selected 44 most representative spectral lines belonging to 12 major elements in oil shale (C, N, H, Fe, Mg, Si, Ca, K, Al, Na, Li, Ti). Each spectral line was characterised by the integral intensity  $I_\lambda = \int_{\Delta\lambda} I_{\lambda'} d\lambda'$  which was found as a sum of counts of pixels in the region,

$\Delta\lambda$  covering approximately the half-width of the line. Details of the half-width choice are presented by Aints et al. [15]. Besides intensities  $I_\lambda$ , the LIBS recordings were characterised by the total intensity  $I_T$ , which is the sum of counts over all pixels in the 220–850 nm spectral range. Both  $I_\lambda$  and  $I_T$  fluctuated remarkably from laser shot to shot. These fluctuations could be largely caused by the heterogeneity of the oil shale samples composition as well as by the random orientation of the lumps surface on the rotating stage. Fluctuations of both  $I_\lambda$  and  $I_T$  for crushed samples were larger than those obtained for specially prepared pellet samples where the laser hit the pellet surface perpendicularly [15]. The averaged LIBS characteristics of the sample were obtained, accumulating 100 single shot spectra. This value was sufficiently high as starting from about 40 accumulated spectra, the average spectrum did not change remarkably. Figure 2 compares two single-shot spectra with the spectrum averaged over 100 laser shots.

To reduce the role of fluctuations, in many works the intensities of lines of the single-shot spectrum are normalised dividing the intensity  $I_\lambda$  by the total intensity  $I_T$  [20–23]. In our case, the normalisation reduced fluctuations by a factor of about 1.3. In the present paper, due to its comparatively low effect, no normalization of every single shot spectrum was applied.

Hereinafter, the term “spectrum” always means the sum of 100 single shot spectra, and, consequently, the intensity,  $I_\lambda$ , is the sum of 100 single shot intensities. The acquisition of 100 single-shot spectra took three minutes. At a fixed value of the moisture content of a sample, the series of five spectra was recorded. This procedure lasted 15 minutes. For each sample the LIBS recordings were collected at five different values of moisture content. Thus, each sample was characterised by 25 spectra and the total number of spectra was 375.

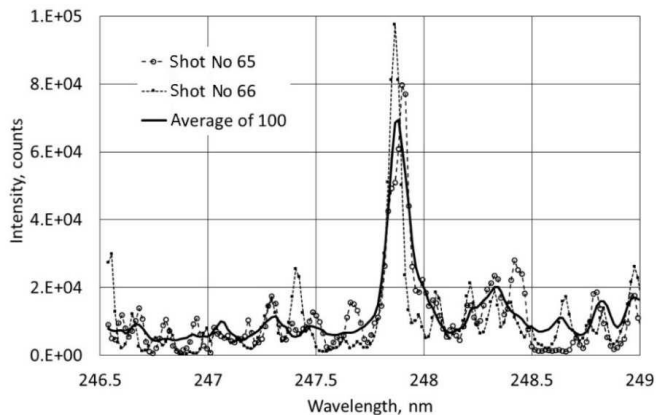


Fig. 2. Spectra near the carbon line at  $\lambda = 247.86$  nm, air-dry sample No 14.

#### 4. Correlation between spectral line intensity and moisture of samples

Figure 3 reflects the moisture effect on  $I_T$ . In this figure, samples are numbered in ascending order of the calorific value, whereby the series of each sample are in ascending order of the moisture content. At fixed values of the calorific value  $Q^d$  and moisture content  $W_w$ , points of  $I_T$  are in timeline with the spectra recording.

Figure 3 shows that  $I_T$  of a sample decreases with increasing moisture content, which is in accordance with the results obtained by other investigators [4, 24–26]. This trend is more apparent for samples with low calorific values (samples 1–5). Another trend, also more pronounced in case of samples with low calorific values, is the increase of  $I_T$  with the spectrum number in a series. In case of some samples with high calorific value, no similar trend can be observed.

The intensities of individual spectral lines also diminished with increasing moisture content, as did the total intensity. As shown in sections 6 and 7, the normalization by  $I_T$  improved the precision of evaluation of both the calorific value and the moisture content. In the further description of the results, we will use normalized intensities of spectral lines,  $I_\lambda/I_T$ .

The authors calculated the coefficients of correlation  $R$  between the moisture content and normalized intensities of spectral lines. Although  $R$  values of a spectral line of different samples differed, the main regularities were independent of the sample number. Correlation coefficients shown in Figure 4 were obtained on the basis of all 375 spectra of samples.

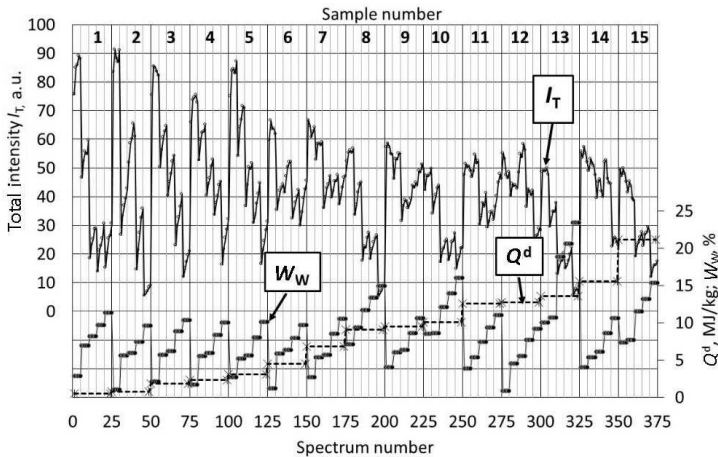


Fig. 3. Total intensity  $I_T$ , calorific value  $Q^d$  and moisture content  $W_w$  as a function of spectrum number. For clarity,  $I_T$  data are shifted up.

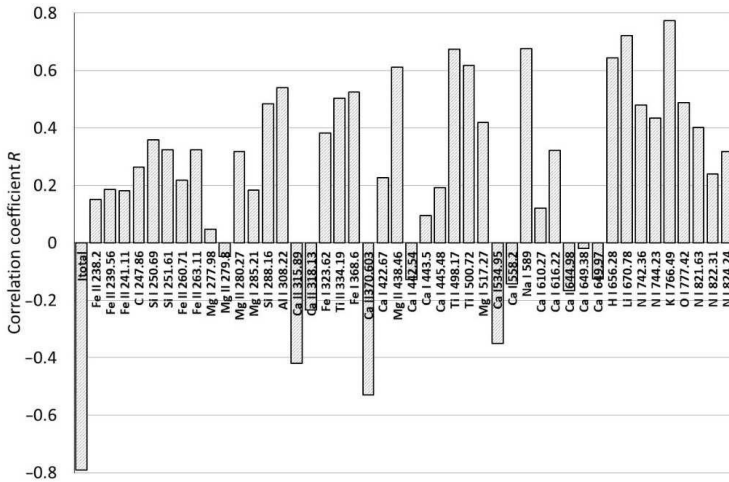


Fig. 4. Correlation between the moisture content of samples,  $W_w$ , and normalized spectral line intensity. The first bar in the row presents the correlation with the total intensity,  $I_T$ .

For all elements the value of the square of the correlation coefficient was low,  $R^2 \leq 0.6$ . A surprisingly low value,  $R^2 = 0.4$ , was obtained for the hydrogen line, although hydrogen should have a strong relationship with moisture content [16]. Alkaline metals and Ti had a comparatively high positive correlation. For a number of Ca lines as well as for the total intensity, the correlation coefficient  $R$  was negative.

Figure 5 illustrates the dependence of the normalized intensity of the hydrogen line,  $I_H$ , on the spectrum number. This figure is organised in a similar way as Figure 3. At fixed values of  $Q^d$  and  $W$ , points of  $I_H$  are in timeline with the spectra recording.

According to Figure 5, samples with low calorific values (samples 1–5) are characterised by two well-pronounced trends. First, for a sample the intensity  $I_H$  increases remarkably with the moisture content. Secondly, at a fixed moisture content of a sample,  $I_H$  decreases during the recording of a 5-spectra series, with the exception of the lowest  $W_w$  value. Samples of high calorific values exhibit similar yet less pronounced trends.

These trends become understandable considering that LIBS gives information about a thin surface layer of lumps. Because of the drying by airflow, the amount of moisture on the surface layer of oil shale lumps is likely not the same as that inside the lumps. This difference is greater in case of barren limestone samples with minor kerogen content, i.e. samples 1–5, while kerogen-rich samples transport water from the inside to the surface more rapidly, which makes the difference between the surface and bulk moisture values smaller.

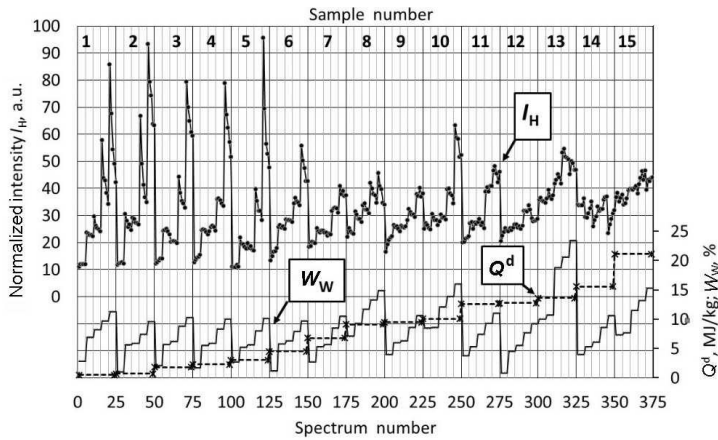


Fig. 5. Normalized intensity of the hydrogen line  $I_H$ , calorific value  $Q^d$  and moisture content  $W_W$  as a function of spectrum number. For clarity,  $I_H$  data are shifted up.

In samples of high calorific values,  $I_H$  changes caused by moisture content variation are less pronounced compared with low-calorific-value samples. It is explainable by the fact that hydrogen is also contained in the kerogen – the organic component of oil shale. Paris et al. [16] showed that the intensity  $I_H$  can be represented as a linear combination of the percentage of hydrogen atoms in organics and that in water. In high-grade oil shale, hydrogen in the organic part likely makes a more significant contribution to  $I_H$  and thus this parameter is less influenced by moisture content.

## 5. Correlation between spectral line intensities and calorific value

Figure 6 shows the coefficients of correlation between the calorific value  $Q^d$  and normalized spectral line intensities determined on the basis of all 375 spectra.

As  $\text{CaCO}_3$  is the main mineral component of oil shale [2], the correlation between  $Q^d$  and the number of spectral lines of Ca is negative, whereas spectral lines of all other elements have a positive correlation. The normalised intensity of the carbon line  $I_C$ ,  $\lambda = 247.86$  nm, exhibited the highest correlation with the calorific value. Assuming a linear dependence between  $I_C$  and  $Q^d$ , we found that the correlation  $R^2 = 0.823$  and the standard deviation  $SD = 4.42$  MJ/kg characterise this dependence. For all other spectral lines,  $R^2 < 0.5$ .

In Figure 7, the dependence of the normalized intensity, calorific value and moisture content on spectrum number is demonstrated.

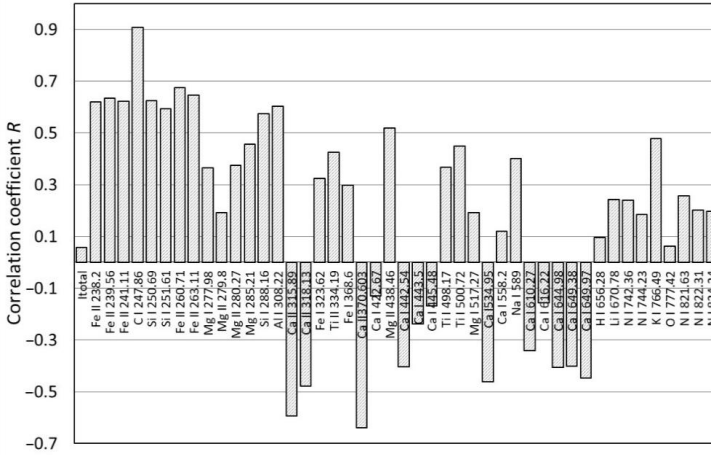


Fig. 6. Correlation between the normalised intensity of a spectral line and calorific value  $Q^d$ . The first bar in the row presents the correlation with the total intensity.

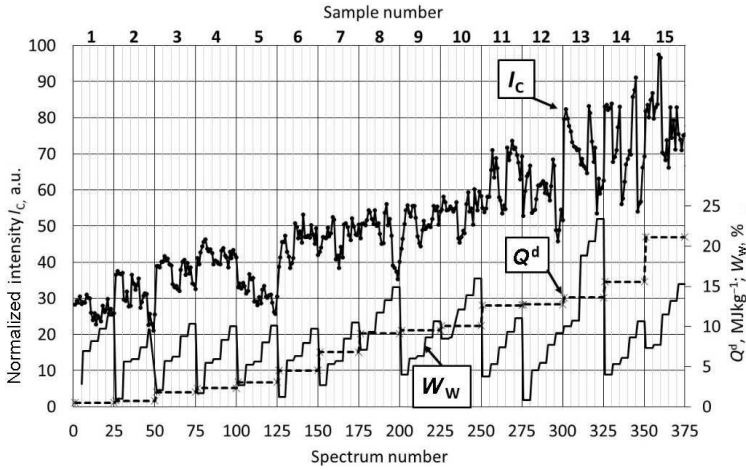


Fig. 7. Dependence of normalized intensity  $I_C$ , calorific value  $Q^d$  and moisture content  $W_w$  on spectrum number.

Like in Figures 3 and 5, the spectra in Figures 7 are shown in ascending order of the calorific value and moisture content of the samples. In case of samples 1–10,  $I_C$  seems to be independent of the moisture content, while in case of high-calorific-value samples,  $I_C$  fluctuates remarkably.

## 6. Multivariate linear regression model for calorific value

The standard deviation, 4.42 MJ/kg, obtained for calorific value by the carbon line only, is unacceptably high for many applications. Considering this, we further applied for the prediction of calorific value and moisture content the model of multivariate linear regression [27].

Like Aints et al. [15], we assumed that the calorific value of a sample could be expressed as a linear combination of measured spectral line intensities:

$$Q = \mathbf{X} \cdot \mathbf{I}, \quad (1)$$

where  $Q$  denotes the calorific value of a sample, vector  $\mathbf{I}$  elements  $I_n$  are intensities of spectral lines, and vector  $\mathbf{X}$  elements  $X_n$  are coefficients whose values must be found during the calibration [15]. The index  $n$  has values  $0 \dots N$  where  $N$  is the number of spectral lines chosen for calibration.

Coefficients  $\mathbf{X}$  were calculated according to the ordinary least square regression as follows:

$$\mathbf{X} = (\mathbf{A}^T \cdot \mathbf{A})^{-1} \cdot \mathbf{A}^T \cdot \mathbf{B}, \quad (2)$$

where  $\mathbf{A}$  is an  $M \times N$  matrix whose elements  $I_{m,n}$  are normalised intensities of spectral lines used in the course of calibration,  $M$  is the number of spectra used for calibration,  $\mathbf{B}$  is an  $M$  element vector whose elements are known values of calorific values of samples used for calibration, the superscript  $T$  denotes the transposed matrix.

The predictive power of the model was evaluated using the leave one out cross-validation method [28]. We used spectra of 14 samples, each with five different moisture contents (altogether 350 spectra) for calibration, i.e. for calculation of coefficients  $\mathbf{X}$  according to Equation (2). Using these coefficients and the set of 25 spectra of the test sample, the calorific value was calculated according to Equation (1). This procedure was repeated, leaving out from calibration, one by one, each of 15 samples.

The standard deviation error of prediction (SDEP) was used to evaluate the predictive power of the model:

$$\text{SDEP} = \sqrt{\frac{1}{K} \sum_{i=1}^K (Q_i^p - Q_i^d)^2}, \quad (3)$$

where  $Q_i^d$  denotes the calorific value of a test sample measured with a bomb calorimeter and  $Q_i^p$  was calculated using Equation (1),  $K$  is the total number of measurements ( $K = 375$ ).

Altogether 20 preselected lines, which had an acceptable signal-to-background ratio and were not interfered with by other lines, were used for determination of the optimal number of spectral lines (variables) for the linear regression model. The optimal number of spectral lines was found by including them in the model, one at a time [28]. The first variable introduced in the regression was the intensity of the carbon line,  $I_C$ , which had the best

correlation with the calorific value. The first selected variable was included in all further calculations. New variables were progressively included in the regression model, selecting those that gave a minimal value of SDEP. SDEP as a function of the number of selected spectral lines  $N$  is presented in Figure 8, with a minimum value of 1.76 MJ/kg at  $N = 10$ .

Fig. 9a shows the correlation between the calorific values determined by the bomb calorimetric method and the LIBS-based multivariate regression, which used the set of 10 first spectral lines in Figure 8. The value of the correlation coefficient,  $R^2 = 0.91$ , was higher than the  $R^2 = 0.823$  obtained for the correlation between  $I_C$  and  $Q^d$ . The standard deviation, 1.76 MJ/kg, for  $Q^p - Q^d$  where  $Q^p$  was determined as a linear combination of intensities

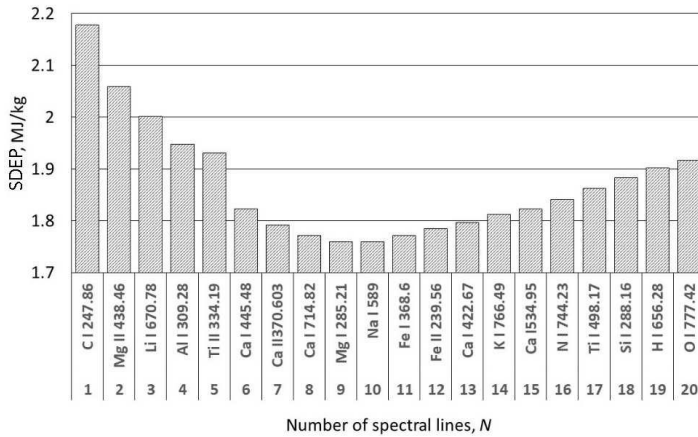


Fig. 8. Standard deviation error in prediction (SDEP) as a function of the number of selected lines. SDEP is minimum at  $N = 10$ .

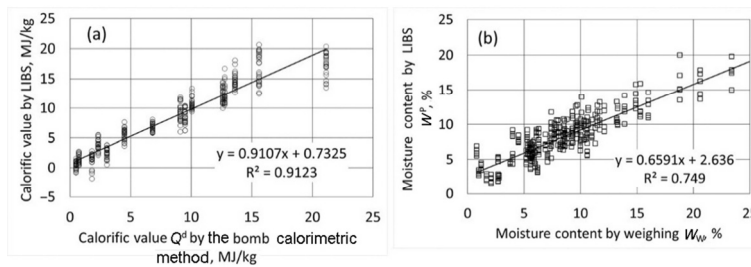


Fig. 9. (a) Calorific value determined by LIBS,  $Q^p$ , vs dry-base calorific value  $Q^d$ ; (b) moisture content determined by LIBS,  $W^p$ , vs moisture content determined by weighing,  $W_w$ . The lines are linear fits of data points.

of 10 spectral lines, was also much higher than that for the single carbon line. When using only air-dry samples for the prediction of the calorific value, the correlation  $R^2 = 0.96$  and the standard deviation was 1.1 MJ/kg. Our calculations also demonstrated that the normalization of spectral line intensities influenced the results. In case of non-normalised intensities,  $SD(Q^p - Q^d) = 2.92$  MJ/kg.

The finding that only 10 lines were needed for determination of calorific value would allow in further studies a considerable simplification of the detection set-up.

## 7. Multivariate regression model for moisture content

A similar procedure as used for determination of calorific value by LIBS was also applied for determination of the moisture content of samples. During the procedure, the following was changed. For validation by leave one out method, the spectra were sorted in ascending order by moisture content and not by calorific value. Then all spectra were divided into five groups with different moisture contents, while four groups of these five were used for calibration and one for validation. This procedure was performed for each group. Figure 10 depicts SDEP as a function of the number of selected spectral lines  $N$  used for determination of moisture content. The number of lines  $N$  corresponding to the minimum SDEP is 8.

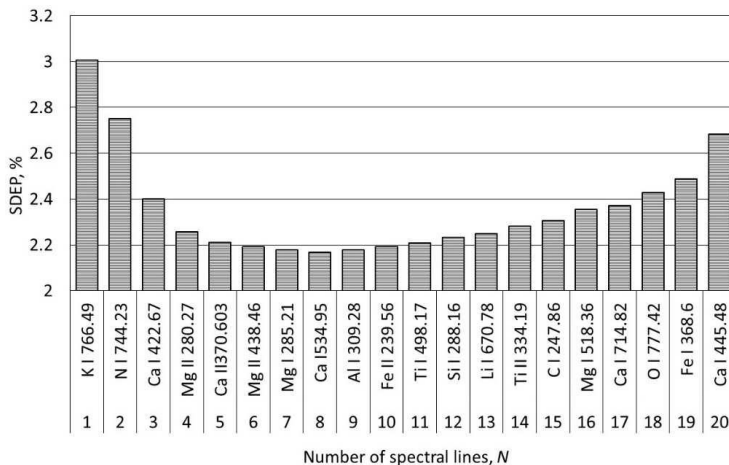


Fig. 10. SDEP as a function of the number of selected lines for determination of moisture content.

Figure 9b shows the relationship between the moisture content determined by LIBS,  $W^p$ , and that found by weighing,  $W_w$ . The corresponding coefficient of correlation ( $R^2$ ) between  $W^p$  and  $W_w$  was 0.75. The minimum SDEP for moisture content was 1.94 % (Fig. 10) and the standard deviation  $SD(W_w - W^p)$  was 1.94%. As in case of calorific value determination, using non-normalized intensities gave a higher  $SD(W_w - W^p)$ , 2.73%.

Better results were obtained when only the very first spectrum from each series was employed in calculations, excluding the four remaining spectra which likely corresponded to the lumps surface with varied moisture. For this last case, the obtained  $SD(W_w - W^p)$  and  $R^2$  were 1.60% and 0.86, respectively.

In Figure 11, the moisture content estimated by LIBS,  $W^p$ , is compared with that determined by weighing,  $W_w$ . Typical for all samples is that the largest deviation of LIBS-determined moisture content values,  $W^p$ , from those obtained by weighing,  $W_w$ , was observed at the lowest moisture content. At the same time, at the lowest moisture content, the  $W^p$  value did not change during the testing of a 5-spectra series. At higher moisture content values,  $W^p$  was time-dependent. In a series of a sample,  $W^p$  decreased with increasing spectrum number in the series which can be explained by the drying of the lumps surface.

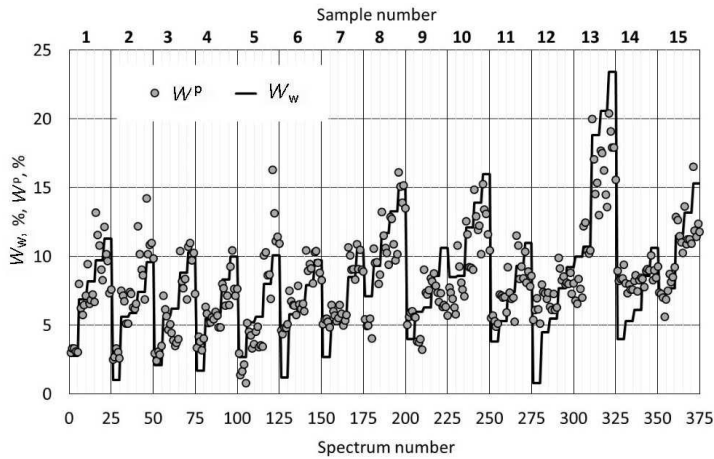


Fig. 11. Moisture content determined by LIBS,  $W^p$ , and by weighing,  $W_w$ , as a function of spectrum number.

## 8. Conclusions

Differently from all previous tests on oil shale by using laser-induced breakdown spectroscopy, the present study applied no preliminary samples preparation, lumps of the tested material were of different size and their facets had a random orientation against the laser beam. Measurements were carried out using the mock-up of the conveyer belt. Overall 75 objects with different calorific values and/or moisture contents were tested. The average of 100 spectra recorded from different spots of an object was used as a unit in data analysis and each object was characterised by the series of five such units.

LIBS results were compared with the calorific value found by the bomb calorimetric method and the moisture content found by the oven-drying method.

Applying the ordinary multivariate regression analysis, the calorific value and moisture content were determined on the basis of LIBS spectra. The optimal set of spectral lines needed for characterisation of oil shale quality was determined.

The root mean square error of the predicted calorific value of crude material was 1.76 MJ/kg ( $R^2 = 0.91$ ). The root mean square error of the predicted moisture content was 1.94 % ( $R^2 = 0.75$ ).

The main factor influencing the accuracy of the LIBS determination of the moisture content was the drying of the lumps surface by airflow. During a measurement series the drying led to the difference between the surface and bulk moisture amounts of lumps.

The drying effect caused by airflow will be less pronounced in case of a real running conveyer belt. Another way of decreasing the influence of difference between the surface and bulk properties of oil shale lumps is the application of a double pulse laser whose first pulse removes the thin top layer of a lump and during the second one a spectrum is recorded. Together with the improvement of the accuracy of moisture content determination, also the root mean square error of the predicted calorific value will be decreased.

The present study demonstrated that the same data recorded by laser-induced breakdown spectroscopy can be used for obtaining express information about calorific value and moisture content in conditions close to those at the conveyer belt in industry.

## Acknowledgements

This work was financially supported by the Environmental Investment Centre of Estonia (project No 7594).

## REFERENCES

1. Aarna, I. Developments in production of synthetic fuels out of Estonian oil shale. *Energy Environ.*, 2011, **22**(5), 541–552.
2. Ots, A. Estonian oil shale properties and utilization in power plants. *Energetika*, 2007, **53**(4), 8–18.
3. Valgma, I., Reinsalu, E., Sabanov, S., Karu, V. Quality control of oil shale production in Estonian mines. *Oil Shale*, 2010, **27**(3), 239–249.
4. Gaft, M., Dvir, E., Modiano, H., Schone, U. Laser induced breakdown spectroscopy machine for online ash analyses in coal. *Spectrochim. Acta B*, 2008, **63**(10), 1177–1182.
5. Hahn, D. W., Omenetto, N. Laser-induced breakdown spectroscopy (LIBS), part II: review of instrumental and methodological approaches to material analysis and applications to different fields. *Appl. Spectrosc.*, 2012, **66**(4), 347–419.
6. Romero, E. C., De Saro, R. LIBS analysis for coal. In: *Laser-Induced Breakdown Spectroscopy: Theory and Applications* (Musazzi, S., Perini, U., eds). Springer, Berlin-Heidelberg, 2014, 511–529.
7. Redoglio, D., Golinelli, E., Musazzi, S., Perini, U., Barberis, F. A large depth of field LIBS measuring system for elemental analysis of moving samples of raw coal. *Spectrochim. Acta Part B At. Spectrosc.*, 2016, **116**, 46–50.
8. Craparo, J., De Saro, R., Romero, C., Yao, Z., Whitehouse, A., Weisberg, A. Measuring thermal properties of coal with a commercial bench top LIBS system. In: *Applied. Industrial Optics: Spectroscopy, Imaging and Metrology. AIO*, 2012, 4–6.
9. Yao, S., Lu, J., Dong, M., Chen, K., Li, J., Li, J. Extracting coal ash content from laser-induced breakdown spectroscopy (LIBS) spectra by multivariate analysis. *Appl. Spectrosc.*, 2011, **65**(10), 1197–1201.
10. Yuan, T., Wang, Z., Lui, S.-L., Fu, Y., Li, Z., Liu, J., Ni, W. Coal property analysis using laser-induced breakdown spectroscopy. *J. Anal. At. Spectrom.*, 2013, **28**(7), 1045–1053.
11. Chen, M., Yuan, T., Hou, Z., Wang, Z., Wang, Y. Effects of moisture content on coal analysis using laser-induced breakdown spectroscopy. *Spectrochim. Acta B*, 2015, **112**, 23–33.
12. Birdwell, J. E., Washburn, K. E. Rapid analysis of kerogen hydrogen-to-carbon ratios in shale and mudrocks by laser-induced breakdown spectroscopy. *Energ. Fuel.*, 2015, **29**(11), 6999–7004.
13. Washburn, K. E. Rapid geochemical and mineralogical characterization of shale by laser-induced breakdown spectroscopy. *Org. Geochem.*, 2015, **83–84**, 114–117.
14. Sanghavi, H. K., Jain, J., Bol'shakov, A., Lopano, C., McIntyre, D., Russo, R. Determination of elemental composition of shale rocks by laser induced breakdown spectroscopy. *Spectrochim. Acta B*, 2016, **122**, 9–14.
15. Aints, M., Paris, P., Laan, M., Piip, K., Riisalu, H., Tufail, I. Determination of heating value of Estonian oil shale by laser-induced breakdown spectroscopy. *J. Spectrosc.*, 2018, Article ID 4605925, 1–10.
16. Paris, P., Piip, K., Lepp, A., Lissovski, A., Aints, M., Laan, M. Discrimination of moist oil shale and limestone using laser induced breakdown spectroscopy. *Spectrochim. Acta B*, 2015, **107**, 61–66.
17. Väli, E., Valgma, I., Reinsalu, E. Usage of Estonian oil shale. *Oil Shale*, 2008, **25**(2S), 101–114.
18. O'Kelly, B. C. Oven-drying characteristics of soils of different origins. *Dry. Technol.*, 2005, **23**(5), 1141–1149.
19. Wisbrun, R., Schechter, I., Niessner, R., Schroder, H., Kompa, K. L. Detector for trace elemental analysis of solid environmental samples by laser plasma spectroscopy. *Anal. Chem.*, 1994, **66**(18), 2964–2975.
20. Bolger, J. A. Semi-quantitative laser-induced breakdown spectroscopy for analysis of mineral drill core. *Appl. Spectrosc.*, 2000, **54**(2), 181–189.

21. Feng, J., Wang, Z., Li, Z., Ni, W. Study to reduce laser-induced breakdown spectroscopy measurement uncertainty using plasma characteristic parameters. *Spectrochim. Acta B*, 2010, **65**(7), 549–556.
22. Senesi, G. S. Laser-induced breakdown spectroscopy (LIBS) applied to terrestrial and extraterrestrial analogue geomaterials with emphasis to minerals and rocks. *Earth-Sci. Rev.*, 2014, **139**, 231–267.
23. Tucker, J. M., Dyar, M. D., Schaefer, M. W., Clegg, S. M., Wiens, R. C. Optimization of laser-induced breakdown spectroscopy for rapid geochemical analysis. *Chem. Geol.*, 2010, **277**(1–2), 137–148.
24. Bublitz, J., Dölle, C., Schade, W., Hartmann, A., Horn, R. Laser-induced breakdown spectroscopy for soil diagnostics. *Eur. J. Soil Sci.*, 2001, **52**(2), 305–312.
25. Chen, M., Yuan, T. Hou, Z., Wang, Z., Wang, Y. Effects of moisture content on coal analysis using laser-induced breakdown spectroscopy. *Spectrochim. Acta B*, 2015, **112**, 23–33.
26. Kim, G., Kwak, J., Kim, K.-R., Lee, H., Kim, K.-W., Yang, H., Park, K. Rapid detection of soils contaminated with heavy metals and oils by laser induced breakdown spectroscopy (LIBS). *J. Hazard. Mater.*, 2013, **263**, 754–760.
27. Martens, H., Naes, T. *Multivariate Calibration*. John Wiley Sons, Chichester, 1989.
28. Shahlaei, M. Descriptor selection methods in quantitative structure–activity relationship studies: A review study. *Chem. Rev.*, 2013, **113**(10), 8093–8103.

*Presented by V. Oja, A. Konist, and A. Siirde*

Received May 3, 2018



## Appendix 3

### Paper - P III

Tufail, I., Paris, P., Jõgi, I., Aints, M., Siiman, A., Riisalu, H., & Laan, M. (2020). Application of diffuse reflectance spectroscopy for quick laboratory assessment of Estonian oil shale quality. *Proceedings of the Estonian Academy of Sciences*, 69(2).





## Application of diffuse reflectance spectroscopy for quick laboratory assessment of Estonian oil shale quality

Iram Tufail<sup>a,b</sup>, Peeter Paris<sup>a</sup>, Indrek Jõgi<sup>a</sup>, Märt Aints<sup>a</sup>, Andres Siiman<sup>c</sup>, Hella Riisalu<sup>d</sup>, and Matti Laan<sup>a\*</sup>

<sup>a</sup> Institute of Physics, University of Tartu, Ostwaldi 1, 50411 Tartu, Estonia

<sup>b</sup> Department of Cybernetics, Tallinn University of Technology, Akadeemia tee 21, 12618 Tallinn, Estonia

<sup>c</sup> Syntpot OÜ, Tähe 106A, 50107 Tartu, Estonia

<sup>d</sup> Virumaa College, Tallinn University of Technology, Järveküla tee 75, 30322 Kohtla-Järve, Estonia

Received 30 May 2019, accepted 27 February 2020, available online

© 2020 Authors. This is an Open Access article distributed under the terms and conditions of the Creative Commons Attribution-NonCommercial 4.0 International License (<http://creativecommons.org/licenses/by-nc/4.0/>).

**Abstract.** Diffuse reflectance spectroscopy in near infrared region was used as a fast laboratory method for quantitative assessment of the calorific value and the moisture content of Estonian oil shale. Samples of different calorificity were collected from Narva open-cast mine and from beneficiation plant of Estonia underground mine, Estonia. The set of crushed oil shale samples, which moisture content was varied were tested by the help of a commercial multipurpose analyser, where Fourier-transform spectrometer recorded spectra in near infrared region and the software used partial least squares regression method. Results were related to the values of calorificity and moisture content, obtained by the bomb calorimeter and weighing methods, respectively. Bands characterizing organic and inorganic parts of the samples as well as the presence of the free water were ascertained by the infrared spectroscopy. Using the software provided by the analyser, the calorific value and the moisture content of samples were predicted. The prediction error of the lower calorificity was 1 MJkg<sup>-1</sup> and prediction error of the weight percent of the moisture content was 1.35%. The comparison between achieved results and the values obtained from earlier laser-induced breakdown spectroscopy (LIBS) measurements shows that in laboratory conditions more precise prediction can be made by diffuse reflectance measurements. Further improvement of the prediction accuracy could be achieved by modified software which considers observed nonlinear effects in spectra.

**Key words:** crushed oil shale, diffuse reflectance spectroscopy in near infrared region, assessment of calorific value and moisture content.

### 1. INTRODUCTION

In Estonian energy production, renewable sources have an increasing importance but at least during the following decade, oil shale will be the dominating raw material for combustion at power plants and for production of shale oil [1]. The optimization of the working regimes of both processes need online control of the oil shale quality which varies from place to place, depending on the oil shale deposit.

The quality of oil shale is often characterized by its calorific value. Currently, a precise determination of the oil shale calorific value is made in laboratory conditions by the bomb calorimetric method [2]. This procedure has typically several time-consuming steps (sampling, transportation, averaging the initial sample to analytical sample, grinding, measuring moisture content and finally, determining the calorific value in bomb). The total duration determining the calorific value could take several hours. Accordingly, this routine method is not suitable for fast quality control of non-stop processes.

\* Corresponding author, [matti.laan@ut](mailto:matti.laan@ut)

Among methods applied for quality control of raw material on running conveyer belt, the optical method based on the laser-induced breakdown spectroscopy (LIBS) has the advantage of being rapid, non-destructive and relatively safe [3–5]. In case of this method, a focused laser beam evaporates the material and emission spectra of chemical elements is recorded [6]. For oil shale analysis, our previous study demonstrated that the concentrations of main ingredients of pellets pressed from oil shale powders can be found on the basis of LIBS spectra by using methods of multivariate analysis [7]. LIBS was further applied for the determination of the calorific value and the moisture content of crushed oil shale samples on the mock-up of the conveyer belt [8]. Results of the two last studies showed that LIBS method could be implemented for obtaining online information of the oil shale quality.

Another optical method used for the assessment of the quality of the raw material is the diffuse reflectance spectroscopy (DRS), which records spectra in infrared or near infrared (NIR) regions [9,10]. As spectra arising in these regions are caused by vibrations of chemical compounds, they are more directly related to the properties of material (e.g. calorific value and moisture) than that of atomic spectra of LIBS. The method is widely used in food and beverage industry, agricultural tests and petrochemical industry [11,12], and it has potential for online measurements over moving conveyer belt [13,14]. The method of NIR DR spectroscopy was successfully used in studies of various quality parameters of coal and biomass/coal samples, applying different data processing methods [15–18]. For oil shale powder samples, it was possible to

predict the yield of shale oil by the NIR DR spectroscopy [19–21]. Nevertheless, there are no studies where NIR DR spectroscopy had been used to predict the calorific value and moisture content of the oil shale.

The aim of the present study was to evaluate the suitability of NIR DR spectroscopy for determining the calorific values and moisture content of crushed oil shale. An extra task of the study was the comparison of results of DR spectrometry with those obtained by LIBS, and thus, the present study uses the same set of samples of crushed oil shale which were used for LIBS studies [8]. NIR spectra were recorded at different values of moisture content. For quantitative analysis, multivariate calibration models were applied.

## 2. SAMPLES

The samples investigated during present study were similar as in our previous study with LIBS and are listed in Table 1 [8]. Most of the samples (11) were collected from Narva (Estonia) open-cast mine, from the 7th trench's west side exposure (outcrop), from different layers of oil shale and limestone interlayers A-F2 [22]. Additional 4 samples labelled with EST were taken from the stopped conveyer belt of the beneficiation plant of Estonia underground mine.

All samples were crushed by jaw crusher to the fraction of 0–25 mm. One part of each sample was used for the determination of calorific value by the bomb calorimeter method (ISO 1928). Calorific values  $Q^d$  of dry samples are presented in Table 1.

**Table 1.** Calorific value and moisture content of samples

No.	Index of layer	$Q^d$ (MJ/kg)	Moisture content $W$ (w%)						
			W1	W2	W3	W4	W5	W6	W7
1	B	21.123	0.5	3.7	7.6	11.3	14.9	18.6	21.6
2	C	15.581	0.5	3.6	7.2	10.8	14.5	18.1	21.7
3	A+A'	13.605	0.5	3.7	7.4	10.8	14.4	18	22.3
4	ESTQ11.4	12.758	0.5	3.7	7.5	11.2	14.9		
5	E	12.616	0.5	3.6	7.2	10.7	14.4		
6	ESTQ8.0	10.064	0.5	3.6	7.3	11	14.7	18.3	
7	F1	9.493	0.5	3.7	7.4	11.1	14.7		
8	ESTQ7.0	9.1	0.5	3.7	7.3	11	14.6	18.3	
9	D	6.813	0.5	3.6	7.3	10.8	14.3		
10	F2	4.502	0.5	3.7	7.5	11.2	14.9		
11	ESTQ1.5	3.055	0.5	3.7	7.4	11.1	14.6		
12	B/C	2.32	0.5	3.9	7.6	11.4	15	17.9	
13	D/E	1.811	0.5	3.8	7.6	11.3	14.9		
14	C/D	0.721	0.5	3.7	7.4	11	14.4		
15	B/A'	0.503	0.5	3.8	7.5	11.3	15		

Another part of samples was kept in hermetically closed jars between measurements of spectra. The moisture content of samples was determined by oven-drying method. Differently from the previous study [8], the moisture content of samples was increased from low to high moisture level (up to 20%) by pipetting 4% of the sample weight into the jar, followed by subsequent “homogenization” in closed jars, which lasted about 10 hours at room temperature.

Before the measurements with increasing moisture content, samples were dried in the evacuated oven at the temperature of 105 °C for about 24 hours. These dry samples were characterized by 0.5 weight percent of moisture content.

Overall, seven remarkably different values of moisture content were set (Table 1). For a number of samples, the highest moisture contents (see columns W6 and W7, Table 1) could not be set as they were not able to absorb such amount of water.

### 3. DEVICE AND PROCEDURE OF MEASUREMENTS

The NIR spectra from crushed oil shale samples were measured and the data were processed by multi-purpose analyser MPA-FT-NIR (Bruker Optik GmbH), where IR spectrum in 12500–3600  $\text{cm}^{-1}$  (800–2780 nm) interval was recorded by Fourier transform spectrometer. The device worked in diffuse reflectance mode. Figure 1 passes the idea of collection of light reflected from a sample [23]. Lumps of oil shale with different size and random orientation filled tightly a rotating Petri dish of 90 cm diameter. The centre of the incident light beam of  $\approx 3 \text{ cm}^2$  cross-section area was at 2.5 cm distance from the rotation axis. Light, partly reflected from oil shale lumps at very different angles, is collected by the integrating sphere. The inner surface of the sphere has a

very diffuse coating with high reflection and evenly dispersed light is formed due to the multiple reflections inside the sphere, which is detected by detector. The relative remittance  $R'$  is determined as the ratio of intensity of the signal from the sample of the reference non-absorbing surface.

At 8  $\text{cm}^{-1}$  spectral resolution, the average of 64 spectra was saved. During the recording of these spectra Petri dish made 2.7 revolutions. At a fixed moisture content each sample was characterized by at least three averaged spectra, the time interval between the recordings of spectra was  $\approx 1 \text{ min}$ . Overall, 355 spectra were recorded.

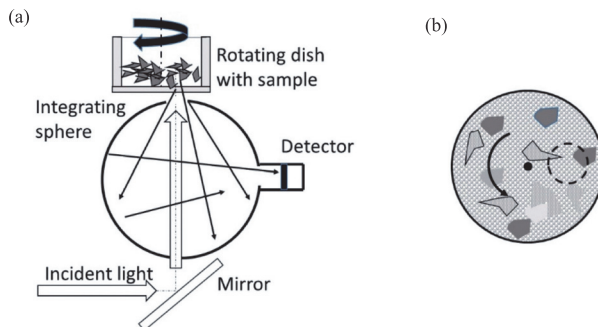
### 4. SPECTRA

Figure 2a presents the dependence of absorbance  $A$  on the wave number  $\nu$ . Here, the term “absorbance” is just the apparent absorbance, introduced as an analogous to that in transmission spectroscopy and defined as  $A = \log(\frac{I_0}{I})$ , its value is directly related to the concentration of absorbing species [10].

Here, like in further figures, the absorbance is presented as a function of wavelength.

At a fixed calorificity the bias component of absorption spectra gradually increased with the growth of the moisture content, whereby in case of samples with higher calorificity the bias was more intensive. At  $\nu > 7500 \text{ cm}^{-1}$  ( $\lambda < 1300 \text{ nm}$ ) the absorption bands were missing and at  $\nu < 3800 \text{ cm}^{-1}$  ( $\lambda > 2600 \text{ nm}$ ) the absorption was very large. For further analysis of spectra, only the narrower spectral range with the characteristic absorbing bands was selected.

Closer examination of presented spectra in the 1200–2600 nm range showed a good signal-to-noise ratio, which allowed to characterize samples by the first derivative of the spectrum. Figure 2b demonstrates that this data



**Fig. 1.** (a) sample illumination and collection of reflected light; (b) top view of Petri dish; dashed line indicates the area of incident light beam.

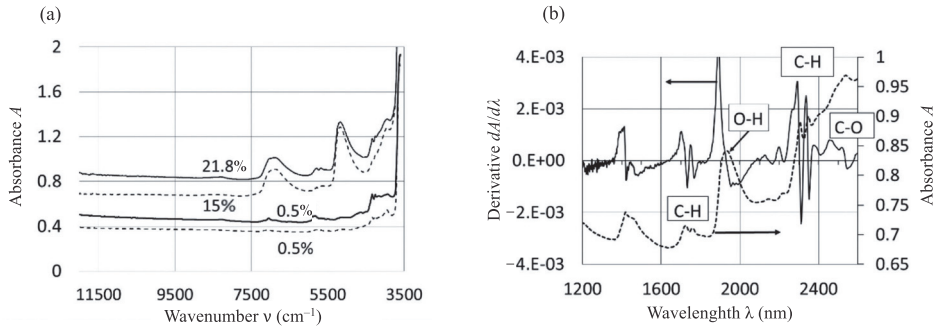


**Fig. 2.** (a) absorbance spectra of samples with drastically different values of calorificity and percentage of moisture content (indicated in figure); sample B ( $Q^d = 21.123 \text{ MJkg}^{-1}$ , solid lines); sample BC ( $Q^d = 2.32 \text{ MJkg}^{-1}$ , dashed lines). (b) absorbance and its derivative as a function of wavelength with the indication of characteristic absorbing bands; sample F1 ( $Q^d = 9.4 \text{ MJkg}^{-1}$ ,  $W_w = 7.5\%$ ).

preprocessing emphasizes steep edges of peaks, thus making the interpretation of spectra easier. Five distinguishable groups of bands exist in the selected spectral range. The most intensive band around 1950 nm ( $5130 \text{ cm}^{-1}$ ) belongs to O-H and is related to the presence of free water [24], while a peak near 2500 nm ( $4000 \text{ cm}^{-1}$ ) characterizes carbonates [25,26]. Both bands near 1700 and 2300 nm belong to C-H vibrations [27]. Near 1400 nm ( $7100 \text{ cm}^{-1}$ ) O-H and C-H bands are overlapped and this part is not used for analysis.

In Fig. 3a spectra of dry samples with very different calorific values can be seen. Differences in spectra correspond to the oil shale chemical composition, whose organic part is described by empirical formula  $C_{421}H_{638}O_{44}S_4NCl$  [28], and the main components of the mineral part are  $CaCO_3$  and  $CaMg(CO_3)_2$  [26]: samples of higher calorificity have more intensive absorption at C-H bands, while samples of lower calorificity have larger absorption of C-O band. Additionally, because of a low moisture content, the absorbance near 1950 nm is practically missing.

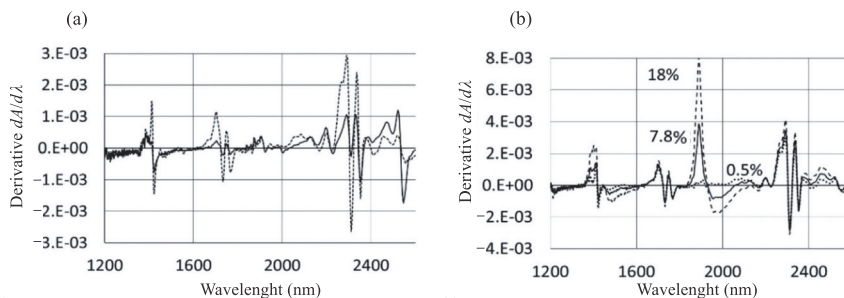
Absorption of O-H band with the peak at 1950 nm has a strong dependence on the moisture content (Fig. 3b). Besides, the moisture content affects the absorbance of bands belonging both to organic (1700 and 2300 nm) and mineral (near 2500 nm) components of the samples.

Figure 4a shows the absorbance of C-H peaks at 2305 nm as a function of calorificity at a fixed moisture content: absorbance is a sublinear function of calorificity, which indicates to the saturation of the absorbance at higher calorific values. Similar non-linear trends were observed in case of all used moisture values.

In case of a certain sample, the absorbance was a linear function of the moisture content (Fig. 4b) but slopes of dependences differ remarkably.

### 5. DATA PROCESSING AND RESULTS

Above presented analysis gives proper physical background of NIR spectra but it does not guarantee the accuracy needed for the assessment of the calorific value



**Fig. 3.** (a) spectra of dry samples,  $W_w = 0.5\%$ ; dashed line – sample A+A' ( $Q^d = 13.6 \text{ MJ/kg}$ ); solid line – sample B/A' ( $Q^d = 0.5 \text{ MJ/kg}$ ). (b) spectra of sample A+A' at three different values of  $W_w = 0.5, 7.8$  and  $18\%$ .

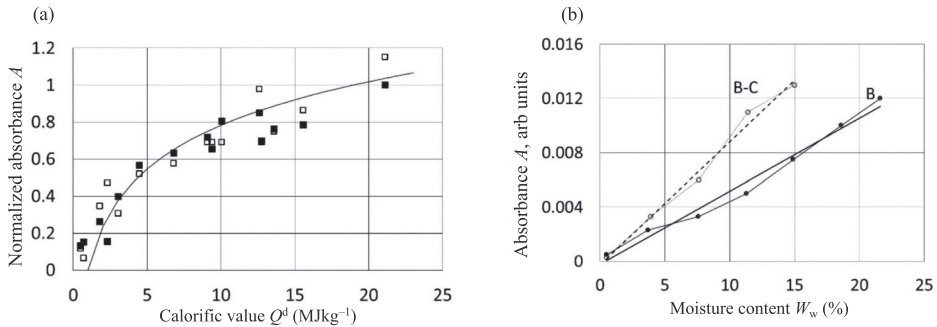


**Fig. 4.** (a) normalized absorbance as a function of calorificity;  $W_w = 14.5\%$ ; filled symbols –  $\lambda = 2305$  nm peak; open symbols –  $\lambda = 1725$  nm peak; solid line – logarithmic fit of  $\lambda = 2305$  nm data. (b) absorbance as a function of moisture content; open symbols – sample B/C ( $Q^d = 2.32$  MJ/kg); filled symbols – sample B ( $Q^d = 21.12$  MJ/kg)  $\lambda = 1925$  nm peak.

and the moisture content as the measured bands are partly overlapped and therefore, the measured absorbance is the sum of the absorbances of all components (not only the component of interest) in the sample.

The software of MPA-FT-NIR device uses multivariate approach, i.e. instead of the intensity of only one specific band, samples are characterized by the entire selected spectrum. Thus, it is assumed that systematic variations in the spectra are related to the sample composition. For data analysis the device software Quant [23] applies partial least square (PLS) regression [29] method, which expects a linear relationship between the spectral data and property value to be determined.

In order to get out most of the information from recordings, a preprocessing of NIR spectra is usually utilized [30]. The device software proposes a number of different preprocessing methods (e.g. first derivative) as well as suggests spectral intervals for building a model for quantification of results. The combination of preprocessing methods and selected spectral ranges are ordered by software

according to the value of root mean square error of prediction (RMSEP) and the one giving the lowest RMSEP was used.

On the basis of spectra belonging to samples with different calorific values and the moisture content, the software of the device calculated the calibration curve which is then used for analyses of unknown samples. For prediction of properties of samples, the software used two validation types. The “cross validation” (leave one out method [31]) uses the same set of samples for calibration and validation but the “test set validation” uses two independent sets of samples, one for calibration and the other for validating the model. In the present study  $\approx 20\%$  of spectra was used for calibration and the remaining  $\approx 80\%$  was the test set.

In case of both types of validations, slopes for calibration and prediction dependences differ only a little (Fig. 5a).

Figures 5a and 6a show correlations between the predicted values of calorificity  $Q^{Pd}$  and moisture  $W^P$  with the calorific value  $Q^d$  and moisture  $W_w$ , respectively.

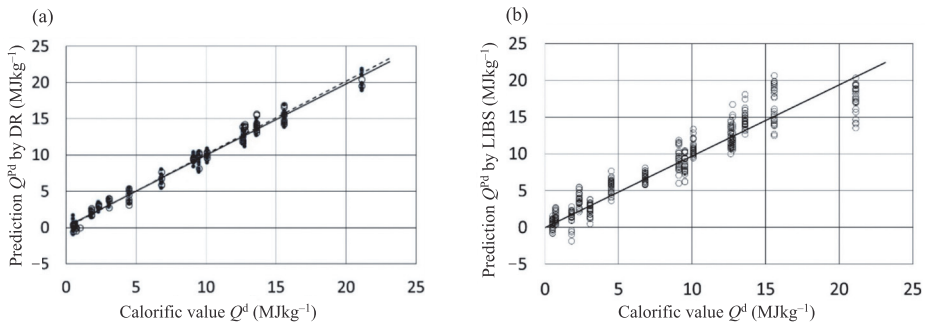


**Fig. 5.** (a) DR results: test set validation of calorific value  $Q^{Pd}$ ; filled symbols – calibration data and dashed line – linear fit for calibration; open symbols – prediction data and solid line – linear fit for prediction. (b) LIBS results: cross validation of calorific value  $Q^{Pd}$ ; data taken from [8].

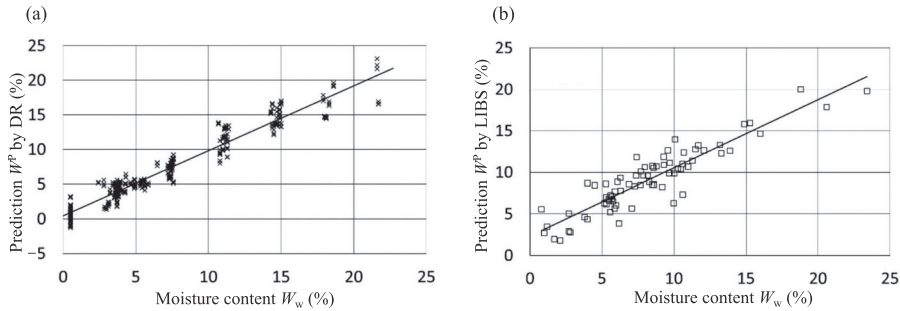


**Fig. 6.** (a) DR results: cross validation of moisture content  $W^p$ . (b) LIBS results: cross validation of moisture content  $W^p$ ; data taken from [8].

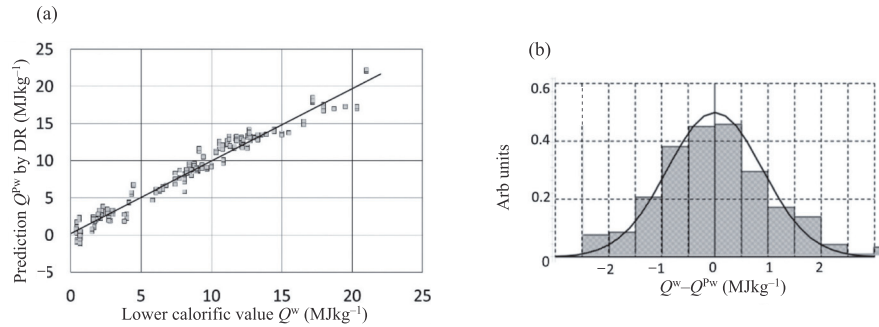


**Fig. 7.** DR results: (a) cross validation of lower calorific value; (b) histogram corresponding to prediction of lower calorific value; solid line – Gaussian fit characterized by standard deviation 1 MJkg<sup>-1</sup>.

Compared with LIBS studies of same crushed oil shale samples [8] we see from Figs 5b and 6b that results of DR are better correlated with the results of calorific bomb and weighing methods.

In industry, the basic parameter of oil shale quality is the lower (net) calorific value  $Q^w$  [32]. The formulae which allow to calculate the calorificity  $Q^w$  on the basis of known values of  $Q^d$  and  $W_w$  are given by ISO 1928:2009 standard [2]. For prediction of lower calorificity  $Q^{pw}$ , the same procedure was followed but instead of  $W_w$ , the prediction values  $W^p$  were used. The relationship between  $Q^w$  and  $Q^{pw}$  is presented in Fig. 7a; and in Fig. 7b is the histogram of the difference  $Q^w - Q^{pw}$ .

### 6. COMPARISON OF DR AND LIBS RESULTS, FURTHER PROSPECTS

Results of prediction of calorificity  $Q^d$ , moisture content  $W_w$ , and lower calorificity  $Q^w$  are shown in Table 2, LIBS results were taken from [7,8]. In the third and fourth

columns are slopes and correlation coefficients of linear fits between “true” and predicted values of corresponding characteristics, while the root mean square errors of prediction (RMSEP) are in the last column.

The best results are obtained for dry powder samples by LIBS. On the other hand, the time needed for preparation of these samples is comparable with that of the traditional calorific bomb method and in this case the only advantage of LIBS is the possibility to predict the concentrations of oil shale ingredients [7].

One experimental problem, common for both DR and LIBS methods, is the accuracy of the estimation of the moisture content. By weighing the samples, it is possible to calculate the moisture content in the body of lumps while DR and LIBS give the moisture at the lumps’ surface. The balance between the moisture at the surface and inside the samples depends on the surrounding environment and the balance could change in time, which leads to the increase of the prediction error. It is the likely reason of higher prediction error in the case of LIBS measurements where the experiments were carried out in an airflow, which

**Table 2.** Results of prediction of oil shale main characteristics

Technique	Samples	Characteristic	Processing	Slope	$R^2$	RMSEP
DR	Crushed oil shale, variable moisture content	$Q^d$	Cross validation	1.00	0.98	0.85 MJ/kg
			Test set validation	1.00	0.97	0.84 MJ/kg
		$W_w$	Cross validation	0.94	0.93	1.35%
			Test set validation	0.97	0.94	1.33%
LIBS	Crushed oil shale, variable moisture content	$Q^w$	Cross validation	0.974	0.96	1 MJ/kg
		$Q^d$	Cross validation	0.91	0.91	1.76 MJ/kg
LIBS	Crushed oil shale, variable moisture content		$W_w$	Cross validation	0.83	0.82
		LIBS	Powder, dry	$Q^d$	Cross validation	1

causes faster changes in the moisture content at the lumps' surface. Furthermore, the moisture affects not only these parts of spectra which are directly related to the moisture content, like O-H band near 1950 nm, but due to the matrix effect, it causes also changes in other parts of spectra (Figure 3b). As a result, the uncertainty of determination of moisture content influences also the accuracy of the determination of the calorificity.

Due to the use of integrating sphere, the role of fluctuations in DR spectra, caused by a random orientation of faces of oil shale lumps, was almost negligible. Contrary, in case of LIBS, even the average intensity of a spectral line found from 100 LIBS spectra needs extra normalization [8]. For this purpose, the average intensity of a line was normalized by the average of the total intensity in 220–850 nm range [8]. This procedure gave a better signal-to-background ratio but it did not allow to exclude “blank” spectra caused by laser beam impacting between lumps of tested samples [3]. This circumstance seems to be the main reason why the prediction error of  $Q^d$  in case of LIBS is two times larger than in case of DR. Carrying out the normalization of intensity of a spectral line belonging to a single spectrum by the corresponding total intensity allows the discrimination of outliers.

The final remark concerns the used software. We saw that some bands in NIR spectra (Fig. 3) are directly related to the changes of samples' calorificity and moisture content. However, these dependencies alone did not allow to determine the calorificity/moisture content with sufficient accuracy. The main advantage of used multivariate approach which handles all parts of spectra equally, is diminishing the role of uncontrollable factors. On the other hand, this approach almost neglects the physical background of observed trends in spectra. Additional limitation related to PLS is that it could not satisfactorily reflect the non-linear relationship between absorbance and the calorificity (Fig. 4a). An appropriate data processing

which combines the physical processes with the multivariate regression could improve the accuracy of data analysis. This approach was successfully realized in LIBS studies [33] where different dominant factors as a function of spectral line intensity were combined with PLS correction, and a significant improvement of final results was achieved.

## 7. CONCLUSIONS

DR spectroscopy was applied for prediction of calorificity and moisture content of crushed 0–25 mm fraction oil shale samples. The study showed that good correlation between calorific value and moisture content determined by traditional methods and those calculated on the bases of NIR DR spectra could be achieved without any additional preparation of samples.

The list of most important findings is given below:

- In the DR spectra, it was possible to separate vibrational bands which characterize organic and inorganic parts of the matter. The most intensive band belongs to O-H which reflects the presence of free water. The moisture has a strong matrix effect and changes of its content cause remarkable changes in other bands of spectra. At a fixed moisture content, the intensity of bands of the organic part of oil shale are non-linear functions of the calorificity.
- For predicting the calorificity and moisture content, the conventional software of the device was used. The accuracy of predictions was governed by a possible difference of the moisture content at lumps' surface from that of inside the lumps.
- Comparison of DR NIR measurements with LIBS results showed that the model of DR NIR predicts the calorificity with higher accuracy. The values of RMSEP are 0.85 MJ/kg and 1.76 MJ/kg, respectively.

- Regularities in spectra indicate that a considerable improvement of final results of both DR and LIBS methods could be achieved by combining the data processing of the multivariate linear regression with the dominant factor model.

Laboratory online control of oil shale quality by NIR-DR spectroscopy is justified in case of selective mining where the oil shale quality changes comparatively slowly.

## ACKNOWLEDGEMENT

The publication costs of this article were covered by the Estonian Academy of Sciences.

## REFERENCES

- Jordan Kearns, J. and Tuohy, E. Trends in Estonian Oil Shale Utilization, 2015, International center for defense and security, Estonia. [https://icds.ee/wp-content/uploads/2015/Jordan\\_Kearns\\_-\\_Trends\\_in\\_Estonian\\_Oil\\_Shale\\_Utilization\\_Oct\\_2015.pdf](https://icds.ee/wp-content/uploads/2015/Jordan_Kearns_-_Trends_in_Estonian_Oil_Shale_Utilization_Oct_2015.pdf)
- Determination of gross calorific value by the bomb calorimetric method and calculation of net calorific value, ISO 1928:2009, modified.
- Gaft, M., Dvir, E., Modiano, H., and Schone, U. Laser Induced Breakdown Spectroscopy machine for online ash analyses in coal. *Spectrochim. Acta, Part B*, 2008, **63**(10), 1177–1182.
- Romero, C. E., De Saro, R., Craparo, J., Weisberg, A., Moreno, R., and Yao, Z. Laser-induced breakdown spectroscopy for coal characterization and assessing slagging propensity. *Energy Fuels*, 2010, **24**(1), 510–517.
- Sheta, S., Afgan, M., Hou, Z., Yao, S.-C., Zhang, L., Li, Z., and Wang, Z. Coal analysis by laser-induced breakdown spectroscopy: a tutorial review. *J. Anal. At. Spectrom.*, 2019, **34**, 1047–1082.
- Cremers, D. A. and Radziemski, L. J. Handbook of Laser-Induced Breakdown Spectroscopy. John Wiley & Sons, Ltd., 2006.
- Aints, M., Paris, P., Laan, M., Piip, K., Riisalu, H., and Tufail, I. Determination of heating value of Estonian oil shale by laser-induced breakdown spectroscopy. *J. Spectrosc.*, 2018, 4605925. <https://doi.org/10.1155/2018/4605925>
- Aints, M., Paris, P., Tufail, I., Jõgi, I., Aosaar, H., Riisalu, H., and Laan, M. Determination of the calorific value and moisture content of crushed oil shale by LIBS. *Oil Shale*, 2018, **35**(4), 339–355.
- Pasquini, C. Near Infrared Spectroscopy: Fundamentals, Practical Aspects and Analytical Applications. *J. Braz. Chem. Soc.*, 2003, **14**(2), 198–219.
- Blitz, J. P. Diffuse reflectance spectroscopy. In *Modern Techniques in Applied Molecular Spectroscopy* (Mirabella, F. M., ed.). John Wiley & Sons, Inc., 1998, 185–219
- Forrester, S. T., Janik, L. J., McLaughlin, M. J., Soriano-Disla, J. M., Stewart, R., and Dearman, B. Total petroleum hydrocarbon concentration prediction in soils using diffuse reflectance infrared spectroscopy. *Soil Sci. Soc. Am. J.*, 2013, **77**(4), 450–460.
- Kokah, D. R., Silas, A. D., and Akeme-Esuotei, O. N. Rapid assessment of petroleum hydrocarbon contamination in soils: spectroscopy approach. *Eng. Appl. Sci.*, 2019, **4**(3), 66–73.
- Goetz, A. F., Curtiss, B., and Shiley, D. A. Rapid gangue mineral concentration measurement over conveyors by NIR reflectance spectroscopy. *Miner. Eng.*, 2009, **22**(5), 490–499.
- Rodionov, A., Welp, G., Damerow, L., Berg, T., Amelung, W., and Pätzold, S. Towards on-the-go field assessment of soil organic carbon using Vis–NIR diffuse reflectance spectroscopy: Developing and testing a novel tractor-driven measuring chamber. *Soil Tillage Res.*, 2015, **145**, 93–102.
- Kaihara, M., Takahashi, S., Akazawa, T., Sato, T., and Takashi, S. Application of near infrared spectroscopy to rapid analysis of coals. *Spectrosc. Lett.*, 2002, **35**(3), 369–376.
- Bona, M. T. and Andres, J. M. Coal analysis by diffuse reflectance near-infrared spectroscopy: Hierarchical cluster and linear discriminant analysis. *Talanta*, 2007, **72**(4), 1423–1431.
- He, C., Yang, Z., Chen, L., Huang, G., Liao, Na., and Han, L. Influencing factors of on-line measurement of straw-coal blends using near infrared spectroscopy. *Trans. Chin. Soc. Agric. Eng.*, 2012, **30**(9), 192–200.
- Wiesner, K., Fuchs, K., Gigler, A. M., and Pastusiak, R. Trends in near infrared spectroscopy and multivariate data analysis from an industrial perspective. *Procedia Eng.*, 2014, **87**, 867–870.
- Romeo, M. J., Adams, M. J., Hind, A. R., Bhargava, S. K., and Grocott, S. C. Near infrared prediction of oil yield from oil shale. *J. Near Infrared Spectrosc.*, 2002, **10**(3), 223–231.
- Adams, M. J., Awaj, F., Bhargava, S. K., Grocott, S. C., and Romeo, M. J. Prediction of oil yield from oil shale minerals using diffuse reflectance infrared Fourier transform spectroscopy. *Fuel*, 2005, **84**(14–15), 1986–1991.
- Zhang, F., Liu, J., Lin, J., and Wang, Z. Detection of oil yield from oil shale based on near-infrared spectroscopy combined with wavelet transform and least squares support vector machines. *Infrared Phys. Technol.*, 2019, **97**, 224–228.
- Ots, A. Estonian oil shale properties and utilization in power plants. *Energetika*, 2007, **53**(4), 8–18.
- User manual Quant, Bruker Optik GmbH, 2011.
- Viscarra Rossel, R. A., Walvoort, D. J. J., McBratney, A. B., Janik, L. J., and Skjemstad, J. O. Visible, near infrared, mid infrared or combined diffuse reflectance spectroscopy for simultaneous assessment of various soil properties. *Geoderma*, 2006, **131**(1–2), 59–75.
- Gaffey, S. J. Spectral reflectance of carbonate minerals in the visible and near infrared (0.35–2.55 microns); calcite, aragonite, and dolomite. *Am. Mineral.*, 1986, **71**(1–2), 151–162.
- Gunasekaran, S., Anbalagan, G., and Pandi, S. Raman and infrared spectra of carbonates of calcite structure. *J. Raman Spectrosc.*, 2006, **37**(9), 892–899.
- Douglas, R. K., Nawar, S., Alamar, M. C., Mouazen, A. M., and Coulon, F. Rapid prediction of total petroleum hydrocarbons concentration in contaminated soil using vis-NIR spectroscopy and regression techniques. *Sci. Total Environ.*, 2018, **616–617**, 147–155.
- Lille, Ü., Heinmaa, I., and Pehk, T. Molecular model of Estonian kukersite kerogen evaluated by <sup>13</sup>C MAS NMR spectra. *Fuel*, 2003, **82**(7), 799–804.

29. Norgaard, L., Saudland, A., Wagner, J., Nielsen, J. P., Munck, L., and Engelsen, S. B. Interval Partial Least-Squares Regression (iPLS): A comparative chemometric study with an example from near-infrared spectroscopy. *Appl. Spectrosc.*, 2000, **54**(3), 413–419.
30. Rinnan, A., van den Berg, F., and Engelsen, S. B. Review of the most common pre-processing techniques for near-infrared spectra. *Trends Anal. Chem.*, 2009, **28**(10), 1201–1222.
31. Filzmoser, P., Liebmann, B., and Varmuza, K. Repeated double cross validation. *J. Chemom.*, 2009, **23**(4), 160–171.
32. Valgma, I., Reinsalu, E., Sabanov, S., and Karu, V. Quality control of oil shale production in Estonian mines. *Oil Shale*, 2010, **27**(3), 239–249.
33. Wang, Z., Feng, J., Li, L., Ni, W., and Li, Z. A multivariate model based on dominant factor for laser-induced breakdown spectroscopy measurements. *J. Anal. At. Spectrom.*, 2011, **26**(11), 2289–2299.

### **Difuusse peegeldusspektroskoopia rakendamine Eesti põlevkivi kvaliteedi kiireks laboratoorseks hindamiseks**

Iram Tufail, Peeter Paris, Indrek Jõgi, Märt Aints, Andres Siiman, Hella Riisalu ja Matti Laan

Infrapuna piirkonna peegeldusspektroskoopiat kasutati põlevkivi kütteväärtuse ja niiskusesisalduse kvantitatiivseks määramiseks. Erineva kütteväärtusega tüükivi proovid võeti Narva karjäärast ja Estonia kaevanduse rikastusvabrikust. Katsetes muudeti proovide niiskusesisaldust. Testimisel kasutati tööstuslikku analüsaatorit, kus Fourier' spektromeeter registreeris spektri lähedases infrapuna piirkonnas. Testimise tulemusena saadud kütteväärtusi ja niiskusesisaldust võrreldi tulemustega, mis saadi kalorimeetrilise pommi ning kaalumise meetodeid vastavalt kasutades. Infrapuna spektris tehti kindlaks karakteristiklikud ribad, mis iseloomustavad nii proovide orgaanilist ja anorgaanilist osa kui ka vaba vee olemasolu. Kütteväärtuse ennustusviga oli  $1 \text{ MJkg}^{-1}$  ja niiskuse kaaluprotsendi oma 1,35%. Varem kasutatud LIBS-i meetodiga võrreldes olid peegeldusspektroskoopia tulemused täpsemad. Tulemuste arutelus leiti, millise kaevandusmeetodi puhul peaks peegeldusspektroskoopia rakendamine olema kõige efektiivsem ja millised andmetöötuse viisid peaksid viima täpsemate tulemusteni.

## Curriculum Vitae

### Personal data

Name: Iram Tufail  
Date of birth: 14.09.1986  
Place of birth: Pakistan  
Citizenship: Pakistan

### Contact data

E-mail: iram.tufail2010@gmail.com  
Phone: +37254618452

### Education

2015–2021 Tallinn University of Technology, Estonia – PhD  
2012–2014 UET, Lahore, Pakistan – MS  
2006–2010 University of Wah, Wah Cantt, Pakistan – BS (Hons)  
2004–2006 Mashal Degree College, Wah Cantt, Pakistan

### Language competence

Urdu Native  
English Fluent

### Professional employment

2013–2015 Wah College, Wah Cantt, Pakistan – Lecturer

## Elulookirjeldus

### Isikuandmed

Nimi:	Iram Tufail
Sünniaeg:	14.09.1986
Sünnikoht:	Pakistan
Kodakondsus:	Pakistani

### Kontaktandmed

E-post:	iram.tufail2010@gmail.com
Telefon:	+37254618452

### Hariduskäik

2015–2021	Tallinna Tehnikaülikool, Estonia – PhD
2012–2014	UET Lahore, Pakistan – MS
2006–2010	University of Wah, Wah Cantt, Pakistan – BS (Hons)
2004–2006	Mashal Degree College, Wah Cantt, Pakistan

### Keelteoskus

Urdu keel	emakeel
Inglise keel	sorav

### Teenistuskäik

2013–2015	Wah College, Wah Cantt, Pakistan – lektor
-----------	---

ISSN 2585-6901 (PDF)  
ISBN 978-9949-83-888-2 (PDF)